ATMOSPHERIC OZONE, MERCURY, AND BIOMASS BURNING IN SOUTH-CENTRAL TEXAS

A Dissertation Presented to
the Faculty of the Department of Earth and Atmospheric Sciences
University of Houston

In Partial Fulfillment
of the Requirements for the Degree
Doctor of Philosophy

By

Lei Liu

August 2016

ATMOSPHERIC OZONE, MERCURY, AND BIOMASS BURNING IN SOUTH-CENTRAL TEXAS

_____

Lei Liu

APPROVED:

_____

Dr. Robert Talbot, Chairman

_____

Dr. Xun Jiang

_____

Dr. Yuxuan Wang

_____

Dr. Shuhab Khan

_____

Dean, College of Natural Sciences and Mathematics

ACKNOWLEDGEMENTS

I would like to express my special appreciation and thanks to my advisor Professor Robert Talbot, you have been a tremendous mentor for me. I would like to thank you for encouraging my research and for allowing me to grow as a research scientist. Your advice on both research as well as on my career have been priceless. My sincerest gratitude also goes to Professor Xun Jiang, Professor Yuxuan Wang, and Professor Shuhab Khan for permitting me to pursue this research and for your brilliant comments and suggestions to my work, thank you.

I would especially like to thank Dr. Barry Lefer, and Dr. Barkley Sive for their suggestions and willingness to help. I thank Dr. Patrick Laine, and Dr. James Flynn for the support with instrumentation. All of you have been there to support me when I required patients and collected data for my Ph.D. dissertation. Without all of their help, this project would never have been successful.

My deepest appreciation goes to my parents, for their trust, support, and encouragement. Without their love, I would never have accomplished this degree. I would also like to thank all of my friends who supported me to strive towards my goal. At the end I would like express appreciation to my beloved husband, Pengfei. He is always my support in the moments when there was no one to answer my queries.

ATMOSPHERIC OZONE, MERCURY, AND BIOMASS BURNING IN SOUTH-CENTRAL TEXAS

An Abstract of A Dissertation
Presented to
the Faculty of the Department of Earth and Atmospheric Sciences
University of Houston

In Partial Fulfillment
of the Requirements for the Degree
Doctor of Philosophy

By

Lei Liu

August 2016

ABSTRACT

This study investigated atmospheric ozone, mercury, and biomass burning characteristics in south-central Texas. I examined the past twenty-three years of ground-level O_3 data and selected meteorological parameters in Houston, and found the frequency of southerly flow has increased by a factor of ~2.5 over the period 1990–2013, likely suppressing O_3 photochemistry and leading to a "cleaner" Houston environment. The sea breeze was enhanced greatly from 1990 to 2013 due to increasing land surface temperatures, increased pressure gradients, and slightly stronger on-shore winds.

Long-term continuous measurements of atmospheric mercury, meteorological parameters, and key trace gases were conducted in Houston, Texas under urban and coastal marine settings. At the urban site, gaseous elemental mercury (GEM) mean value was 185 ppqv and 165 ppqv at the coastal site. The urban site had a greater occurrence of high mercury events than the coastal site. A variable mercury diurnal pattern was found: At the urban site, GEM showed a maximum mixing ratio before sunrise and the minimum mixing ratio in late afternoon. At the coastal site, GEM decreased at night and reached its minimum before sunrise. The relationship between mercury species and meteorological factors was studied. The concurrence of GEM, CO_2, CO, CH_4, and SO_2 maximum values were striking.

A prescribed grassland fire experiment was conducted employing in-situ field sampling combined with comprehensive pre-burn and post-burn sampling. The volatile

organic compounds (VOCs) exhibited a double peak feature in the flaming and smoldering stages. The emission of VOCs was associated primarily with the smoldering combustion stage and correlated better with CO than with CO_2. The emission factors of CO_2, CO, CH_4, NO, CH_3Cl, C_2H_6, C_2H_4, C_3H_8, C_3H_6, C_6H_6, and C_7H_8 accounted for 96% of the total species. Total gaseous mercury was released primarily during the smoldering phase, although the total amount released from the fire was small (0.015 kg). Overall, 53,257 kg CO_2 was emitted into the atmosphere during the fire and it accounted for 95% of all species emissions. The relationship between carbon emissions from the dry fuel (194 tons) and released from CO_2 (14.5 tons) was found to be 7.5% for this event.

TABLE OF CONTENTS

Chapter 1

Introduction[1]

1.1 Introduction

Houston, the fourth largest city in United States, routinely experienced some of the highest ozone (O_3) mixing ratios in the United States over the past several decades (Kleinman et al., 2002). Due to this it has been classified by the U.S. Environmental Protection Agency as a "severe" 8-hr O_3 nonattainment area in 1997 and a "marginal" 8-hr O_3 nonattainment area in 2008. Houston experienced significant variability in both the peak O_3 mixing ratios and the number of high O_3 days (Lefer et al., 2010).

Air pollution in the Houston area is a product of strong emissions coupled with specialized meteorological conditions (McGaughey et al., 2004). Automobiles and industrial sources along the Houston Ship Channel (HSC) area and in outlying areas of the city emit large amounts of highly reactive volatile organic compounds (HRVOCs)

[1]Material in this chapter was published as portions of the following articles:

Liu, L., Talbot R., and Lan X., Influence of Climate Change and Meteorological Factors on Houston's Air Pollution: Ozone a Case Study, Atmos., 6, 623-640, 2015.

Liu L., Talbot R., Torres A., Lefer B., Lan X., and Flynn J., Comparison of Speciated Atmospheric Mercury at a Coastal and Urban Site, pending submission, 2016.

Liu L., Talbot R., Lan X., Sive B., Lefer B., Flynn J., and Judd L., Emission Estimates of Trace Gases and Volatile Organic Compounds from a Prescribed Grassland Fire in Southeastern Texas, pending submission, 2016.

and nitrogen oxides ($NO + NO_2 = NO_x$) (Kim et al., 2011), which provide the ingredients necessary for ground-level O_3 production in the presence of heat and sunlight.

Meteorology also plays a critical role in O_3 formation, which either dilutes pollutant emissions or allows them to accumulate, and it can also affect other key processes, such as chemical reaction rates (Ngan et al., 2007). Previous studies have shown that levels of O_3 precursors are substantially elevated during post-frontal environments or in the presence of anti-cyclonic conditions where weak winds, clear skies, and subsidence dominates (Rappenglueck et al., 2008). In this study, we characterized various meteorological variables including temperature, wind speed, wind direction, and pressure for both high and low O_3 events over the past 23 years (from January, 1990 to December, 2013). We want to have an in-depth understanding of the relationship between the climate/meteorology factors and O_3 mixing ratios in the Houston area. Another critical question to answer is which is the key meteorology factor that influences concentration of ground-level O_3 on a large time scale in the Houston area?

Another trace gas of interest in this study was mercury (Hg). Mercury is a pervasive and toxic environmental pollutant that exists in several chemical and physical forms that are distributed widely on Earth. The atmosphere serves as the major pathway for the release of mercury from reservoirs to the environment. Mercury in the atmosphere is then deposited to terrestrial systems or water bodies where it is converted to methylated mercury, the most toxic form of mercury, and can enter the food chain by bioaccumulation (Pirrone et al., 1996). Thus, to analyze the characteristics of atmospheric mercury with special emphasis on its sources, transport, and depositional mechanisms, it

is especially meaningful in areas where mercury-emitting facilities are highly concentrated.

Understanding the atmospheric mercury budget in Houston is challenging. There are distinct industrial emissions, a special geographic pattern (close to the Gulf of Mexico), and complex meteorological conditions (Liu et al., 2015). A few atmospheric mercury measurements were conducted in Houston (Brooks et al., 2010), atop the University of Houston Moody Tower (MT). However, the previous research was limited to a single urban site. This study focuses on the comprehensive analysis of atmospheric mercury by investigating and comparing the factors that impact mercury mixing ratios under urban and coastal settings in the Houston area. This study contains continuous 16-months of mercury measurements together with simultaneous meteorological parameters and key trace gases data. The aims of the study were to improve our understanding of mercury pollution under different environmental settings, to investigate high mercury events, and to help evaluate the regional mercury budget in the Houston area.

Last, but not least, biomass burning is the largest global source of primary fine carbonaceous particles and the second largest source of numerous important atmospheric trace gases (Andreae and Merlet, 2001; Schultz et al., 1999). The open combustion of biomass is the key pathway by which humans directly affect the chemical and radiative properties of the atmosphere (Wooster et al., 2011). Trace gases emitted from biomass burning have a significant influence on the atmosphere (Akagi et al., 2011), especially in tropical and subtropical regions (Koppmann et al., 1997). For example, carbon monoxide (CO), methane (CH_4), and volatile organic compounds (VOCs) affect the oxidation capacity of the troposphere by reacting with OH radicals (Crutzen and Andreae, 1990).

Nitric oxide (NO) and VOC emissions have led to the formation of tropospheric ozone (O_3) and other photo oxidants. Biomass burning is also a major source of the methyl chloride (CH_3Cl), methyl bromide (CH_3Br), and a minor source of methyl iodide (CH_3I), which potentially delivers halogens to the stratosphere and causes O_3 depletion (Andreae et al., 1996). Therefore, there is an increasing need for information on comprehensive biomass-burning emissions of trace gases and aerosols.

There are only a relatively small number of studies that have reported emissions from grassland and savanna fires (Wooster et al., 2011; Shirai et al., 2003). There are even fewer studies of emission of trace gases from domestic grassland and savanna fires in the United States (Koppmann et al., 2005; Sudo et al., 2007). Full fire-lifecycle emissions are seldom measured directly.

Our experiment is unique because the sampling inlets were close (meters) to the controlled burn and we provided detailed in-situ measurements of trace gases and VOC emissions throughout the ignition, flaming, and smoldering phases of a prescribed grassland fire. Thus, this controlled experiment will add comprehensive and direct information of important trace gases and VOC emissions from biomass burning to our limited knowledge on this topic.

The over-all goal of this study was to improve the current understanding of atmospheric ozone, mercury, and biomass burning in south-central Texas.

1.2 References

Akagi S.K., Yokelson R.J., Wiedinmyer C., Alvarado M.J., Reid J.S., Karl T., Crounse J.D., and Wennberg P.O., Emission factors for open and domestic biomass burning for use in atmospheric models, *Atmos. Chem. Phys*., 11, 4039-4072, 2011.

Andreae M.O. and Merlet P., Emission of trace gases and aerosols from biomass burning, *Glob. Biogeo. Cycl.*, 955-966, 2001.

Andreae M.O., Methyl halide emission from savanna fires in southern Africa, *J. Geophys. Res.*, 101, 23, 603-23, 1996.

Brooks S., Luke W., Cohen M., Kelly P., Lefer B., and Rappengluck B., Mercury species measured atop the Moody Tower TRAMP site, Houston, Texas, *Atmos. Environ*. 44, 4045–4055, 2010.

Crutzen P.J., and Andreae M.O., Biomass Burning in the Tropics: Impact on Atmospheric Chemistry and Biogeochemical Cycles, *Sci.*, 250.49881669, 1990.

J., Hilboll A., Mellqvist J., Peischl J., Richter D., Rivera C., Ryerson T., Walega J., Warneke C., Weibring P., and Williams E., Evaluations of NOx and highly reactive VOC emission inventories in Texas and their implications for ozone plume simulations during the Texas Air Quality Study, *Atmos. Chem. Phys.*, 2011, 11, 11361-11386, 2006.

Kim S.W., McKeen S.A., Frost G.J., Lee S.H., Trainer M., Richter A., Angevine W.M., Atlas E., Bianco L., Boersma K.F., Brioude J., Burrows J.P., Gouw J., Fried A., Evaluations of NOx and highly reactive VOC emission inventories in Texas and their implications for ozone plume simulations during the Texas Air Quality Study 2006, *Atmos. Chem. Phys.*, 11, 11361-11386, 2011.

Kleinman L.I., Daum P.H., Imre D., and Lee Y.N., Ozone production rate and hydrocarbon reactivity in 5 urban areas: A cause of high ozone concentrations in Houston, *Geophys. Res. Lett.*, 29, 1467, 10, 2002.

Koppmann R., Czapiewski K., and Reid J.S., A review of biomass burning emissions, part I: gaseous emissions of carbon monoxide, methane, volatile organic compounds, and nitrogen containing compounds, *Atmos. Chem. Phys. Discuss.*, 5, 10455-10516, 2015.

Koppmann R., Khedim A., Rudolph J., Poppe D., Helas G., Welling M., and Zenker T., Emissions of organic trace gases from savanna fires in Southern Africa during SAFARI 92 and their impact on the formation of tropospheric ozone, *J. Geophys. Res.*, 10, 1029-97, 1997.

Lefer B., Rappenglück B., Flynn J., and Haman C., Photochemical and meteorological relationships during the Texas-II Radical and Aerosol Measurement Project (TRAMP), *Atmos. Environ*, 44 (2010) 4005-4013, 2010.

Liu L., Talbot R.W., and Lan X., Influence of Climate Change and Meteorological Factors on Houston's Air Pollution: Ozone a Case Study, *Atmos.*, 6, 623-640, 2015.

McGaughey G.R., Desal N.R., Allen D.T., Seila R.L., Lonneman W.A., Fraser M.P., Harley R.A., Pollack A.K., Ivy J.M., and Price J.H., Analysis of motor vehicle emissions in a Houston tunnel during the Texas Air Quality Study, *Atmos. Environ.*, 17, 1981-1989, 2004.

Ngan F., and Byun D., Trajectory analysis for source-receptor relation of high ozone events over Houston/Galveston area, paper presented at 9th Conference on Atmospheric Chemistry, *Am. Meteorol. Soc.*, San Antonio, Tex, U.S.A, 2007.

Pirrone N., Keeler G.J., and Nriagu J., Regional differences in worldwide emissions of mercury to the atmosphere. *Atmos. Environ*. 17, 2981–2987, 1996.

Rappenglueck B., Perna R., Zhong S., and Morris G.A., An analysis of the vertical structure of the atmosphere and the upper-level meteorology and their impact on surface ozone levels in Houston, Tex., *J. Geophys. Res.*, 113, D17315, 2008.

Schultz M.G., Jacob D.J., Wang Y., Logan J.A., Atlas E.L., Blake D.R., Blake N.J., Bradshaw J.D., Browell E.V., Fenn M.A., Flocke F., Gregory G.L., Heikes B.G., Sachse G.W., Sandholm Shetter, S. T., R.E., Singh H.B., Talbot R.W., On the origin of tropospheric ozone and NOx over the tropical South Pacific, *J. Geophys. Res.*, 10, 1029-1035, 1999.

Shirai T., Blake D.R., Meinardi S., Rowland F.S., Smith J.R., Edwards A., Kondo Y., Koike M., Kita K., Machida T., Takegawa N., Nishi N., Kawakami S., and Ogawa T., Emission estimates of selected volatile organic compounds from tropical savanna burning in northern Australia, *J. Geophys. Res.*, 10, 1984-2001, 2003.

Sive B. C., Zhou Y., Troop D., Wang Y., Little W.C., Wingenter O.W., Russo R.S., Varner R.K., and Talbot R., Development of a cryogen-free concentration system for measurements of volatile organic compounds, *Anal. Chem.*, 77(21), 6989-6998, 2005.

Sudo K., and Akimoto H., Global source attribution of tropospheric ozone: Long-range transport from various source regions, *J. Geophys. Res.*, 11, 1541-4562, 2007.

Wooster M.J., Freeborn P.H., Archibald S., Oppenheimer C., Roberts G.J., Smith T.E.L., Govender N., Burton M., and Palumbo I., Field determination of biomass burning emission ratios and factors via open-path FTIR spectroscopy and fire radiative power assessment: headfire, backfire and residual smouldering combustion in African savannas, *Atmos. Chem. Phys.*, 11, 11591-11615, 2011.

Chapter 2

Influence of Climate Change and Meteorological Factors on Houston's Air Pollution: Ozone a Case Study[2]

2.1 Introduction

Houston, the fourth largest city in the United States, is located on the northern coastline of the Gulf of Mexico (Feagin et al., 1985). It routinely experiences some of the highest ozone (O_3) mixing ratios in the United States over the past several decades (Kleinman et al., 2002). Due to this, Houston has been classified by the U.S. Environmental Protection Agency as a "severe" 8-h O_3 nonattainment area in 1997 and a "marginal" 8-h O_3 nonattainment area in 2008. Houston experienced significant variability in both the peak O_3 mixing ratios and the number of high O_3 days (Lefer et al., 2010). Houston exceeds the 75 ppbv 8-h and 124 ppbv 1-h National Ambient Air Quality Standard (NAAQS) for ground-level O_3 mixing ratios dozens of days a year over last two decades.

The Texas Commission on Environmental Quality (TCEQ) treats the O_3 mixing ratio at a given location as the sum of the background mixing ratio and the contribution from local O_3 production (Gammon et al., 2005). Background O_3 levels in eastern Texas are typically higher during late summer and early fall as northerly and easterly flows

[2] Material in this chapter was published in:

Liu, L., Talbot R., and Lan X., Influence of Climate Change and Meteorological Factors on Houston's Air Pollution: Ozone a Case Study, Atmos., 6, 623-640, 2015.

associated with synoptic scale transport of O_3-rich continental air to the region (Berlin et al., 2013). This increased regional background contributes to the frequency and severity of high-O_3 episodes in Houston.

Air pollution in the Houston area is a product of strong emissions coupled with specialized meteorological conditions (McGaughey et al., 2004). Automobiles and industrial sources along the Houston Ship Channel (HSC) area and in outlying areas of the city emit large amounts of highly reactive volatile organic compounds (HRVOCs) and nitrogen oxides ($NO + NO_2 = NOx$) (Kim et al., 2011), which provides the ingredients necessary for ground-level O_3 production in the presence of heat and sunlight (Seinfeld et al., 1998).

More than 400 chemical manufacturing facilities and two of the four largest refineries in the U.S. reside in the Houston Ship-Channel area (Streutker et al., 2003). As a world-class city, the population of Houston increased 29% in the past two decades (Frank et al., 2006). This has led to increased vehicular traffic and associated NOx emissions (Glynis et al., 2005). Inevitably, this caused environmental problems, especially with regard to air pollution. Air pollution effects the health of human beings (Walker et al., 1982), impacts radiative transfer in the atmosphere (Varotsos et al., 2012), and how much solar ultraviolet radiation reaches the ground (Chubarova et al., 2004; Tzanis et al., 2009). Houston has moved from #7 to #6 in the rankings of the worst O_3 in the U.S., which is based on the number of days with elevated pollution levels. As the air pollution conditions grew worse, researchers and policy makers are starting to pay attention to this topic. In 2000, the city of Houston started an emission reduction plan that

focused on reduction of NOx emissions from industry and motor vehicles. The National Oceanographic and Atmospheric Administration (NOAA) conducted two airborne studies in the Houston area; Texas Air Quality Study I 2000 and the Texas Air Quality Study II—the Gulf of Mexico Atmospheric Composition and Climate Study 2006. These studies involved both measurements and modeling to unravel the complexity of air pollution in Houston and especially to understand what was driving the unusually high O_3 production in the area.

Meteorology also plays a critical role in O_3 formation, which either dilutes pollutant emissions or allows them to accumulate, and it can also affect other key processes, such as chemical reaction rates (Cheng et al., 2007; Rappenglueck et al., 2008). Previous studies have shown that levels of O_3 precursors are substantially elevated during post-frontal environments or in the presence of anti-cyclonic conditions where weak winds, clear skies, and subsidence dominates (Ngan et al., 2007).

In this dissertation, we characterized various meteorological variables including temperature, wind speed, wind direction, and pressure for both high and low O_3 events over the past 23 years (from January 1990 to December 2013). We obtained an in-depth understanding about the relationship between the climate/meteorology factors and O_3 mixing ratios in the Houston area. Because Houston is located (latitude 30°) near the northern coast of the Gulf of Mexico, it is known that ground-level O_3 mixing ratios could be affected significantly by the land-sea breeze (Banta et al., 2005).

We choose four sites along the South-North direction in the Houston area. We mainly emphasized trends of ground-level O_3 mixing ratios, background O_3 mixing ratios, wind speed, wind direction, temperature, and pressure. A critical question to answer is, which is the key meteorology factor that influences concentration of ground-level O_3 on a large time scale in the Houston area?

2.2 Results and Discussion

2.2.1 Background Ozone

Background O_3 is the mixing ratio of O_3 in the absence of direct influence by local anthropogenic emissions in an area. Currently, the 8-h O_3 standard is 75 ppb (the 84 ppb standard was changed in 2008), the ongoing reduction of 1-h and 8-h standards makes the level of background O_3 more important. Background O_3 levels vary with time of day, over months, and across large time spans of a decade or more. Changes in natural and anthropogenic sources during long-range atmospheric transport will ultimately influence local O_3 levels. In the Houston area, background O_3 mixing ratio trends are flat or decreasing, and vary greatly with transport patterns. For example, the flow of air from over the Gulf of Mexico may play an important role in the Houston background O_3 levels. Carbon monoxide is an excellent anthropogenic tracer because it mostly comes from mobile combustion (Mao et al., 2012). Air masses with CO mixing ratios below the 25th percentile value are commonly considered background air (Mao et al., 2012). In this study, we used the 20th percentile of concurrently measured carbon monoxide (CO) and O_3 to ascertain background O_3 (Mao et al., 2010). These measurements were performed atop Moody Tower on the

University of Houston campus over the time period of January 2008 to January 2014. Figure 2.1 shows a time series of the background O_3 mixing ratios in urban Houston.

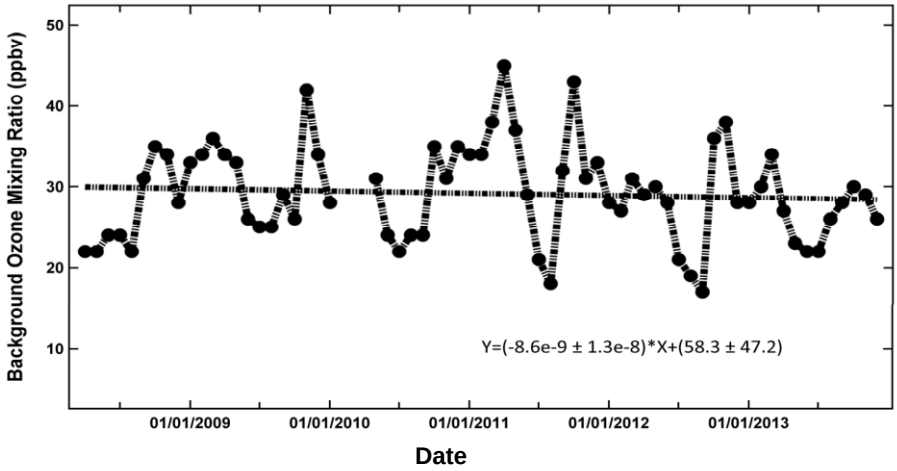

Figure 2.1. Monthly averaged background O_3 mixing ratios measured atop Moody Tower on the University of Houston campus.

Background O_3 ranged between 15 ppbv and 45 ppbv, with an average of 30 ppbv and the highest values occurring in spring and lowest in June or July. During the summer there is strong southerly flow off the Gulf of Mexico bringing "cleaner" air inland. The overall trend-line shows that background O_3 is fairly constant with a slight decrease of ~1 ppbv over the past seven years.

2.2.2 Exceedance Days of 1-h / 8-h Averaged O_3 Mixing Ratio

We analyzed data from the four research sites around the urban Houston. According to the revised National Ambient Air Quality Standards (NAAQS) by the Environmental Protection Agency (EPA) in 2011, for ground-level O_3 if there is at least one 1-h averaged surface O_3 mixing ratio exceeding 124 ppbv or an 8-h average exceeding 75 ppbv, the day is regarded as an exceedance day.

In Figure 2.2 we illustrate the number of exceedance days of 1-h and 8-h averaged

ground-level O_3 for each year during the research period 1990 to 2013 for our four sites. The four sites' number of exceedance days of 1-h O_3 and 8-h O_3 remained with wide year-to-year variations. The most northern sites (Aldine and Northwest Harris) have higher occurrences of exceedance days than the sites to the south (Clinton and Galveston). Surface O_3 is a secondary product that is formed during transport, and under southerly winds the highest O_3 would be expected in the northern part of the study area.

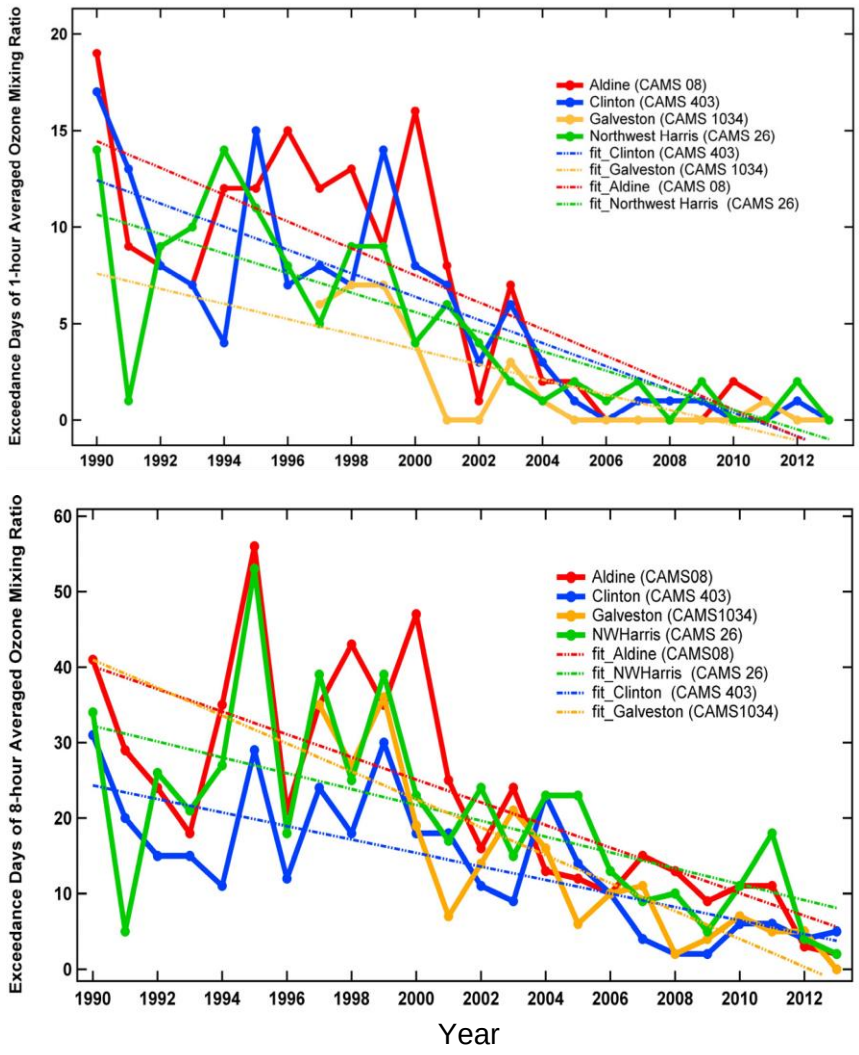

Figure 2.2. Annually exceedance days of 1-h averaged (a) and 8-h averaged (b) O_3 mixing ratios during 1990–2014 for four sites.

The dashed lines on Figure 2.2 are the linear trend lines of the exceedance days over the 23 year period. The slopes of the 1-h and (8-h) trend lines are −0.69 $year^{-1}$ (−1.5 $year^{-1}$) (Aldine), −0.50 $year^{-1}$ (−1.0 h^{-1}) (Northwest Harris), −0.60 $year^{-1}$ (−0.90 $year^{-1}$) (Clinton), and −0.39 $year^{-1}$ (−1.8 $year^{-1}$) (Galveston). From Figure 2.2, we noticed that around the year of 2000, the number of exceedance days at all sites dropped dramatically. After 2000, the number of exceedance days remained steady in the low single digits. We attribute a reduction in emissions for part of this transition to lower O_3 mixing ratios in Houston. We divided the time period shown in Figure 2.2 into two stages: the first stage was 1990–2000 and the second stage was 2001–2013. We calculated the average number of exceedance days for each site during the two stages. As Table 2.1 shows, the average number of exceedance days at Aldine decreased from 12 to 2 (1-h) and from 35 to 11 (8-h); at Clinton they decreased from 10 to 2 (1-h) and 20 to 8 (8-h); NW Harris they decreased from 9 to 1 (1-h) and 28 to 13 (8-h); at the Galveston site they decreased from 6 to 1 (1-h) and from 29 to 8 (8-h). The average number of exceedance days during stage II was reduced to about one-fifth of the stage I for 1-h averaged O_3, and reduced to half of its original value for the 8-h averaged O_3.

Table 2.1. Average Number of Exceedance Days per Site 1-h (8-h)

Site	**1990–2000**	**2001–2013**
Aldine	12 (35)	2 (11)
Clinton	10 (20)	2 (8)
NW Harris	9 (28)	1 (13)
Galveston	6 (29)	1 (8)

2.2.3 Southerly Flow and Ground-Level O_3

We analyzed the long-term relationship between ground-level O_3 mixing ratio and meteorological factors, including temperature, pressure, and wind speed. However, we did not find any significant relationships. The analyzed results can be found in the Supplementary Material (Figures S2.1. and Figure S2.2.).

According to the research of Banta et al., 2005, summertime meteorological conditions in Houston involve interactions between sea-breeze circulation patterns. The sea-breeze cycle at 30° N latitude is at its maximum amplitude, and plays an especially strong role for atmospheric advection in the Houston area. There are two forms of sea breeze in Houston: (1) the superposition of large-scale flow with inertia-gravity wind oscillation; and (2) under suitable conditions of wind and temperature, the sea breeze can assume a frontal structure. Both of these can produce winds inland away from the shore. Banta et al., 2005 and Rappengluck et al., 2008 showed that under specialized conditions (e.g., timing, location, and the height to which pollutants mix), the pollutants that have been carried offshore by the land breeze can be brought back over land by the sea breeze. Southerly winds typically bring in "cleaner" marine air with lower precursors (e.g., NOx, CO, and hydrocarbons) and lower background levels of O_3.

Especially in the summer and fall seasons, the southerly flow can influence local air quality conditions. A common pattern found was, in the early morning, northerly winds push polluted air masses aloft in the Galveston area, which is located next to the Gulf of Mexico. Around noontime to the early afternoon, because of the increased solar radiation and the higher heat capacity of water, land temperatures increase faster than water temperatures, and the sea breeze (southerly flow) with relative "cleaner" air, which

originated over the Gulf of Mexico begins to appear over the city. According to our data analysis, in the late afternoon, especially during 2:00 p.m. ~ 5:00 p.m. in summer and fall seasons, the air temperature and the frequency of southerly flow reaches its peak. However, at night, air temperatures decrease dramatically because of the lack of solar radiation. Along with it, there is a disappearance of the sea breeze and northerly winds take over again (i.e., the land breeze). Local emissions trapped under a shallow nocturnal planetary boundary layer (PBL) accelerate the accumulation of pollutants in downtown Houston and the Houston-Ship-Channel areas.

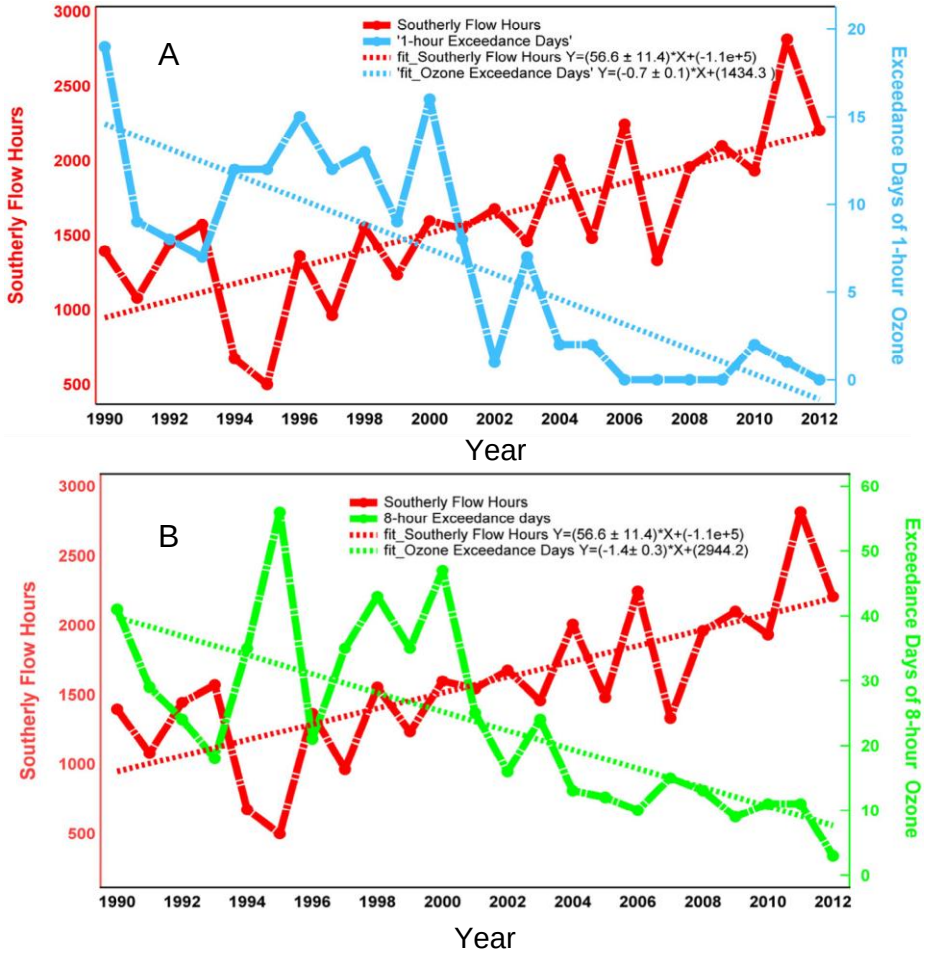

Figure 2.3. (A) 1-h and (B) 8-h exceedance days as a function of annual southerly flow hours per year at the Aldine site.

To further investigate the variations of southerly wind, we defined the range of wind directions for southerly flow as 160°–200° and only examined the wind data during March-October, the southerly flow season. We used meteorological data from the NOAA Climate Data Center, which provided one-hour averaged wind speed and wind direction. In order to get an in-depth understanding, we contrasted the two factors. The relationship between annually number of exceedance days and hours of southerly flow per year is depicted in Figure 2.3 (Aldine) and Figure 2.4 (Clinton). The anti-correlation between these two parameters is striking, and shows that the length of time per year Houston is under the influence of southerly flow has more than doubled from 1990 to 2013. The correlation coefficient between annually southerly flow hours and annually number of exceedance days of 1-h averaged (8-h averaged) in Aldine site are −0.63 (−0.72), for Clinton site are −0.56 (−0.51). All of them pass the significant test ($p < 0.05$). The slope of the linear regression line for 1-h exceedance days at Aldine is −0.71 exceedances year^{-1} and −0.90 exceedances year^{-1} at Clinton. Conversely, the slope for Aldine is +56.6 year^{-1} and +16.8 year^{-1} for Clinton. Similar relationships for the two other sites can be found in the Supplementary Material (Figures S2.3 and S2.4). The Clinton site is near downtown Houston and the ship channel area where many refineries and petrochemical industrial plants are located. In addition, the slope of southerly flow hours is more than three time greater at Aldine than at Clinton. These nearby sources and reduced dilution likely supplied more O_3 precursor compounds to this site and slowed the trend in decreased O_3.

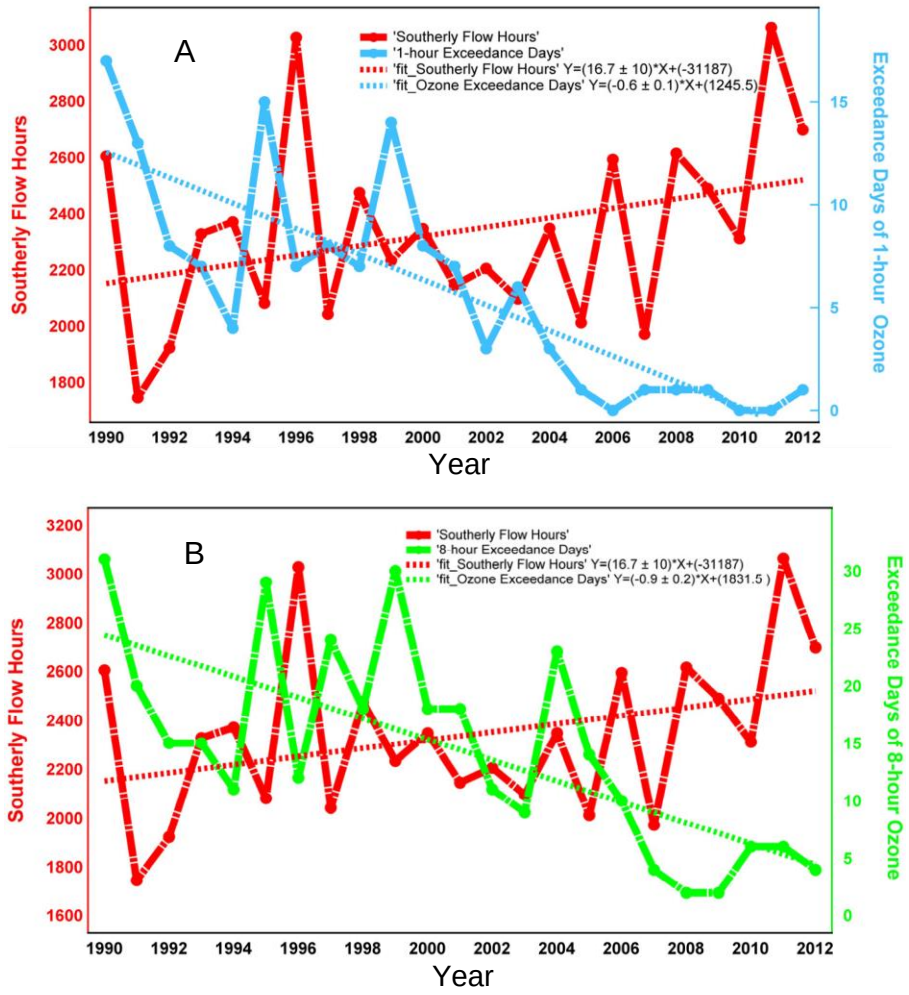

Figure 2.4. (A) 1-h and (B) 8-h exceedance days as a function of annual southerly flow hours per year at the Clinton site.

We propose that the increased flow of "cleaner" air is diluting the dirty Houston air, lowering the mixing ratios of NOx, O_3, and precursor hydrocarbons. It also would advect the polluted air away from Houston. Both of these processes would lead to a lower potential to produce O_3 in the Houston area. The significantly increased southerly flow together with lower emissions is leading to a "cleaner" O_3 environment. The general correspondence between increased exceedance days and decreased southerly flow hours

give credence to our hypothesis. For example, the 8-h peak value was 55 with the corresponding low in southerly flow hours of 500 (Figure 2.3).

2.2.4 Contrasting Southerly Flow Frequencies

We have documented increased southerly flow hours from 1990 to 2013, and now will examine this in terms of southerly flow days and averaged daily southerly flow hours. Around the year 2000, there was a decrease in the number of exceedance days; they dropped dramatically and decreased by a factor of three on average. After 2000 the number of exceedance days decreased to single digits, meanwhile southerly flow hours increased steadily by a factor of two. Based on the changes, we divided the time series into two stages: 1990–2000 and 2001–2013. In each stage, we choose two sample years when most of the data were close to the trend-line and with good representatives. We choose 1995 and 1996 for stage I, and 2010 and 2011 for stage II. The data of the sample years were averaged to better compare the southerly flow between the two stages. We compared Aldine site located north of the urban Houston area and the Galveston site close to the Gulf of Mexico (Figure 2.5). Southerly flow mainly occurs in summer and fall season when the sea surface temperature has the largest gradients with land temperature. We examined the data from March–October to cover the period of southerly flow conditions. It was apparent at both sites that annually southerly flow hours have increased dramatically, by as much as a factor of 2–3. The inland sites experienced greater increases in southerly flow hours than the Galveston site. Both of the two sites had the strongest southerly flow in May, June, and July. In 2010 and 2011, the Aldine site had the strongest southerly flow in April and June, slightly earlier in the year.

In Galveston, 65% of the southerly flow occurred in summertime, specifically, in June, July, and August. Annually southerly flow hours in June (from 200 to 350), August (from 120 to 380), and October (from 60 to 200) increased the most, increasing by a factor of 2.5 on the average. In the summer season, southerly flow dominates in Galveston.

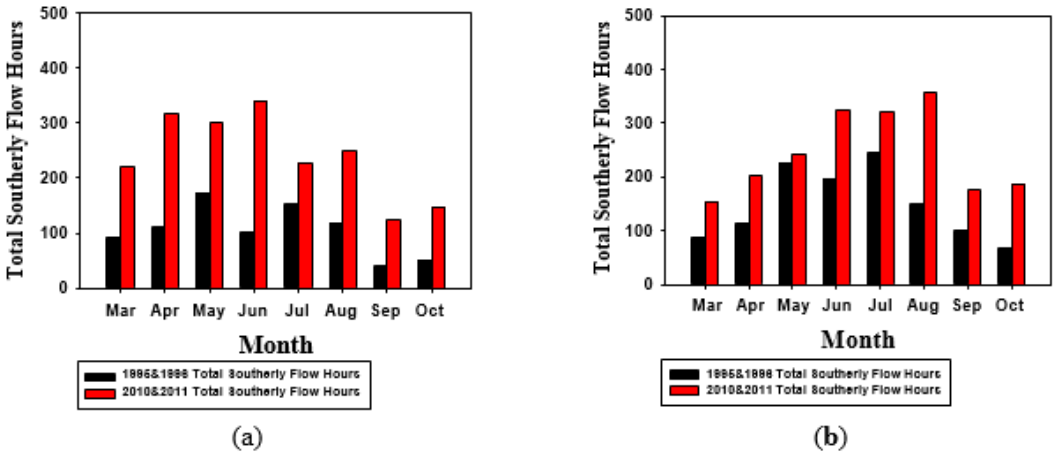

Figure 2.5. Total southerly flow average hours in 1995–1996 (black) and 2010–2011 (red) at Aldine (a) and Galveston (b).

Figure 2.6 shows that from March to October, total southerly flow days in 2010 and 2011 happened more frequently than that in 1995 and 1996. For both sites, the southerly flow days increase in each month during two sample periods. At the Aldine site, total southerly flow days increased most in March and October, in March, the southerly flow days increased from 13 days to 20 days, and in October, increased from 6 days to 22 days, it is an increase more than a factor of three. At the Galveston site, most increase occurred in October, from 9 days to 20 days, increasing by a factor of two.

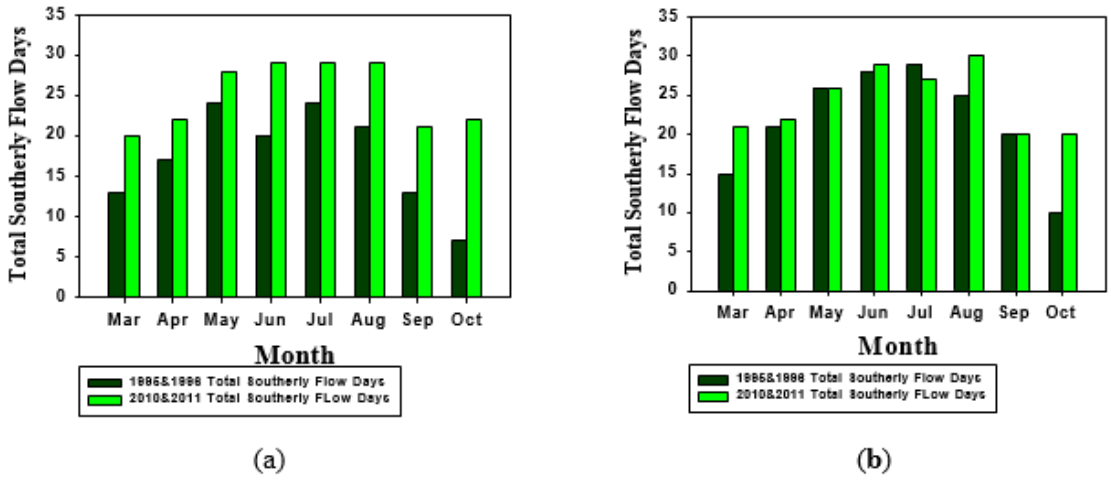

Figure 2.6. Days with southerly flow at Aldine (a) and Galveston (b) average over 1995–1996 (dark green) and 2010–2011 (light green).

To better understand the southerly flow occurrences at the Aldine and Galveston sites, we analyzed the daily southerly flow hours for the two locations (Figures 2.7 and Figure 2.8). It increased in each month between the two sample periods for both sites. At the Aldine site, especially in April (increase from 6 to 15), May (increase from 7 to 11), and June (increase from 5 to 13), daily southerly flow hours increase by a factor of two in average contrasting the two periods. For the Galveston site, most increases occur in April (increase from 5 to 9), August (increase from 6 to 12), and September (increase from 2 to 7). The results for the other sites are presented in the Supplementary Material (Figures S2.5 and S2.6). It is interesting to find out that the daily southerly flow hours have increased the most in the spring and fall seasons at the Aldine and Galveston sites. These are the type of trends we would expect with a warming climate (Timmermann et al., 1999).

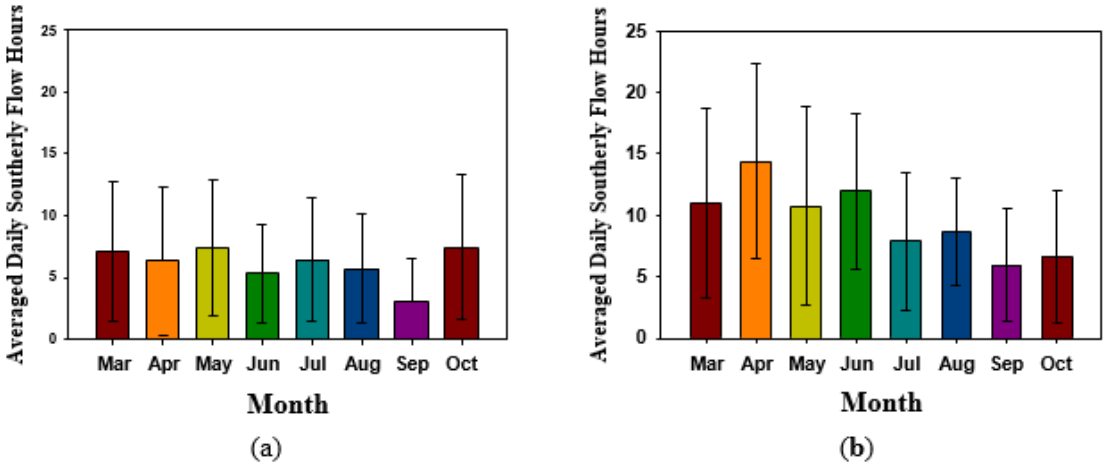

Figure 2.7. Daily southerly flow hours at Aldine during 1995–1996 (a) and 2010–2011 (b).

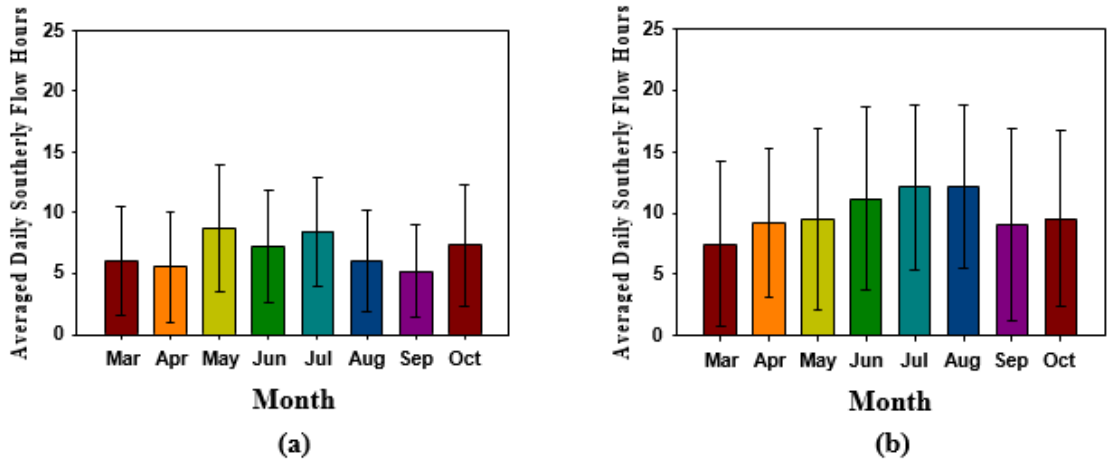

Figure 2.8. Daily southerly flow hours at Galveston during 1995–1996 (a) and 2010–2011 (b).

In order to get a better understanding of the variation in wind direction over past decades, we constructed wind rose graphs for the Houston area. Because there are not sufficient meteorological data to cover the 23 years research time period in the O_3 sites, we used the meteorological data from the nearest NCEP monitoring site, and detailed site information, available in the experimental section. The hourly wind speed and wind direction data are available from National Center for Environmental Protection

(NCEP). We choose four sites: George Bush Airport (north), Galveston (southeast), William Hobby Airport (near downtown) and David Wayne Hooks Memorial Airport (north). Figure 2.9 shows the wind rose for the George Bush Airport site. The other three sites can be found in the Supporting Materials (Figures S2.7 – S2.9). We define the frequency of wind direction based on the formula $g = \frac{\mathrm{f}}{\mathrm{c}+\sum_{n=1}^{16} f}$ (Fryberger et al., 1979), where g is the frequency of wind direction N, f is the number of occurrences of the wind direction N for this period and c is the static wind frequency. We choose March to October during 1990~2013 as the time period when southerly flow is most active. Then, the time period was divided into five time intervals and the average for each was calculated. In the rose graph of 1990–1994, general wind directions were from the north (25%), and south and southeast (40%). Wind speeds were generally between 4 and 6 m/s (65%). During 1995–1999 and 2000–2004, major wind directions shifted to the south and southeast. The highest wind speed (8–10 m/s) occurred in the direction of 130°–165°.

During the period 2005–2009, major wind directions were distributed among 160°–195° (32%), which is southerly wind. Wind speeds were in the range of 6–8 m/s (24%) and 13% fell into the range of 8–10 m/s. The frequency and wind speed of the southerly flow increased in contrast to the previous three time intervals. The last interval of 2010–2013, 60% of the wind directions accumulated between 130° and 195°. Specifically, for the directions from 160° to 180°, 30% of the wind speeds were distributed among 6–10 m/s with 5% being in excess of 10 m/s. In summary, the strength of the sea breeze system intensified.

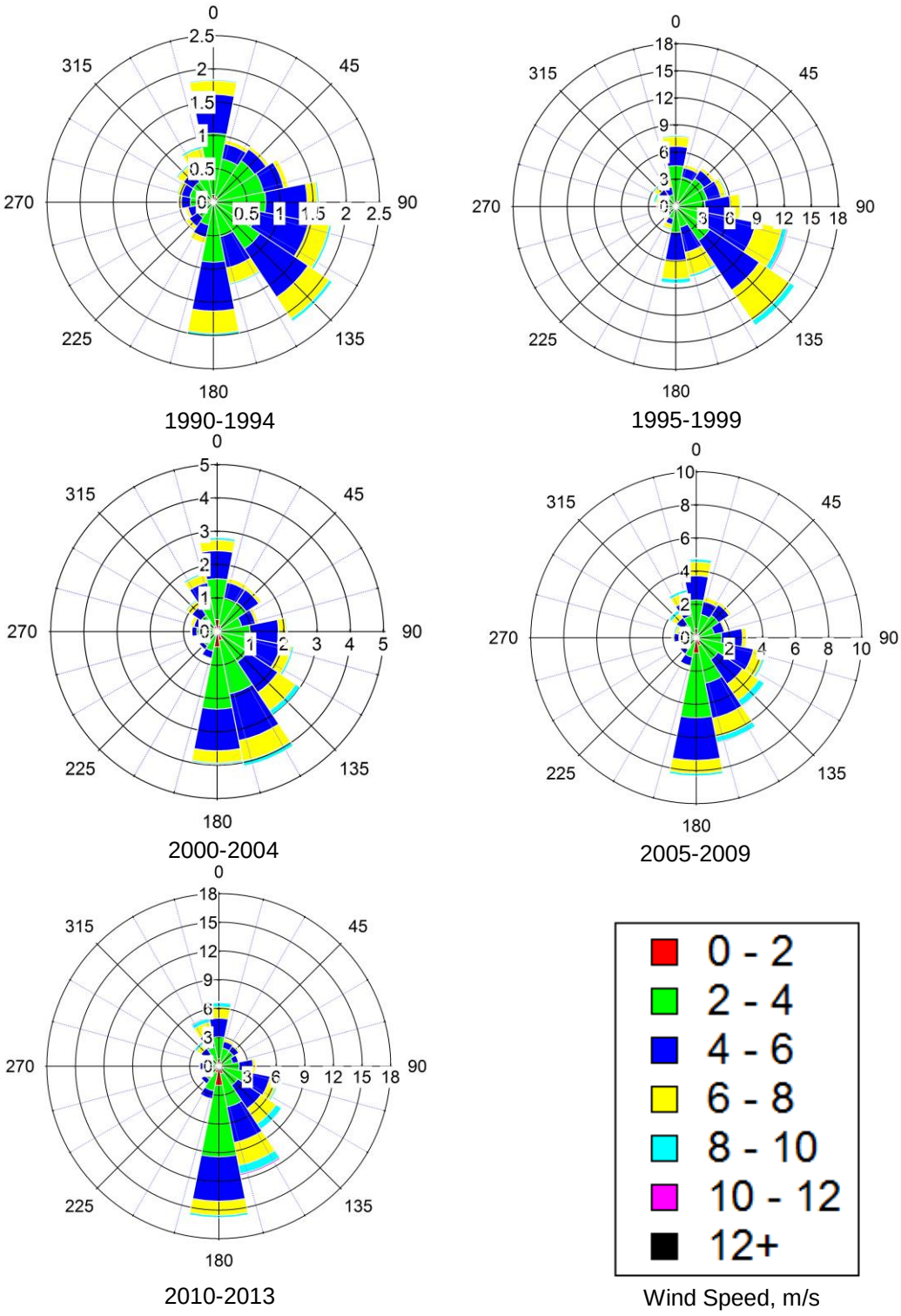

Figure 2.9. Wind speed and direction as a function of time for George Bush Airport site.

2.2.5 Why an Increase in Southerly Flow?

2.2.5.1 LST / SST Difference

Both the frequency and wind speed of southerly flow has increased in the most recent two decades, especially during 2000–2013 in the Houston area. As we mentioned previously, the sea breeze usually occurs in the afternoon because of the heat capacity of water is larger than that of soil (Noborio et al., 1996), which contributes to the temperature differences between land and ocean. To investigate how temperature differences impact southerly flow, we compared land and sea temperatures for the past twenty-three years. Southerly flow occurs mostly from March to October, so we examined hourly land and sea surface temperature data from our study sites. The sea surface temperature (SST) using data from two buoy sites located at the western Gulf of Mexico operated by NOAA National Data Buoy Center.

We used monthly averaged land/sea surface temperature difference in our analysis. We choose the hourly land surface temperature data during 2:00 p.m.–5:00 p.m. (local time) from 1 March to 31 October during 1990–2012, we firstly averaged hourly LST data to get the daily data for each site. Then we averaged the four land sites' daily data, which is the land surface temperature data for a day. We repeated the processes for each day from March to October during 1990–2012. For the SST, the research time period and the method of analysis was the same as for LST. At last, daily LST data was subtracted by daily SST data, then, I calculated the monthly averaged temperature difference between LST and SST.

Figure 2.10 depicts the temperature difference between LST and SST. The largest differences occurred in May and June and these are shown individually in the supporting

information (Figure S2.10). Before the year of 1998, the amplitude of temperature difference between the LST-SST was −8 °C to 2 °C, however, a change occurred on September 1998. After the change point, during 1999 to 2012, the amplitude increased to 24 °C (−12 °C to 12 °C), with a high pronounced variability with an unknown cause. The increased variability was not caused by changing out of the measurement devices at any of our study sites. We divided the time period into two stages, the first stage during 1990–1998 and the second stage during 1999–2012. We calculated out the average temperature difference between land and sea for each stage, during 1990–1998, the number was −1.2 °C and during 1999–2012, the average temperature difference was 0.4 °C, an increase of 1.6 °C. The regression trend-line increased from −2 °C to 2 °C during 1990–2013.

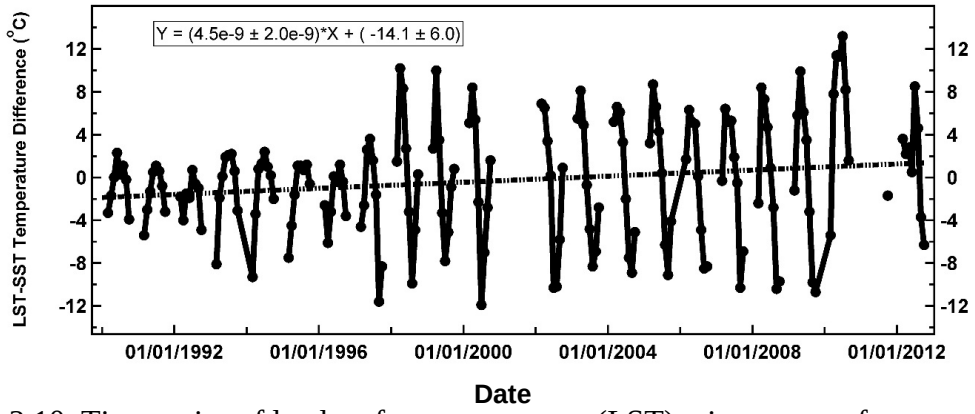

Figure 2.10. Time series of land surface temperature (LST) minus sea surface temperature (SST) for the Houston area.

For the trend of southerly flow wind speed, as shown in Figure 2.11., we analyzed the four land meteorological sites' wind speed data with wind directions between 160° and 200° and the southerly flow wind speed data were selected from the time period of 2:00 p.m.–5:00 p.m. (local time) from March to October during 1990–2012. After we

averaged the four sites' daily southerly flow wind speed data (average spatially), we calculated average monthly southerly flow wind speeds. The trend line shows monthly average southerly flow wind speed increased by 0.3 m/s from 1990 to 2012. The peak value of the monthly average southerly flow wind speed was 5.8 m/s, which occurred in June of 2012. In summary, the frequency of the southerly flow is intensified and the wind speed of the southerly flow was stable or increased slightly over the last two decades in the Houston area.

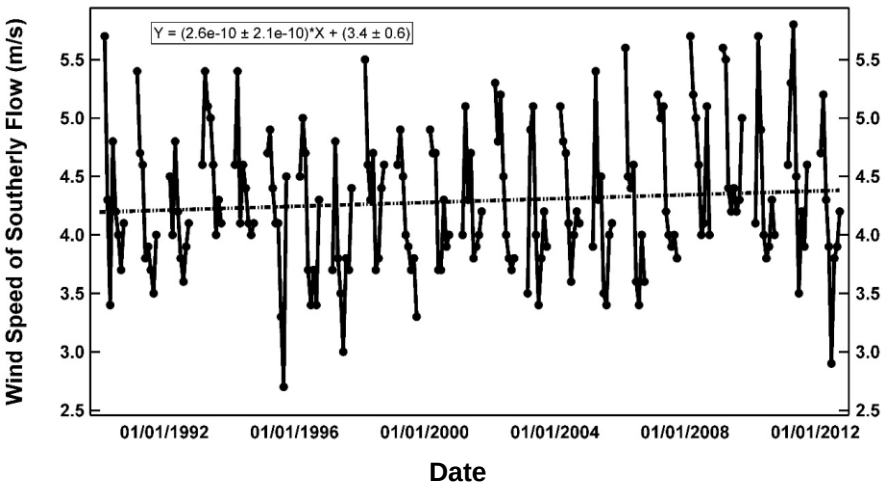

Figure 2.11. Time series of the monthly averaged wind speed of southerly flow for the Houston area.

2.2.5.2 Large Scale Atmospheric Circulation

To ascertain what processes caused increased southerly flow in the Houston area, we examined the mean sea-level pressure maps for March–October 1995–1996 and 2010–2011. The data were obtained from the National Center for Environmental Prediction and are shown in Figure 2.12. We define the ranges between 120° W–50° W and 50° N–20° S. Comparison of the two time periods indicates that the land surface pressure in Houston during 1995 and 1996 was 1015.5 hPa, during 2010 and 2011 it

decreased to 1014.5 hPa. The surface pressure over the Gulf of Mexico, especially around the Houston area, was 1013.5 hPa during 1995 and 1996 and 1015.5 hPa during 2010 and 2011. The terrestrial high-pressure system, which located over Louisiana decreased from 1017.5 hPa to 1016.5 hPa. In summary, surface pressure over the Gulf of Mexico increased while surface pressure over Houston decreased. This pressure difference between land and the Gulf of Mexico probably contributes to increased southerly flow around the Houston area. According to a previous study, eastward displacement of the Bermuda High in 2010 and 2011 may be responsible for reduced summertime O_3 along the U.S. east coast during the past decade (Lai et al., 2012).

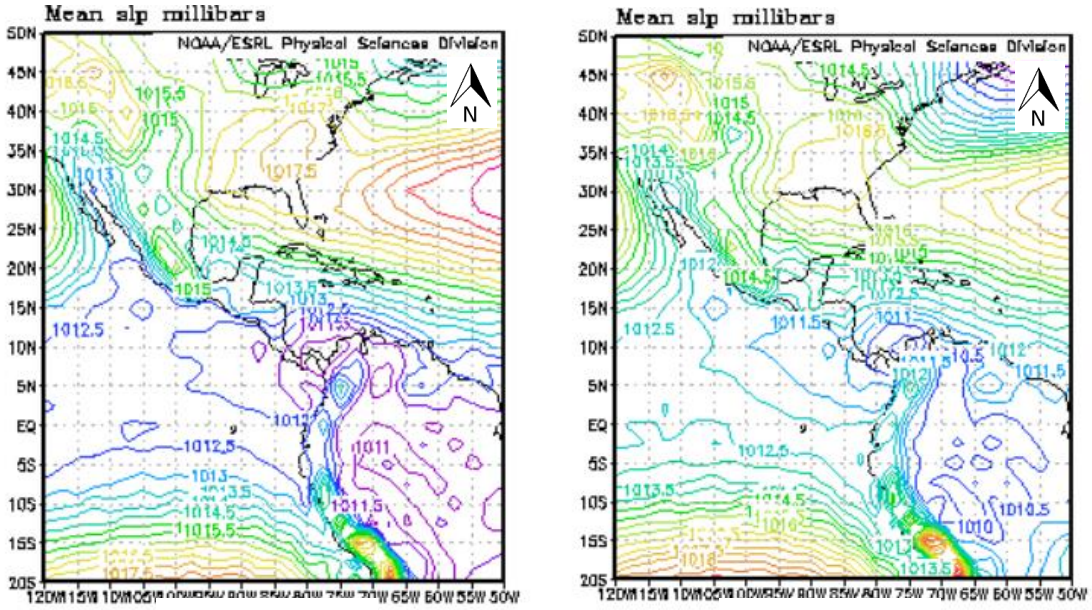

1995 & 1996 2010 & 2011

Figure 2.12. National Center for Environmental Prediction (NCEP) reanalysis mean sea-level pressure for March-October in 1995 and 1996 and 2010 and 2011.

2.3. Experimental

For the ground-level O_3 mixing ratio data, along a south to north transect, we chose four CAMS (continuous ambient monitoring station) sites, which are operated by

the Texas Commission on Environmental Quality (TCEQ); they are CAMS 1034 Galveston, CAMS 403 Clinton Ave., CAMS 08 Aldine and CAMS 26 Northwest Harris. The time period for the ground-level O_3 mixing ratio begins 1 January, 1990 and ends 31 December, 2013. The format of the O_3 data was one-hour averages.

The spatial distribution of our study sites is given in Figure 2.13. For the meteorological data, because of insufficient data to cover the 23 years' research time period in the sites by TCEQ, we choose four meteorological monitoring sites closest to the O_3 sites. These sites are operated by the NOAA National Climatic Data Center. In correspondence with the TCEQ O_3 sites, the meteorology sites are at Galveston (29°16′32.24″ N and 94°50′9.46″ W), William Hobby Airport (29°39′14.79″ N and 95°16′35.81″ W) (Clinton O_3 site), George Bush Intercontinental Airport (29°59′27.13″ N and 95°20′12.70″ W) (Aldine O_3 site), and David Wayne Hooks Memorial Airport (30° 3′31.68″ N and 95°33′2.49″ W) (Northwest Harris O_3 site). The time period for the meteorology data cover the same time period with ground-level O_3 mixing ratio data, which begins 1 January 1990 and ends 31 December 2013. The format of the data was one-hour averages. We analyzed the meteorological factors as local temperature, wind direction, wind speed, pressure, atmospheric circulation, and the land-sea breeze. The procedures for the O_3 and CO analysis are provided in (Lan et al., 2014). Sea-level pressure was provided by the NCEP/NCAR reanalysis datasets.

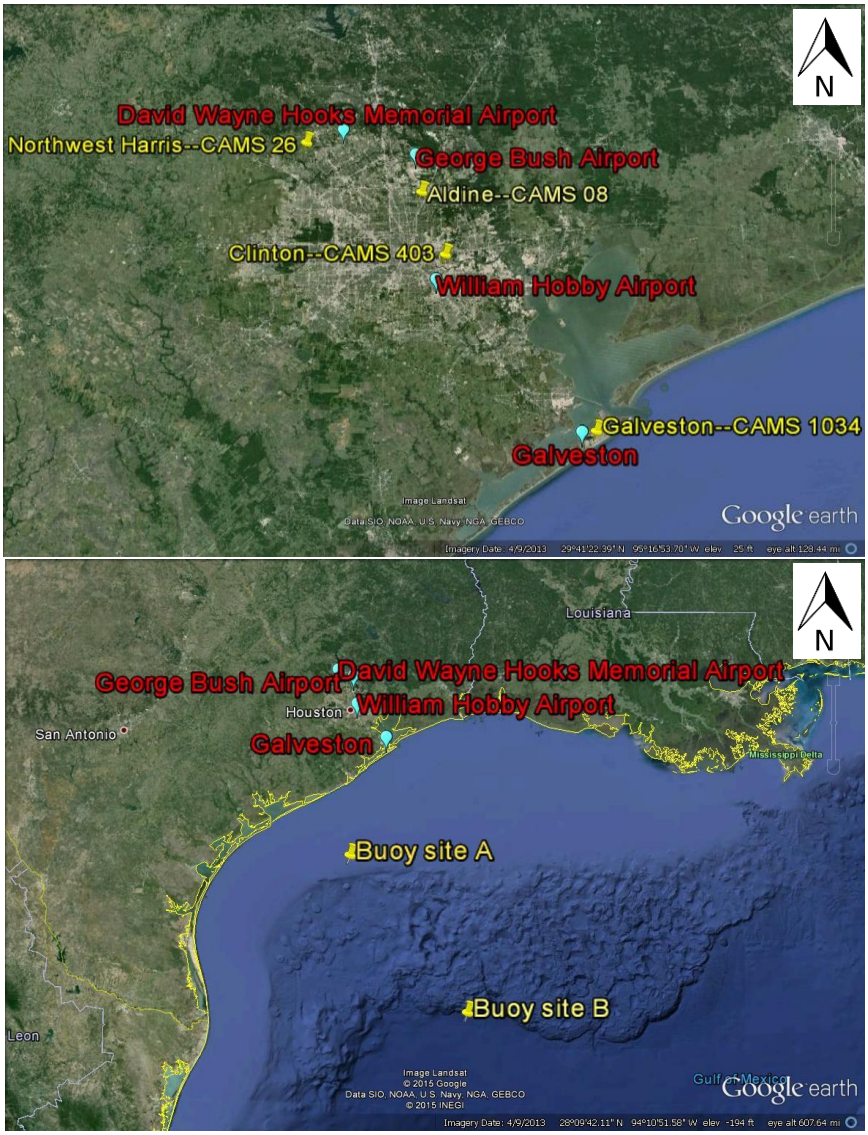

Figure 2.13. Spatial distribution of study sites.

To the land/sea surface temperature difference, the land surface temperature data is offered by NOAA meteorological sites we choose along the south to north direction (Figure 2.12). We choose two buoy sites (27°54′25″ N and 95°21′10″ W, 26°5′29″ N and 93°45′29″ W) operated by NOAA located in the Gulf of Mexico, which offer the sea surface temperature data.

2.4. Conclusions

Houston is located close to the Gulf of Mexico and at latitude of 30° N. It is home to a large amount of petroleum industries, which produce and emit chemical precursors for the production of ground-level O_3. Because of the critical role meteorology plays in controlling ground-level O_3 mixing ratios, we examined it with regard to the rapidly decreasing number of annual O_3 exceedances in Houston. Background O_3 mixing ratios in Houston are flat or decreasing slightly around 30 ppbv. The exceedance days of 1-h/8-h averaged O_3 mixing ratio decrease dramatically from tens of days to only a couple of days annually. A rapid shift occurred around 2000.

Southerly flow has been increasing in the Houston area since at least 1990. Both the frequency and the wind speed of the southerly flow have increased. During 2010~2013, 60% of the wind direction was concentrated in the range of 130°–195°, which is south wind or southeast wind, from the Gulf of Mexico. The cause for increased southerly flow is an increase of nearly 3 °C in LST compared to the SST of the ocean. The net temperature difference between LST and SST increased by a factor of four in May and by a factor of two in June. Before 1999, the range between the maximum and minimum was 12 °C, however, between 1999 and 2012, the range increased to 20 °C, with a pronounced increase in variability. We suspect that this is a worldwide phenomenon.

2.5. Acknowledgments

The authors would like to express their gratitude to the Texas Commission on Environmental Quality for providing us CAMS data sets, and thanks NOAA/NCEP for providing meteorological and buoy data. In particular, thanks to Barry Lefer for chemical

data and Xun Jiang at the University of Houston for valuable guidance. We especially thank Senior Air Quality scientist Mark Estes at the TCEQ for valuable discussions and help.

2.6. References

Banta R.M., Senff C.J., Nielsen G., Darby L.S., Ryerson T.B., Alvarez R.J., Sandberg S.P., Williams E.J., and Trainer M., A bad air day in Houston. *Bull. Am. Meteorol. Soc.*, 86, 657–669, 2005.

Berlin S.R., Langford A.O., Estes M., Dong M., Parrish D.D., and Magnitude J., Decadal Changes, and Impact of Regional Background Ozone Transported into the Greater Houston, Texas Area. *Environ. Sci. Tech.*, 47, 13985–13992, 2013.

Cheng C.S., Campbell M., Li Q., Li G., Auld H., Day N., Pengelly D., Gingrich S., and Yap D., A synoptic climatological approach to assess climatic impact on air quality in south-central Canada. Part I: Historical analysis. *Water Air Soil Pollut.*, 182, 131–148, 2007.

Chubarova N.E., Influence of aerosol and atmospheric gases on ultraviolet radiation in different optical conditions including smoky mist of 2002. Dokl. *Earth Sci.*, 394, 62–67, 2004.

Feagin J.R., The Global Context of Metropolitan Growth: Houston and the Oil Industry. *Am. J. Sociol*., 90, 1204–1230, 1985.

Frank L.D., Sallis J.F., Conway T.L., Chapman J.E., Saelens B.E., and Bachman W, Many Pathways from Land Use to Health: Associations between Neighborhood Walkability and Active Transportation, Body Mass Index, and Air Quality. *J. Am. Plan. Assoc.*, 72, 75–87, 2006.

Fryberger S.G., Dean G., In A Study of Global Sand Seas; U.S. Government Print Office: Washington, DC, USA; pp. 8–17, 1979.

Gammon N.J., Tobin J., McNeel A., and Li G., A Conceptual Model for Eight-Hour Exceedences in Houston, Texas. Part I: Background Ozone Levels in Eastern Texas; Houston Advance Research Center: The Woodlands, TX, USA, p.52, 2005.

Glynis C.L., James J.S., Martin M.S., Jeffrey T.D., and Jason P.W., Emission of Metals Associated with Motor Vehicle Roadways. *Environ. Sci. Tech*., 39, 826–836, 2005.

Kim S.W., McKeen S.A., Frost G.J., Lee S.H., Trainer M., Richter A., Angevine W.M., Atlas E., Bianco L., and Boersma K.F., Evaluations of NOx and highly reactive VOC emission inventories in Texas and their implications for ozone plume simulations during the Texas Air Quality Study, *Atmos. Chem. Phys.*, 2011, 11, 11361–11386, 2006.

Kleinman L.I., Daum P.H., Imre D., and Lee Y.N., Ozone production rate and hydrocarbon reactivity in 5 urban areas: A cause of high ozone concentrations in Houston. *Geophys. Res. Lett.*, 29, 1467, 2002.

Lai T.L., Talbot R.W., and Mao H., Two extreme ozone events in New England during 2000–2010: Meteorological influences. *Atmos.*, 3, 59–86, 2012.

Lan X., Talbot R.W., Laine P., Lefer B., Flynn J., Sun Z., and Torres A., Seasonal and diurnal variations of total gaseous mercury in urban Houston, Texas (U.S.A.). *Atmos.*, 5, 399–419, 2014.

Lefer B., Rappenglück B., Flynn J., and Haman C., Photochemical and meteorological relationships during the Texas-II Radical and Aerosol Measurement Project (TRAMP). *Atmos. Environ*., 44, 4005–4013, 2010.

Mao H., and Talbot R.W., Speciated mercury at marine, coastal, and inland sites in New England-Part 1: Temporal variability. *Atmos. Chem. Phys.*, 12, 5099–5112, 2012.

Mao H., Chen M., Hegarty J., Talbot R.W., Koermer J., Thompson A., Williams E., and Avery M.A., Comphrensive evaluation of seasonal simulations of ozone in the northeastern U.S. during summers of 2001–2005. *Atmos. Chem. Phys.*, 10, 9–27, 2010.

McGaughey G.R., Desal N.R., Allen, D.T., Seila R.L., Lonneman W.A., Fraser M.P., Harley R.A., Pollack A.K., Ivy J.M., and Price J.H., Analysis of motor vehicle emissions in a Houston tunnel during the Texas Air Quality Study 2000. *Atmos. Environ.,*. 38, 3363–3372, 2004.

Ngan F., and Byun D., Trajectory Analysis for Source-Receptor Relation of High Ozone Events over Houston/Galveston Area, Paper Presented at 9th Conference on Atmospheric Chemistry; *Am. Meteorol. Soc.*: San Antonio, TX, USA, 2007.

Noborio K., McInnes K.J., and Heilman J.L., Measurements of soil water content, heat capacity, and thermal conductivity with a single TDR probe. *Soil Sci.*, 161, 22–28, 1996.

Rappenglueck B., Perna R., Zhong S., and Morris G.A., An analysis of the vertical structure of the atmosphere and the upper-level meteorology and their impact on surface ozone levels in Houston, Texas. *J. Geophys. Res.*, 113, D17315, 2008.

Seinfeld J.H., and Pandis S.N., Atmospheric Chemistry and Physics: From Air Pollution to Climate Change, 2nd ed.; John Wiley: New York, NY, USA, 1998.

Streutker D.R., Satellite-measured growth of the urban heat island of Houston, Texas. *Remote Sens. Environ*., 85, 282–289, 2003.

Timmermann A., Oberhuber J., Bacher A., Esch M., Latif M., and Roeckner E., Increased El Niño frequency in a climate model forced by future greenhouse warming. *Nat.*, 398, 694–697, 1999.

Tzanis C., Tsivola E., Efstathiou M., and Varotsos C., Forest fires pollution impact on the solar UV irradiance at the ground. *Fresenius Environ. Bull.*, 18, 2151–2158, 2009.

Varotsos C., Ondov J., Tzanis C., Ozturk F., Nelson M., Ke H., and Christodoulakis J., An observational study of the atmospheric ultra-fine particle dynamics. *Atmos. Environ*., 59, 312–319, 2012.

Walker R.D., Connor T.H., MacDonald E.J., Trieff N.M., Legator M.S., MacKenzie K.W., and Dossins J.G., Correlation of mutagenic assessment of Houston air particulate extracts in relation to lung cancer mortality rates. *Environ. Res.*, 28, 303–312, 1982.

2.7. Supporting Materials

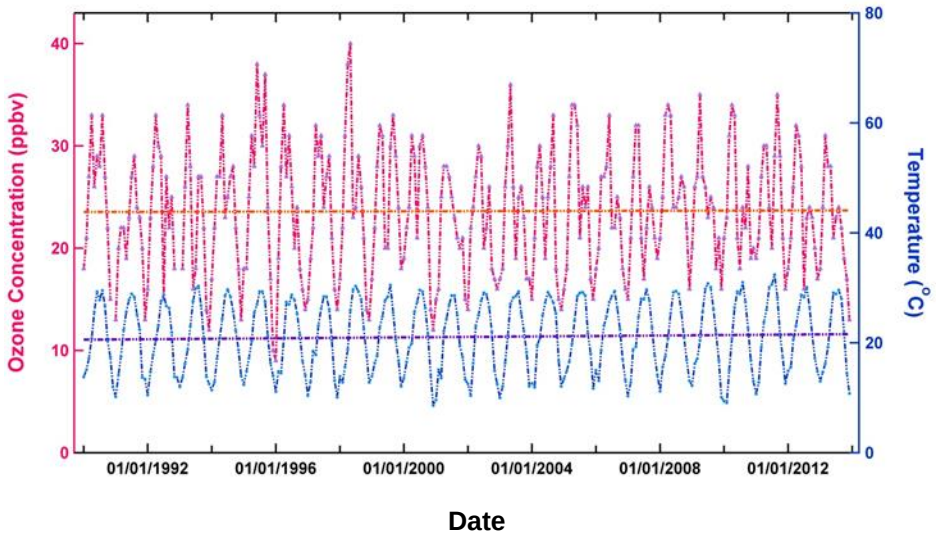

Figure S2.1. Monthly Averaged Ground-Level Ozone Mixing Ratio vs Temperature data at the Aldine site.

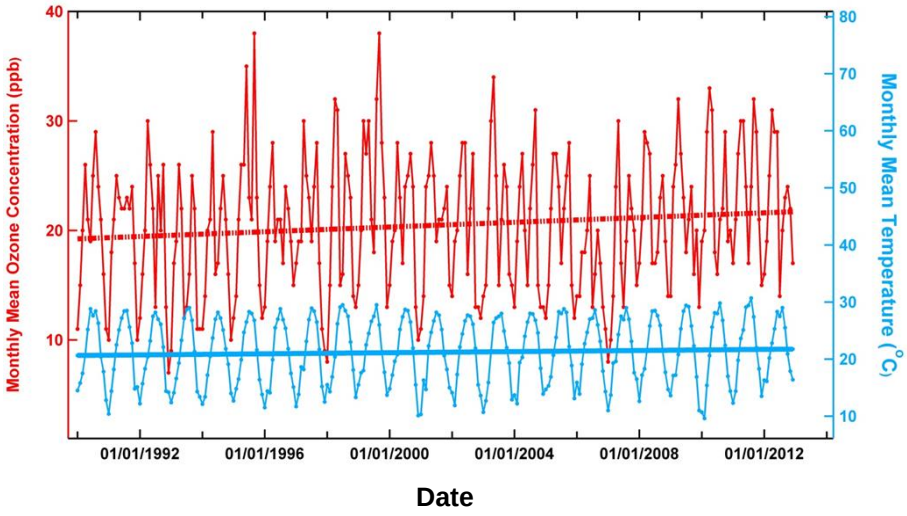

Figure S2.2. Monthly Averaged Ground-Level Ozone Mixing Ratio vs Temperature data in Clinton site.

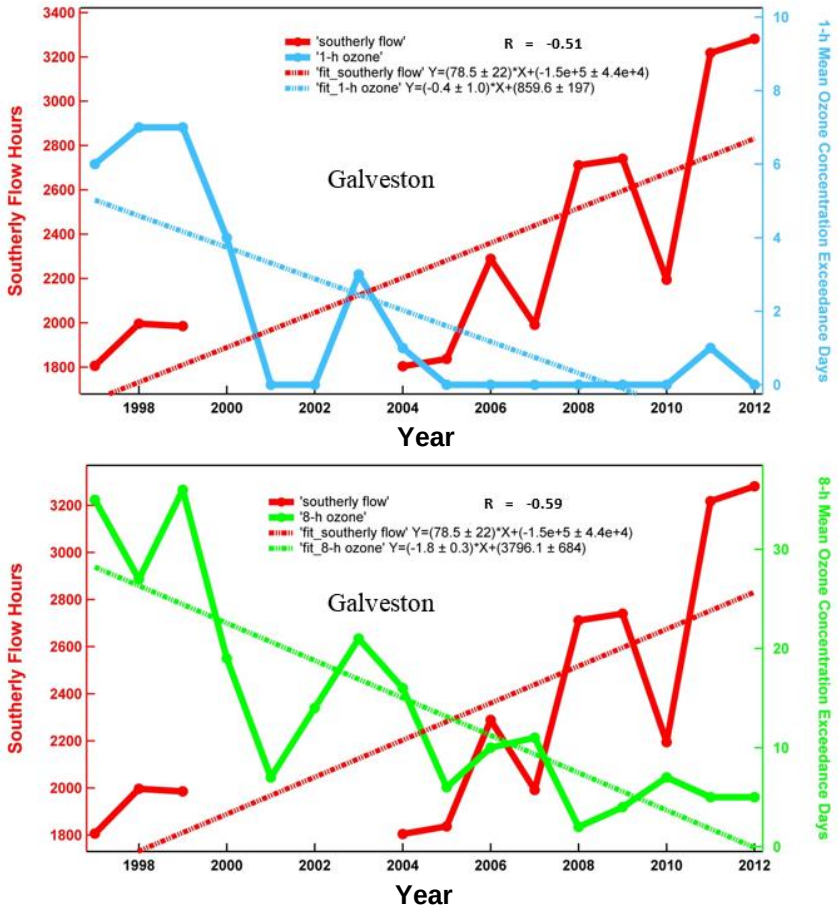

Figure S2.3. 1-hr and 8-hr exceedance days as a function of annual southerly flow hours per year at the Galveston site.

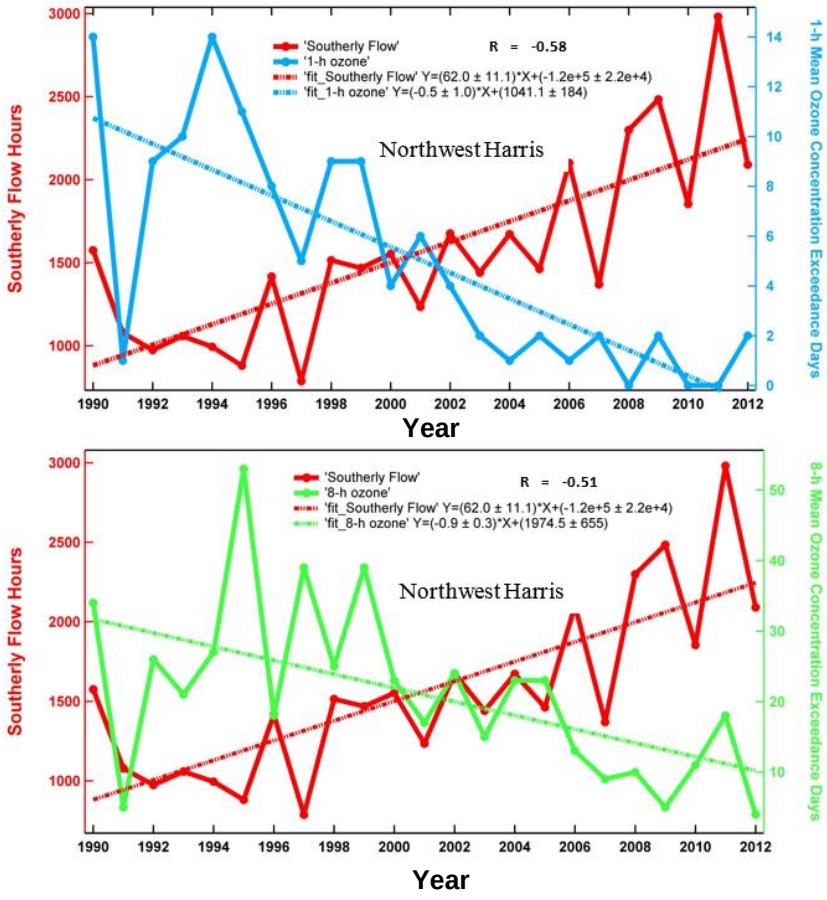

Figure S2.4. 1-hr and 8-hr exceedance days as a function of annual southerly flow hours per year at the Northwest Harris site.

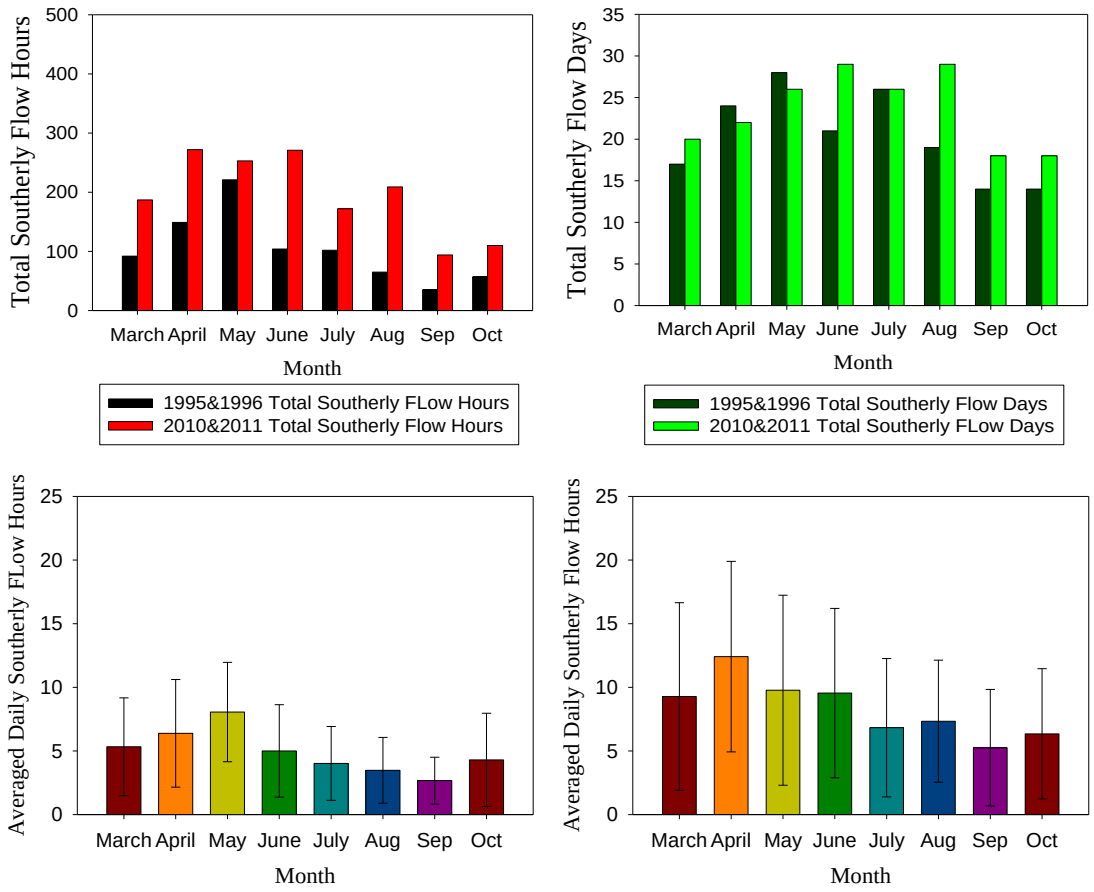

Figure S2.5. Days with southerly flow at the Northwest Harris site.

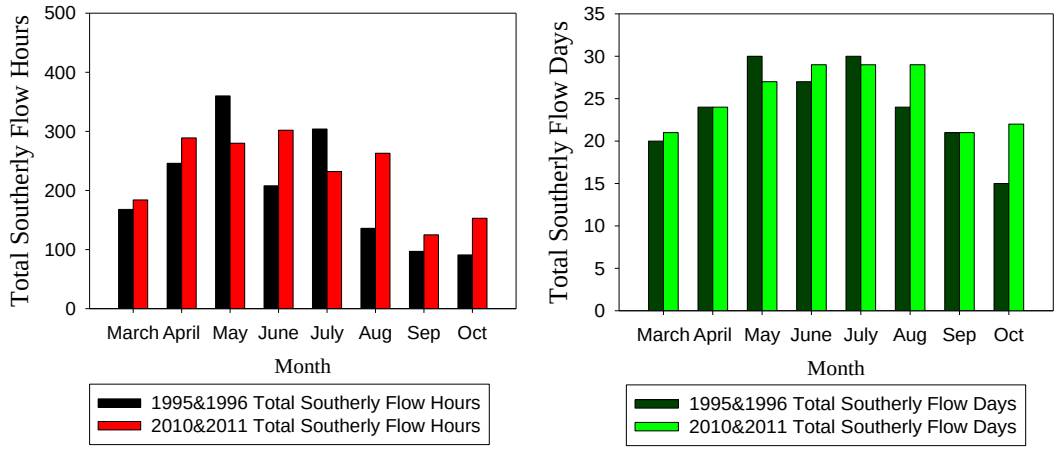

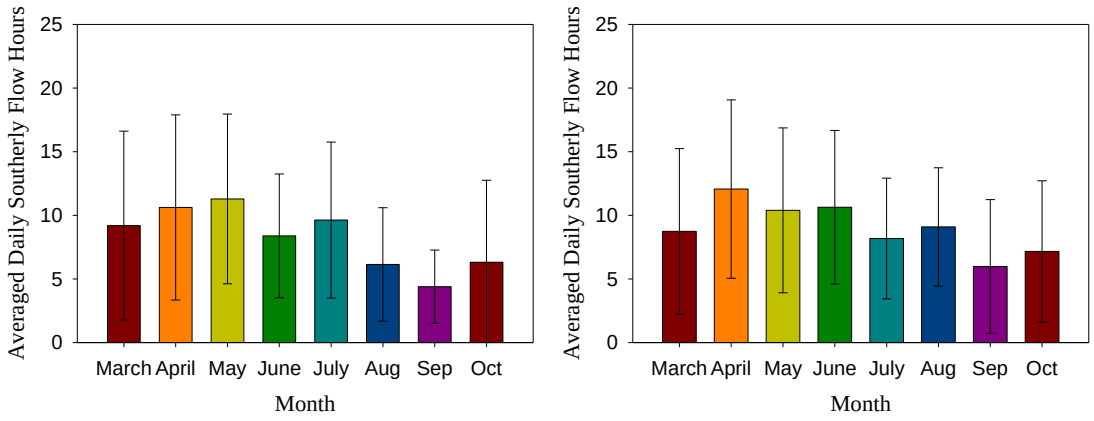

Figure S2.6. Days with southerly flow at the Clinton site.

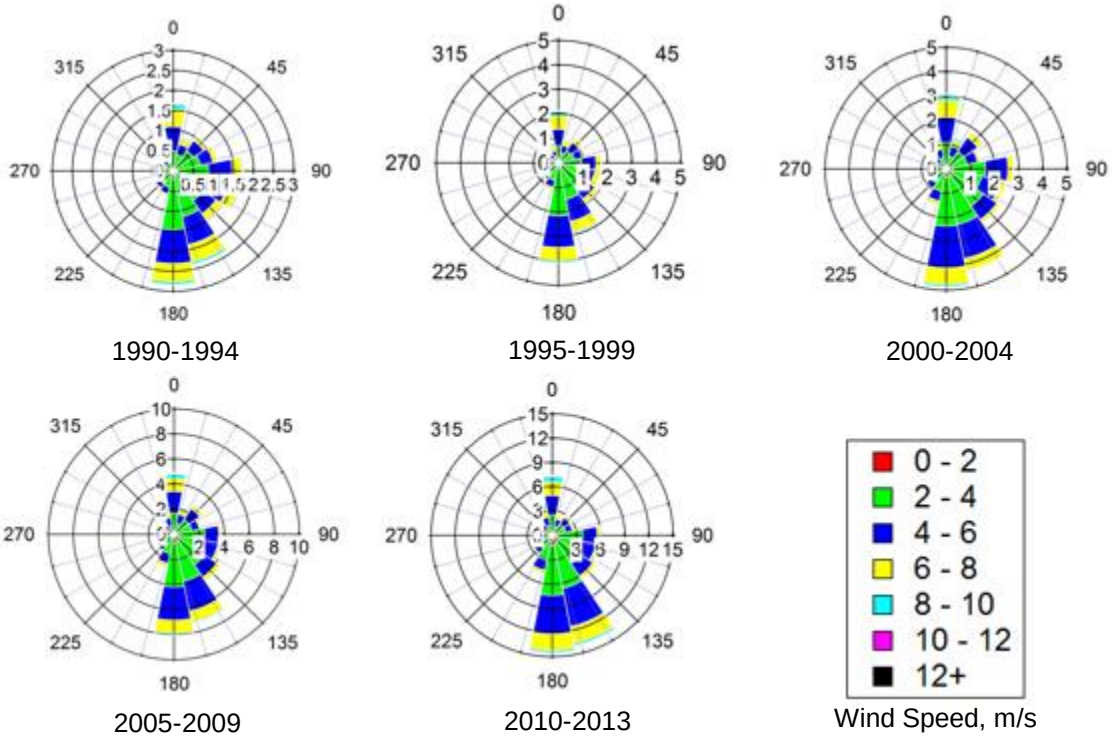

Figure S2.7. Wind speed and direction as a function of time in Clinton.

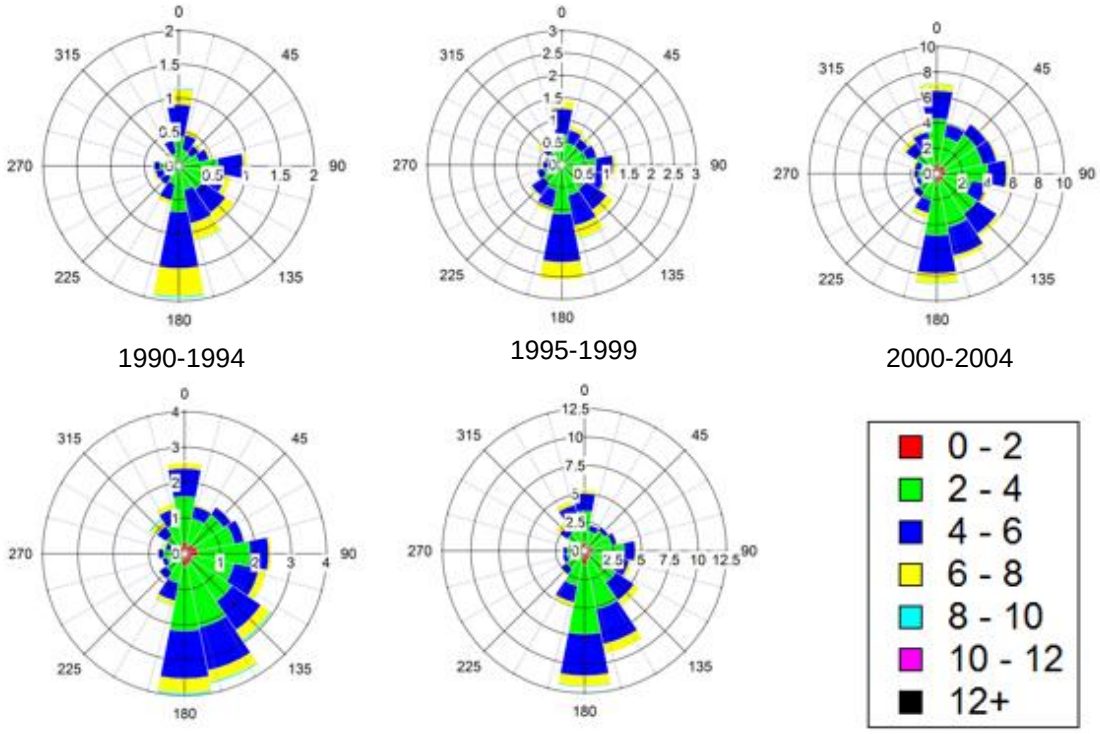

Figure S2.8. Wind speed and direction as a function of time in Northwest Harris.

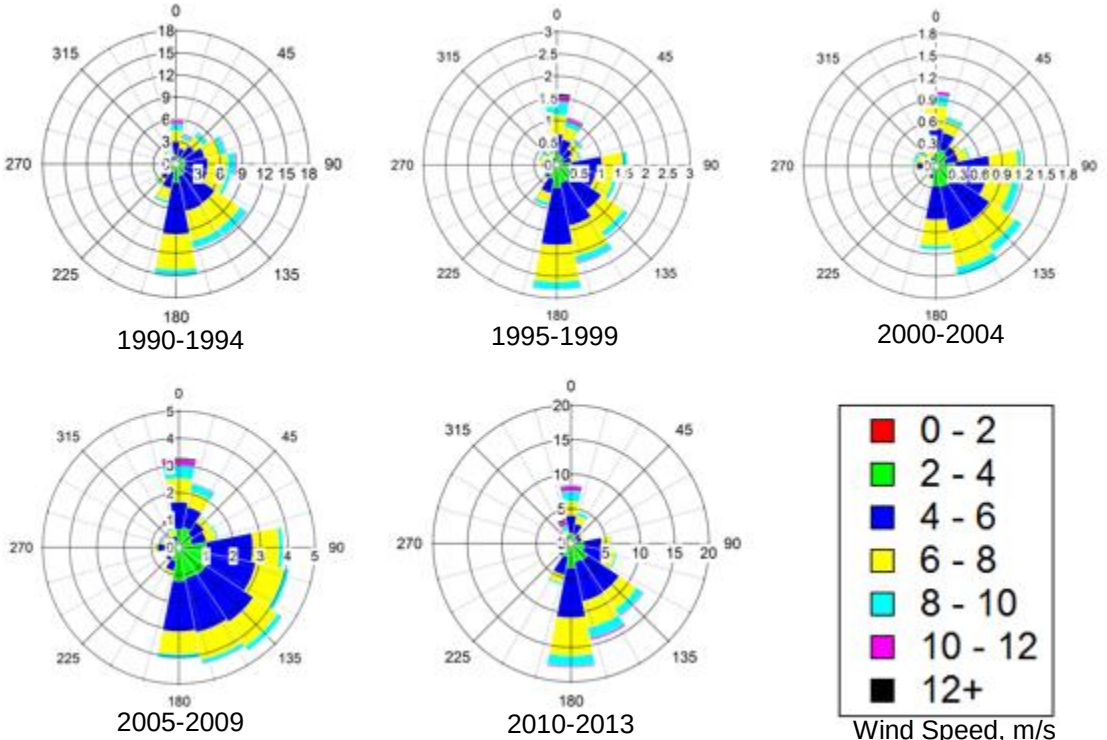

Figure S2.9. Wind speed and direction as a function of time in Galveston.

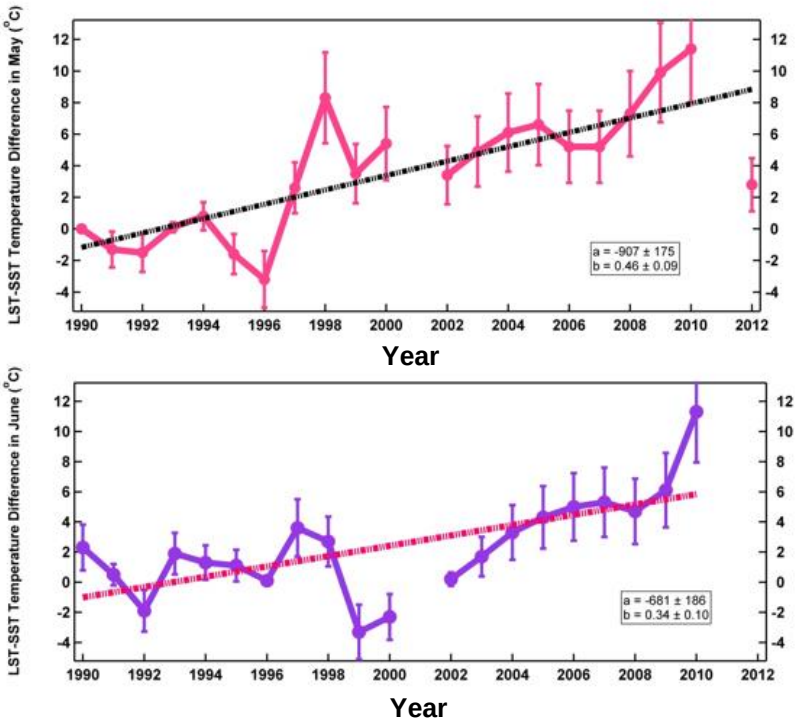

Figure S2.10. LST – SST Temperature Difference in May (top) and June (bottom).

Chapter 3

Comparison of Speciated Atmospheric Mercury at a Coastal and Urban Site[3]

3.1 Introduction

Mercury (Hg) is a pervasive and toxic environmental pollutant that exists in several chemical and physical forms that are distributed widely on Earth. The atmosphere serves as the major pathway for the release of mercury from reservoirs to the environment. Mercury is emitted to the atmosphere from a variety of anthropogenic sources (e.g., smelting, coal combustion, waste treatment, cement production), and natural sources (e.g., volcanoes, wild fires) (Pirrone et al., 2001; Sprovieri et al., 2010). Mercury in the atmosphere is then deposited to terrestrial systems or water bodies where it is converted to methylated mercury, the most toxic form of mercury that can enter the food chain by bioaccumulation (Pirrone et al., 1996). Thus, to analyze the characteristics of atmospheric mercury with special emphasis on its sources, transport and depositional mechanisms, is especially meaningful in areas where mercury emitting facilities are highly concentrated.

[3] Material in this chapter to be published:

Liu L., Talbot R., Torres A., Lefer B., Lan X., and Flynn J., Comparison of Speciated Atmospheric Mercury at a Coastal and Urban Site, pending submission, 2016.

Atmospheric mercury exists in three chemical forms, gaseous elemental mercury (GEM = Hg^o), reactive gaseous mercury (RGM = $HgCl_2$+$HgBr_2$+$HgOB_r$+…) and particular bound mercury (PBM = Hg^p) (Zhu et al., 2012). The chemical composition of RGM has recently been challenged (Jaffe et al., 2014), producing greater uncertainty in understanding atmospheric mercury. The lifetime of GEM in the atmosphere is 6–12 months, that of PBM in the lower troposphere is 2–5 days (Keeler et al., 1995), while the lifetime of RGM is even shorter, only 1–3 hours (Skov et al., 2006). RGM and PBM are removed rapidly from the atmosphere due to their water solubility and high rates of dry deposition (Schroeder and Munthe, 1998; Skov et al., 2006; Keeler et al., 1995). GEM reportedly comprises > 95% of the global atmospheric mercury pool (Gabriel et al., 2005*)*, and GEM can be oxidized to RGM under the presence of hydroxyl radicals, halogen atoms, and nitrate radicals (Laurier et al., 2003; Holmes et al., 2006; Nair et al., 2011). RGM can also be converted to PBM under special conditions. New research may lead to refinements in these chemical transformations.

Valente et al., (2007) found that the Northern Hemisphere GEM background level is 168 ppqv, RGM mean mixing ratio is 3-5 ppqv, and PBM ranges between 3 and 35 ppqv. However, local mercury sources, meteorology, and topography patterns impact mercury cycling in the atmosphere as demonstrated in previous multiple-sites studies (Lan et al., 2014; Cheng et al., 2014; Gabriel et al., 2005; Rutter et al., 2007; Mao and Talbot, 2012). A recent study reported mercury species diurnal patterns in rural sites across the United States Atmospheric Mercury Network: the maximum mixing ratio took place around solar noon and the minimum shown up just before sunrise (Lan et al., 2012). Mao and Talbot (2012) found this cycle is driven by re-volatilization following

deposition. Meanwhile, studies in urban areas of United States found higher mixing ratios of GEM, RGM and more complex diurnal patterns (Gabriel et al., 2005; Nair et al., 2011), which were probably impacted by local anthropogenic emissions, boundary layer dynamics, dry/wet deposition, and photochemical reactions (Engle et al., 2010; Nair et al., 2011). On the other hand, the ocean is a significant source of GEM, reactive bromine, sea salt, and halogen radicals, which can oxidize GEM to RGM and PBM (Malcolm et al., 2003, Cheng et al., 2014). Thus, it is significant to research the impacts of marine air on atmospheric mercury cycling in coastal environments and contrast it with the mercury measurements at an urban site.

Understanding the atmospheric mercury budget in Houston is challenging. There are distinct industrial emissions, a special geographic pattern (close to the Gulf of Mexico), and complex meteorological conditions (Liu et al., 2015; Banta et al., 2005; Brooks et al., 2010). Data from the National Atmospheric Deposition Program indicates that mercury concentrations in precipitation in the Gulf of Mexico area are the highest in the United States (Ren et al., 2014). A few atmospheric mercury measurements were conducted in Houston (Brooks et al., 2010; Lan et al., 2014), atop the University of Houston MT. However, the previous research was limited to a single urban site. This study focuses on the comprehensive analysis of atmospheric mercury, investigating, and comparing the factors that impacted mercury mixing ratios under urban and coastal settings in the Houston area. Our data contains continuous 16-months of mercury measurements together with simultaneous meteorological parameters and key trace gases data. The aims of the study were to improve the understanding of mercury pollution under different environmental settings, to investigate high mercury events, and to help

evaluate the regional mercury budget in the Houston area.

3.2 Methodology

3.2.1 Sampling Area

According to 2011 United States EPA National Emissions Inventory (NEI), southeastern Texas and Louisiana encompasses an area with one of the highest mercury emissions from oil and gas facilities, power plants, and waste management facilities in the United States. As Figure 3.1 shows, the Freestone Electric Station and Limestone Generation Station, which locate north of Houston, emit 1200 kg mercury per year. The WA Parish plant, one of the largest coal-fired electrical power plants in the United States, locate 60 km southwest of downtown Houston, emits 250 kg mercury per year. In summarize, nearly half of Texas mercury emitting facilities are accumulated in the Houston-Galveston area and an even larger number if you include the surrounding counties, making Houston an ideal location for mercury measurements and investigations of its cycling.

As shown in Figure 3.2, the continuous observations of GEM, RGM, and PBM were conducted at two observatory sites: atop the University of Houston Moody Tower (29.71^{o}N, 95.34^{o}W) from March 22, 2012 to June 6, 2013 and at the University of Houston Coastal Center (29.23°N, 95.15°W) from July 26, 2012 to June 6, 2013. The MT building is an urban site located inside the inner loop of the city. The 70 m height of this site is unique because it makes it less sensitive to local activities. The MT site locates 2-4 km away from major freeways, 35 km west of Galveston Bay, 70 km northwest of the Gulf of Mexico, and 25 km west-southwest of the Houston Ship-Channel area, where approximately more than 400 chemical manufacturing facilities and two of the four

largest refineries in the U.S. reside (Lan et al., 2014). The CC is a ground level coastal site locates in central Galveston County, approximately 22 km northwest of the Gulf of Mexico, 53 km southeast of the MT site, west of the Texas City industrial refinery area, and south of the Houston Ship-Channel area. Both sites are downwind from large emission sources, making them ideal for air quality studies.

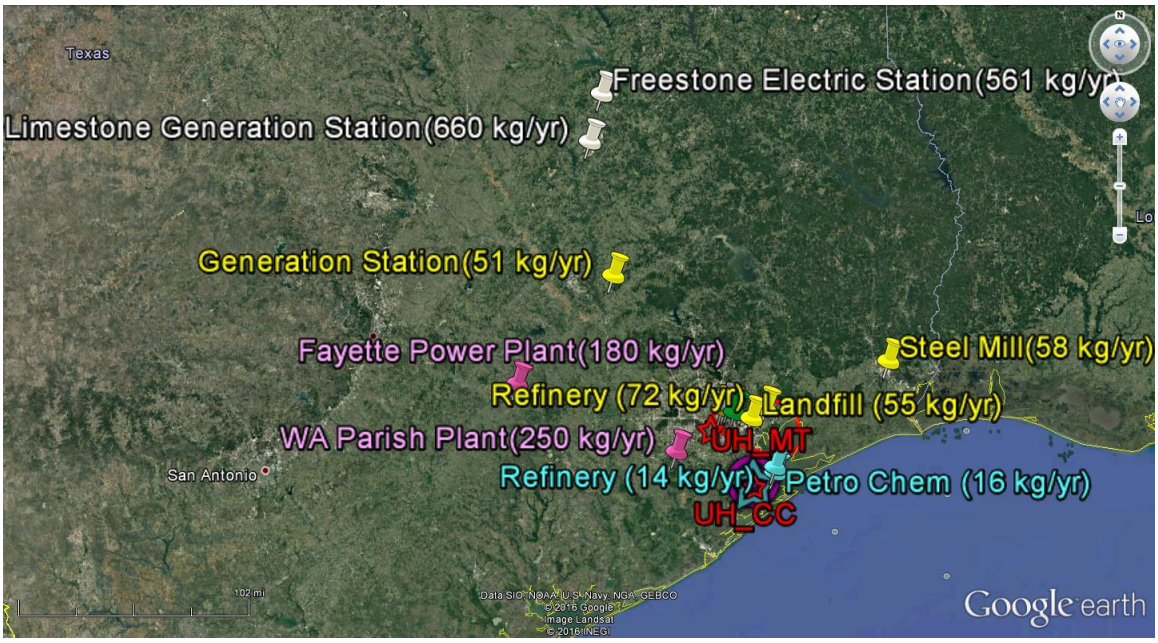

Figure 3.1. Facility emission sources around Houston from 2011 NEI mercury facility data.

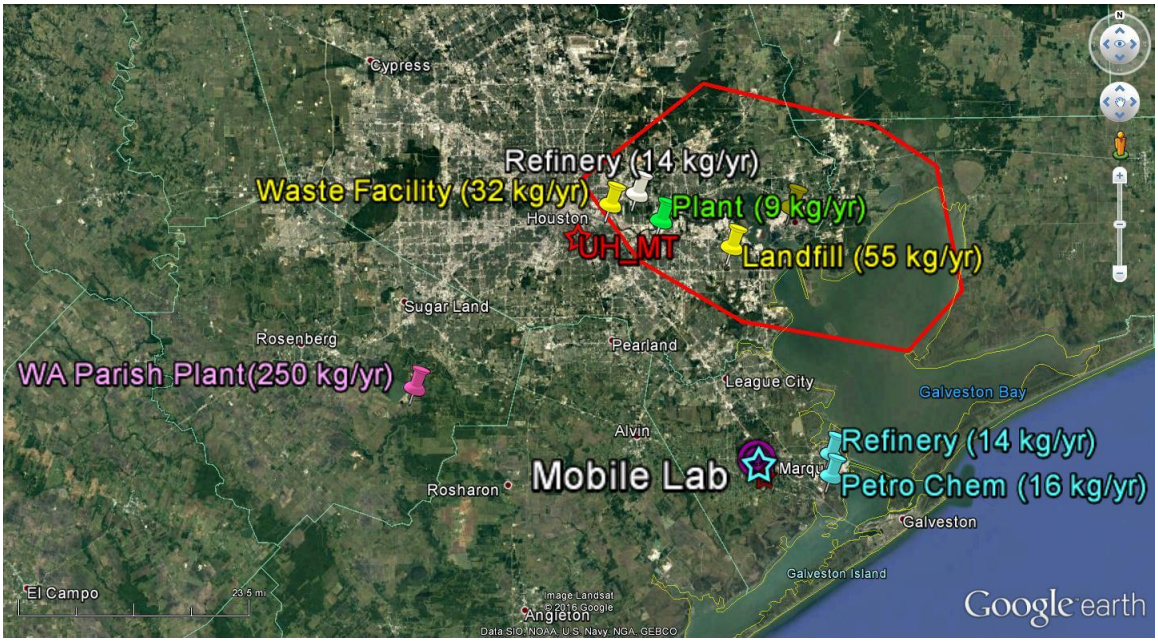

Figure 3.2. Locations of the UH Moody Tower and Coastal Center monitoring station, along with large point sources of mercury in the Houston region, based on the US EPA 2011 national Emission Inventory. Red polygon is the Houston Ship-Channel area.

3.2.2 Measurements

Mercury measurements at MT and CC sites were conducted on a continuous 24 hr/day 7 day/week basis with 5-min time resolution of GEM and 2-hr time resolution of RGM and PBM. A Tekran 2537A-1130-1135 Atmospheric Mercury Speciation System was utilized at both air-monitoring facilities. This system is a combination of three separate units. Model 2537A is a mercury vapor analyzer, which can be used on its own to provide total gaseous mercury (TGM = GEM + RGM), however when in use as part of the speciation system it provides mixing ratios of GEM. The model 1130 Mercury Speciation Unit measures RGM mixing ratios and Model 1135 Particulate Mercury Unit provides PBM mixing ratios.

The Model 2537A employs a Cold Vapor Atomic Fluorescence

Spectrophotometry (CVSFS) for GEM detection with a detection limit of <0.1 ng/m^3 and a range of 0.1-2000 ng/m^3. Model 1130 Mercury Speciation Unit has an active sampling element of a potassium chloride coated thermally on a re-generable quartz denuder. The denuder captures RGM while allowing GEM to pass through freely. When the sampling phase is complete, the denuder is desorbed by heating it. Upon its release from the denuder surface, the 2537A quantitates the RGM released. The particulate mercury unit, Model 1135, provides mixing ratios of PBM for particulate matter (PM) <2.5 μm. The fine particles are then trapped on a quartz particulate filter, and released with each desorption cycle. As this particulate trap is heated to 900 ºC, the PBM is desorbed allowing the 2537A Model to quantitate the GEM released.

The Tekran system employed an internal permeation tube calibration (±5% reproducibility) that was verified every six months using syringe injection from the headspace of a thermoelectrically cooled GEM reservoir (Tekran model 2505). Standard additions of GEM were conducted using the internal permeation source in the Tekran. The Tekran 2537A-1130-1135 Atmospheric Mercury Speciation System outputs ng/m^3 (10^{-9} g/m^3) for GEM and pg/m^3 (10^{-12} g/m^3) for RGM and PBM that are converted to atmospheric mixing ratios in parts per quadrillion by volume (ppqv) (1 ng/m^3 = 112 ppqv and 1 pg/m^3 = 0.112 ppqv).

In contrast to others (*i.e.*, Lyman et al., 2010), we did not observed apparent loss of GEM with enhanced O_3 levels of up to ~150 ppbv (Figure S3.1; S3.2). This gives us confidence that our results are meaningful and useful for analysis without apparent artifacts.

Continuous measurements of key trace gases (CO, CO_2, O_3, CH_4, NO_x, and SO_2) and

meteorological parameters were conducted, making it possible to better identify mercury plume signatures from various sources in Houston-Galveston area. Meteorological parameters (time resolution = 5 min) measured at MT included temperature, relative humidity, pressure, precipitation, planetary boundary layer height, wind speed, and direction. At CC, temperature, relative humidity, pressure, precipitation, wind speed, and direction were monitored. Carbon monoxide and ozone mixing ratios were measured at both sites by the Thermo CO analyzer and the Thermo Ozone UV photometric analyzer with 5-min resolution. At the MT site, SO_2 was measured during August 19, 2012~June 6, 2013 with a Thermo 43C instrument. Nitric oxide and nitrogen dioxide were measured by TE NO-NO_2-NOx analyzer during March 22, 2012~November 15, 2012. The time resolution of SO_2, NO, NO_2, and NO_x were averaged to 5-min. A LICOR LI-7000 analyzer were employed to measure carbon dioxide during March 22, 2012~October 21, 2012. The Picarro G2132-i instrument measured CH_4 mixing ratios during June 4, 2012~January 1, 2013. Both instruments calibration were checked monthly with Scott Marrin ±1% NIST certified standards.

3.3 Results

3.3.1 General Characteristics

The complete time series of GEM, RGM, and PBM at the MT and CC sites are presented in Figure 3.3. The distributions of GEM, RGM, and PBM at both sites were characterized by significant variabilities throughout the sampling period. At MT, the GEM mean mixing ratio was 185 ppqv (GEM median value = 178 ppqv) (Table 3.1), which was 17 ppqv higher than the Northern Hemisphere background level of 168 ppqv (Valente et al., 2007). RGM mean value was 0.72 ppqv (RGM median value = 0.39 ppqv)

and PBM mean value equaled 0.71 ppqv (PBM median value = 0.38 ppqv). RGM and PBM mean mixing ratios were 6 times higher than the NH background level (0.112 ppqv). At the CC, the GEM mean value was 165 ppqv (GEM median value = 163 ppqv) (Table 3.1), lower than the GEM NH background level and higher than those measured at other coastal sites located in the northern United States (*e.g.*, 139 ppqv, Sigler et al., 2009). The mean value of RGM was 0.75 ppqv (RGM median value = 0.23 ppqv), PBM mean mixing ratio was 0.58 ppqv (PBM median value = 0.24 ppqv). Both RGM and PBM mean mixing ratios measured at the CC were higher than the NH background levels by a factor of 4. According to Lan et al., 2012, GEM mixing ratios ranged between 148 and 226 ppqv at 11 different United States Atmospheric Mercury Network (AMNet) sites, the GEM mean values measured in Houston belong to this range, but GEM mixing ratios measured at MT are higher than those monitored at the CC. An impressive feature of the mercury measured at both sites is the frequent occurrence of large mercury events, especially at MT.

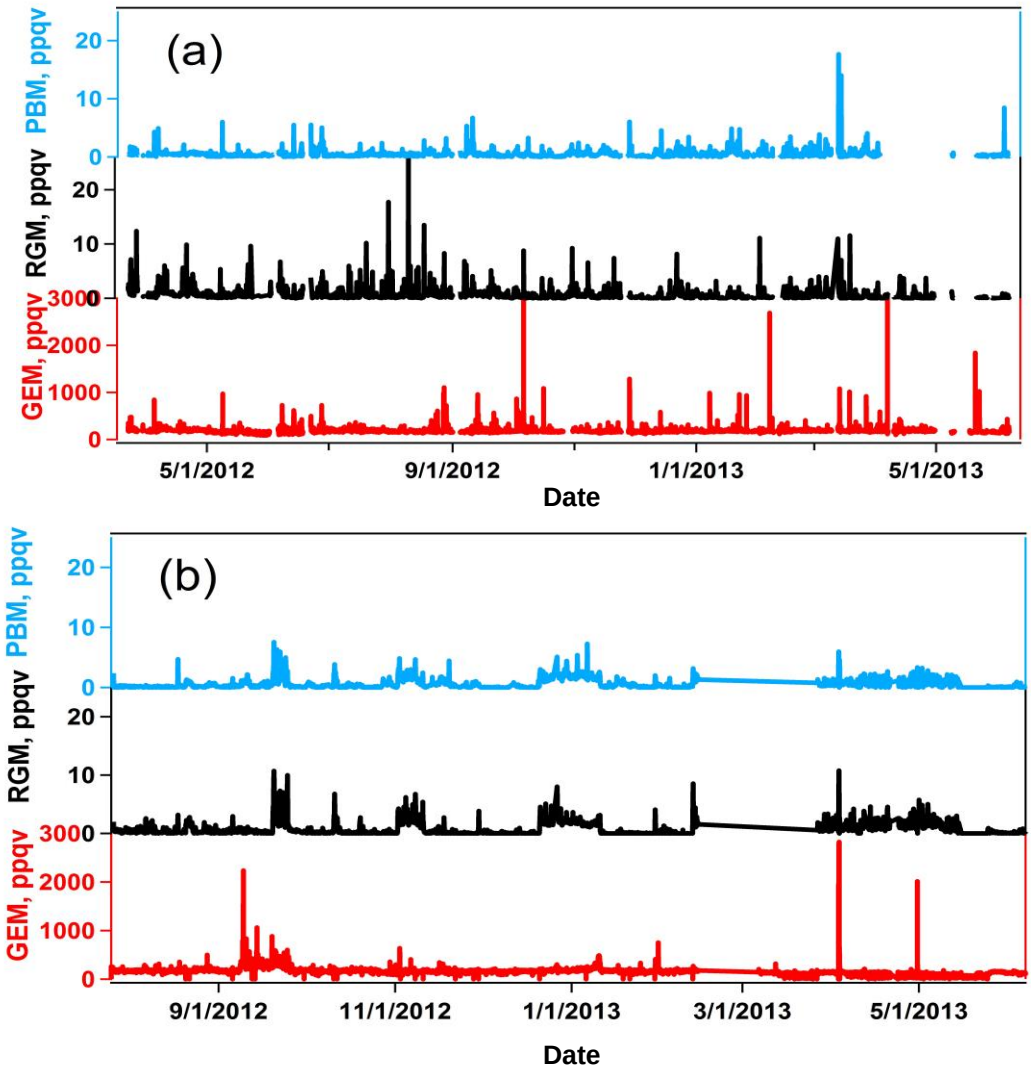

Figure 3.3. The complete time series of GEM, RGM, and PBM at the MT (a) and CC (b) sites.

Figure 3.4a depicts the frequency of TGM mixing-ratio intervals at MT, 7.3% were in the range between 80 and 150 ppqv, which represents the TGM mixing ratios below the NH background level. Most of the TGM mixing ratios (75.4%) were distributed between 150 and 200 ppqv, close to the NH background level, 16% exceeded 200 ppqv. At CC (Figure 3.4b), 6.7% of the TGM mixing ratios were under 80 ppqv, 30% were distributed in the range of 80 ~ 150 ppqv. A large portion of the TGM (51.4%) was

distributed in the range of 150 ~ 200 ppqv, only 8% of the TGM mixing ratios exceeded 200 ppqv. In summary, the CC site exhibited a higher occurrence of low mercury events and MT site showed a higher frequency of high mercury events.

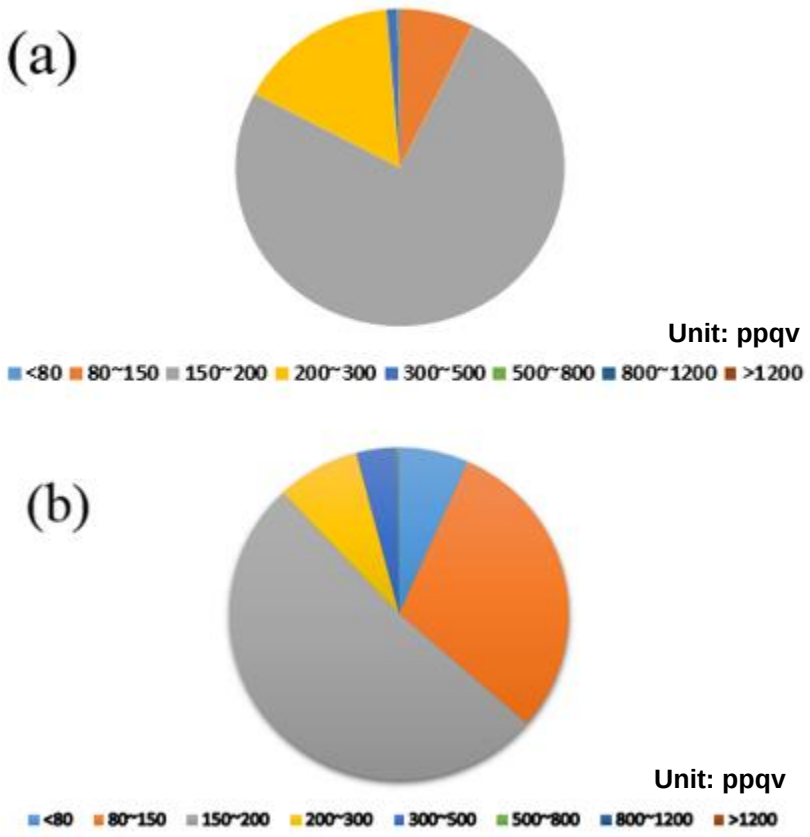

Figure 3.4. Total gaseous mercury mixing-ratio intervals at MT (a) and CC (b) sites.

3.3.2 Seasonal and Monthly Variations

GEM, RGM, and PBM measured at MT and CC showed distinct monthly and seasonal variations during the study period. Figure 3.5 depicts the variations of the monthly median GEM (Figure 3.5a), RGM and PBM (Figure 3.5b). As Figure 3.5a shows, monthly median GEM at MT oscillated around 178 ppqv. In March and April 2012, the median values were as high as 200 ppqv decreased to 150 ppqv in May, then

increased again to 180 ppqv in the following months.

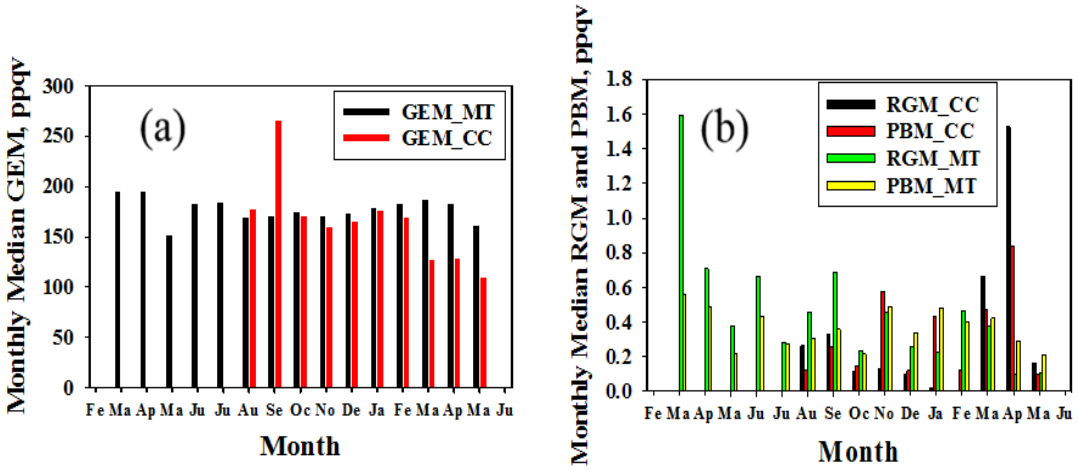

Figure 3.5. Monthly medians of GEM, RGM, and PBM at MT and CC sites.

At the CC, except the extremely high GEM value (260 ppqv) that occurred in September 2012, the other months' GEM median values were lower than those measured at MT, especially in March, April, and May in 2013. The GEM median values measured at the CC oscillated around 162 ppqv. In Figure 3.5b, RGM, and PBM monthly median values experienced dramatic oscillations at both sites. For RGM at MT, the highest monthly median value was 1.6 ppqv in March 2012, it was more than a double of the mean RGM (0.72 ppqv) at the same site. RGM median value decreased to 0.63 ppqv in April 2012 and showed a decreasing trend along the following months with slight variations. For monthly median RGM at the CC, it varied around 0.5 ppqv, lower than that measured at the MT site, except in March 2012 and April 2013, when RGM was as high as 1.58 ppqv, two times higher than the other months. We suspect that is due to the more active photochemical reaction from GEM to RGM in spring season under the presence of abundant marine halogen compounds under the coastal environment, mercury

probably would be rapidly cycled (Malcolm et al., 2003; Sigler et al., 2009; Lan et al., 2012; Obrist et al., 2011). The monthly median PBM mixing ratio at MT ranged between 0.2 ppqv and 0.6 ppqv throughout the sampling period, and ranged between 0.1 ppqv and 0.8 ppqv at CC. The PBM oscillation at the CC was more dramatic than that at MT and the average monthly median PBM value was 0.25 ppqv lower than that at MT, it was likely due to the impact from local Hg emission sources considering the short lifetime of PBM.

Table 3.1 depicts the seasonal characteristics of GEM, RGM, and PBM at the MT and CC sites. The GEM mixing ratio at MT ranges between 81 ppqv and 27,326 ppqv, the mean mixing ratio was 184 ppqv, median value was 178 ppqv, which exceeded the Northern Hemisphere background level. Over the five seasons GEM mixing ratio values showed small differences. At the CC site, GEM mixing ratios show distinct variations between each season. The highest GEM mean value (198 ppqv) occurred in 2012 fall, and the lowest mean value (114 ppqv) was seen in 2013 spring. For RGM and PBM: the low RGM value (0.29 ppqv/0.03 ppqv) occurred in winter (2012) at both sites which is probably because of the lower photochemical reaction rate from GEM to RGM. On the other hand, the mean/median RGM value was extremely high (1.09 ppqv/0.89 ppqv) in 2013 spring at the CC, which was two times higher than the average, meanwhile, the mean/median GEM value (113 ppqv/124 ppqv) measured at the same site in the same season is 30% lower than the average values. A more detailed analysis is available in the Discussion section. The 2012 summer met with the lowest median/mean PBM mixing ratios for both sites, however, relatively higher PBM values occurred in winter and spring. We attribute this phenomenon to the higher southerly flow wind speed together with

more active agricultural biomass burning activities from Mexico and Central America in the winter and early spring seasons (Ren et al., 2014). To summarize, the seasonal median values of RGM and PBM measured at MT is higher than those measured at CC, this phenomenon highly reflects that RGM and PBM are easily affected by the local mercury emissions due to their short lifetime (Obrist et al., 2011).

Table 3.1. Statistical summary of GEM, RGM, and PBM measurements at the MT and CC sites

	Moody Tower				Coastal Center			
	Mean±Std	Median	Range	N	Mean±Std	Median	Range	N
GEM (ppqv)								
2012 spring	182±17	180	81~973	7796	*	*	*	*
2012 summer	189±15	179	94~1105	11483	179±36	176	11~498	5137
2012 fall	183±26	172	113~27326	10690	197±29	173	11~2236	12559
2012 winter	182±18	179	112~2689	11405	174±24	170	12~754	10164
2013 spring	184±23	180	96~4631	10348	113±19	124	12~2823	11297
Total	184±30	178	81~27326	51723	164±34	162	11~2823	39160
RGM (ppqv)								
2012 spring	1.09±0.5	0.64	0.10~12.39	590	*	*	*	*
2012 summer	0.88±0.3	0.42	0.18~26.04	874	0.46±0.4	0.26	0.15~3.15	407
2012 fall	0.66±0.1	0.47	0.21~9.23	944	0.69±1.1	0.18	0.1~10.71	1042
2012 winter	0.51±1.6	0.29	0.19~11.11	811	0.66±0.7	0.03	0.1~8.52	842
2013 spring	0.48±1.2	0.17	0.14~11.57	756	1.09±2.1	0.89	0.1~10.76	790
Total	0.72±0.9	0.39	0.10~26.04	3856	0.75±0.3	0.23	0.1~10.76	3082
PBM (ppqv)								
2012 spring	0.47±1.9	0.41	0.18~6.01	661	*	*	*	*
2012 summer	0.45±1.3	0.29	0.11~5.53	880	0.19±0.2	0.12	0.12~4.69	407
2012 fall	0.47±1.6	0.36	0.15~6.73	955	0.59±0.9	0.26	0.14~7.55	1042
2012 winter	0.57±0.8	0.41	0.21~4.86	836	0.67±1.1	0.21	0.11~7.27	842
2013 spring	0.57±1.0	0.31	0.17~17.65	523	0.67±0.8	0.55	0.16~5.96	790
Total	0.71±0.1	0.38	0.10~17.65	3976	0.58±1.6	0.24	0.10~7.55	3082

3.3.3 Diurnal Patterns

Mercury mixing ratios measured at MT and CC exhibited pronounced diurnal patterns as seen in Figure 3.6. At MT (Figure 3.6a), GEM started to increase from midnight (06:00 UTC time) and accumulated overnight, the maximum GEM value, which was as high as 220 ppqv, shown up right before the sunrise (12:00 UTC time). It was then followed by a sharp decrease after sunrise (14:00 UTC time) and a more gradual decrease in the following hours. The daily minimum mixing ratio occurred in the late

afternoon which was as low as 176 ppqv. Similar urban diurnal patterns shown up in other urban cities which were demonstrated by previous studies: Detroit, United States (Liu et al., 2007), Nanjing, China (Zhu et al., 2012) and Chongqing, China (Yang et al., 2009). The mechanism of the typical urban GEM diurnal pattern is highly related with the lower nocturnal boundary height and stagnant condition in the Houston urban area (Banta et al., 2005; Liu et al., 2015). Mercury emissions emitted from anthropogenic activities thus accumulated and reached maximum values before the sunrise until the stable condition was broken by the morning increase in vertical turbulent motions. The RGM diurnal pattern at MT showed distinct variations as well, it started to increase at noon (17:00 UTC time) and reached its maximum value (3.0 ppqv) in the late afternoon (00:00 UTC time), then followed by a decrease at nighttime and the diurnal minimum (0.3 ppqv) in the morning. Due to the short lifetime of RGM, the increase of RGM in the afternoon is well related with the increase of temperature and solar radiation which contributes to the intensifying photochemical activity, meanwhile the lower RGM at night was probably due to deposition mechanisms (Nair et al., 2011).

As shown in Figure 3.6b, the CC site had diurnal mercury patterns that showed obvious differences with the urban area. For example, GEM exhibited a steady decrease at night and reached its minimum mixing ratio (140 ppqv) before the sunrise (11:00 UTC time), then it slowly increased after the sunrise and reached its maximum (175 ppqv) in the late morning (16:00 UTC time). This pattern is typical for rural areas and has been summarized previously (Lan et al., 2012; Ren et al., 2014; Nair et al., 2011; Zhu et al., 2012; Mao et al., 2012). The RGM and PBM diurnal patterns showed small variations and the RGM level overall was higher than in the urban environment.

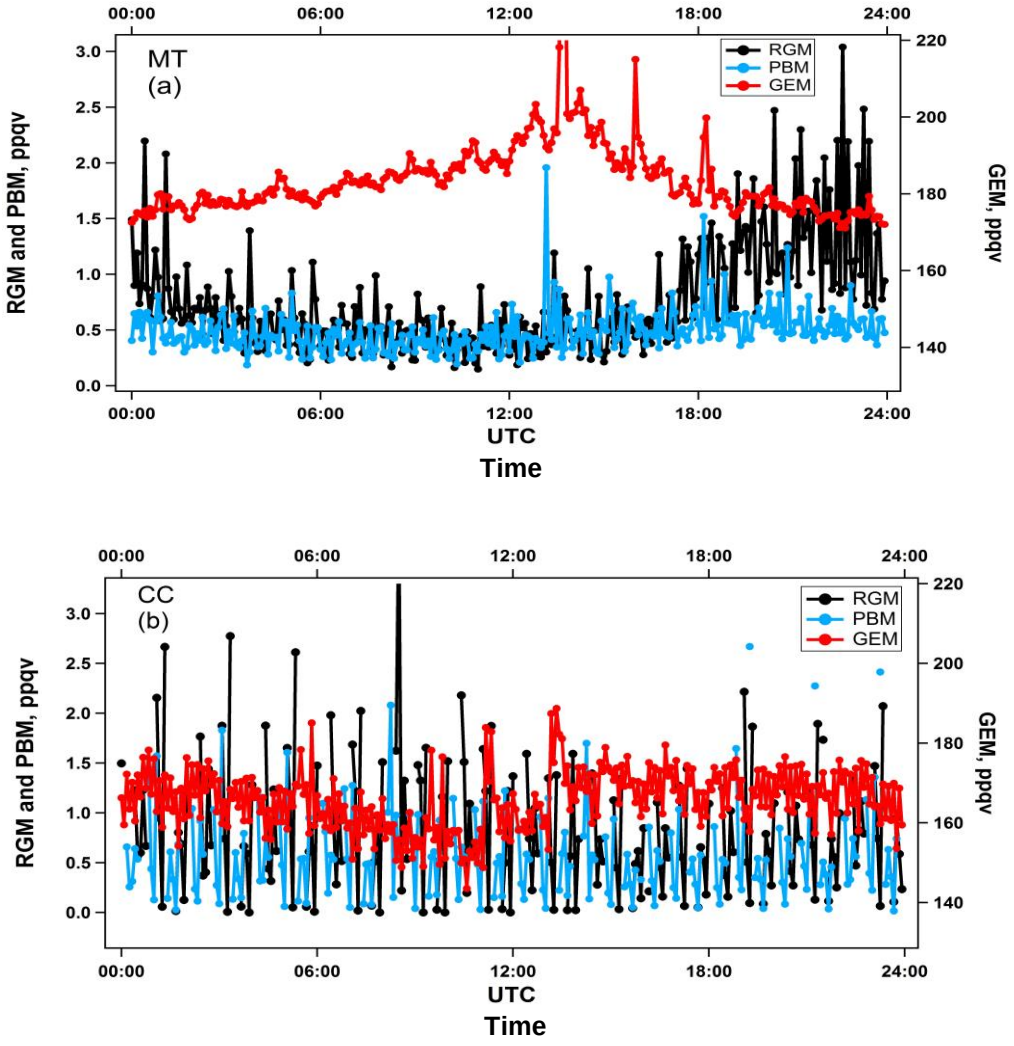

Figure 3.6. Diurnal variations of GEM, RGM, and PBM at the MT (a) and CC (b) sites.

3.3.4 Seasonal Patterns

In 2012 spring, 2012 summer, 2012 fall, 2012 winter, and 2013 spring, the MT site GEM seasonal diurnal variation (Figure 3.7a) showed gradually increasing trend starting around midnight (06:00 UTC time) and lasting 6-8 to reach the maximum values right before sunrise, then followed by the gradual decrease after the sunrise and reached the minimum mixing ratio at early nighttime (00:00-03:00 UTC time). The average amplitude of the five seasons diurnal cycle was ~50 ppqv (180 ppqv - 230 ppqv). The

largest amplitude occurred in 2012 fall, which is probably because the highest GEM mixing ratio occurred in October 2012. We noticed that the GEM diurnal peak occurred at 06:30 local time in the summer season, earlier than the other three seasons (fall: 08:00 local time; winter: 11:00 local time; spring: 09:30 local time). This is correlated with the time when significant PBL height increase commenced.

The CC site GEM seasonal diurnal variation (Figure 3.7b) in 2012 summer, 2012 fall, 2012 winter, and 2013 spring showed a large difference compared to MT. The average amplitude of the four seasons was 40 ppqv (160 ppqv - 200 ppqv for summer, fall, winter; 100 ppqv - 140 ppqv for 2013 spring), lower and smoother than those measured at MT. This diurnal pattern is typical when compared with other rural areas. An interesting point is the special diurnal pattern was in 2013 spring, the GEM mixing ratio was 40% lower than the other three seasons and the diurnal peak time took place before sunrise. After analyzing the wind pattern in spring 2013, we found the frequency of southerly flow was intensified by 25%, which likely diluted the GEM mixing ratios at the CC site and inhibited inflow of polluted urban air.

The seasonal diurnal variation patterns of RGM at MT (Figure 3.7c) started to increase significantly in the late morning and reached maximum values in the afternoon around 15:00 local time, then gradually decreased from the late afternoon until the midnight (03:00 local time). The largest amplitude occurred in summer (0.5 ppqv~2.4 ppqv), followed by spring (0.4 ppqv~1.4 ppqv), fall (0.4 ppqv~1.2 ppqv) and winter (0.2 ppqv~0.6 ppqv). The peak mixing ratio values ordered as summer (2.7 ppqv), spring (1.4 ppqv), fall (1.0 ppqv), and winter (0.7 ppqv). This emphasis the important roles of temperature and solar radiation in RGM cycling (*i.e.*, photochemistry and re-volatilize

mechanisms). The seasonal diurnal pattern of PBM at MT site (Figure 3.7e) did not show significant variations, the average amplitude was 0.2 ppqv (0.4 ppqv ~0.6 ppqv) with small standard deviations. In general, the amplitudes of PBM are smaller than those of RGM. This is similar to the other sites (AMNet) (Lan et al., 2012) distributed across the United States.

The CC RGM seasonal diurnal variation patterns (Figure 3.7d) showed differences compared with those at MT. RGM in summer, fall and winter increased significantly in the early morning hours and reached their maximum values in the afternoon around local time 15:00, then gradually decreased from local time 03:00. However, in spring, the high RGM period was shifted to midnight (22:00 local time). It lasted 8 until reaching the maximum value in the early morning (06:00 local time). Due to the intensified air flow in spring, the RGM peak took place when urban air was mixed with marine air at CC. We hypothesize it was possible that a low nocturnal boundary layer and mixing of urban air containing nighttime radicals such as NO_3 produced enhanced RGM. This clearly needs to be explored further in more detailed studies.

The largest diurnal RGM amplitude was in summer (0.1 ppqv~1.0 ppqv), followed by spring (0.8 ppqv~1.6 ppqv), fall (0.4 ppqv~1.1 ppqv), and winter (0.6 ppqv~1.1 ppqv). The CC site is usually impacted by the air flow from the Gulf of Mexico, which is cleaner than air over land (Liu et al., 2015). The coastal PBM diurnal pattern (Figure 3.7f) in each season did not show significant variations, the average amplitude was 0.2 ppqv (0.4 ppqv ~0.6 ppqv) with tiny standard deviations. In summary, the amplitude of the PBM diurnal cycle was much smaller than those of RGM, and RGM does not appear to be enhanced in the marine boundary as shown by Ren et al., 2014 at

another site along the Gulf Coast.

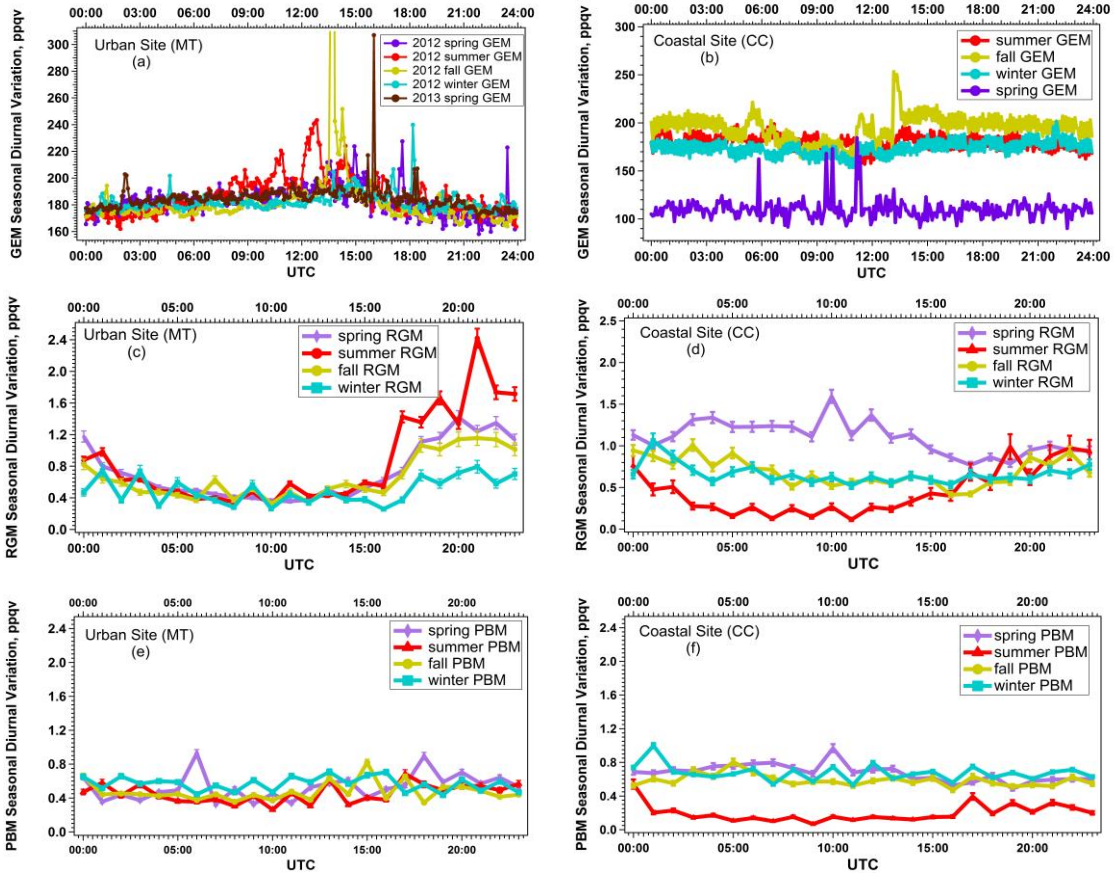

Figure 3.7. Seasonal diurnal variations of GEM, RGM, and PBM at the MT and CC sites.

3.4 Discussion

3.4.1 Relationship with Meteorological Parameters

Rain events typically remove the RGM and PBM species from the middle-to-lower troposphere due to the solubility characteristics of RGM and PBM (Brooks et al., 2010; Ren et al., 2014). Houston experiences thunderstorms or rain events quite often especially in the summer season (Brooks et al., 2010). Understanding the relationship between precipitation and RGM and PBM mixing ratios has importance for mercury cycling. Depicted in Figure 3.8 are the relationships between the precipitation and the

RGM, PBM mixing ratios (during rain events only) at MT (Figure 3.8a) and CC sites (Figure 3.8b). The highest RGM and PBM mixing ratios took place when precipitation was minimal, and lower RGM/PBM levels when it was wet. In Figure 3.8a, the slopes of precipitation and RGM/PBM was -0.04/-0.03, $r^2 = 0.7$ at the urban site. RGM/PBM was -0.01/-0.02, $r^2 = 0.58/0.63$ at the coastal center (Figure 3.8b). All values passed the significance test at $P < 0.05$.

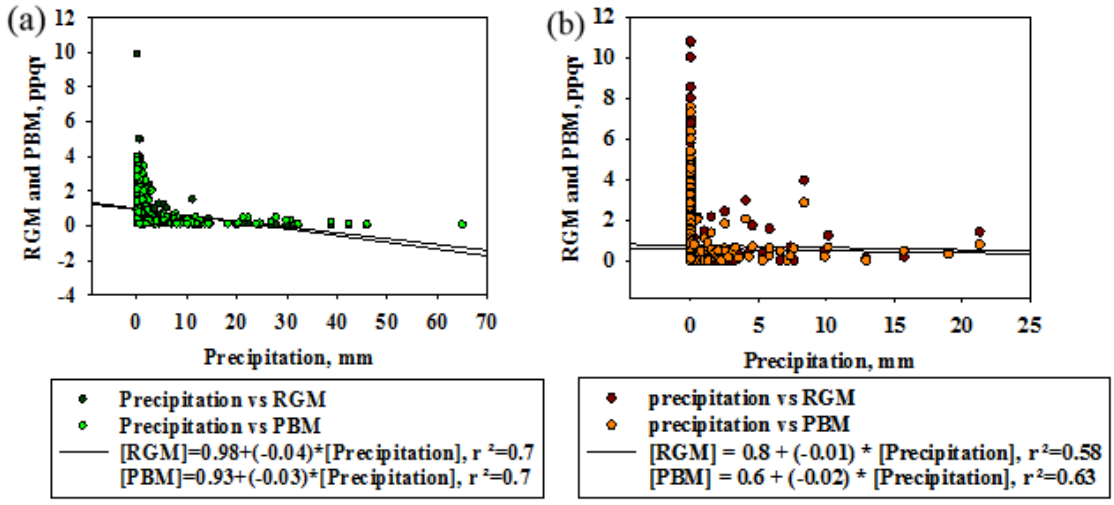

Figure 3.8. Relationship between precipitation, RGM, and PBM.

A comprehensive analysis was conducted to determine which meteorological factors impacted mercury mixing ratios. Figure S3.5~S3.7 demonstrated the relationship between temperature and GEM at both sites. The diurnal patterns of meteorological parameters were analyzed in representative seasons: 2012 spring (Figure 3.9a), 2012 summer (Figure 3.9b), and 2012 fall (Figure 3.9c). The GEM mixing ratios started to increase before the sunrise, meanwhile the boundary layer height and the wind speed reached their minimum values (PBL: 200 ~ 400 m; WS: 3 ~ 4 m/s) around 12:00 UTC and contributed to the diurnal maximum GEM mixing ratio. After sunrise, along with the

increase of temperature, wind speed, and boundary layer height, the more active vertical and horizontal turbulence diluted the mercury species and caused lower GEM mixing ratios. The relationship depicted in Figure 3.9d identifies the striking anti-correlation between boundary layer height and mercury mixing ratios with a slope of -0.32 with R^2 = 0.64, P < 0. 05 at MT.

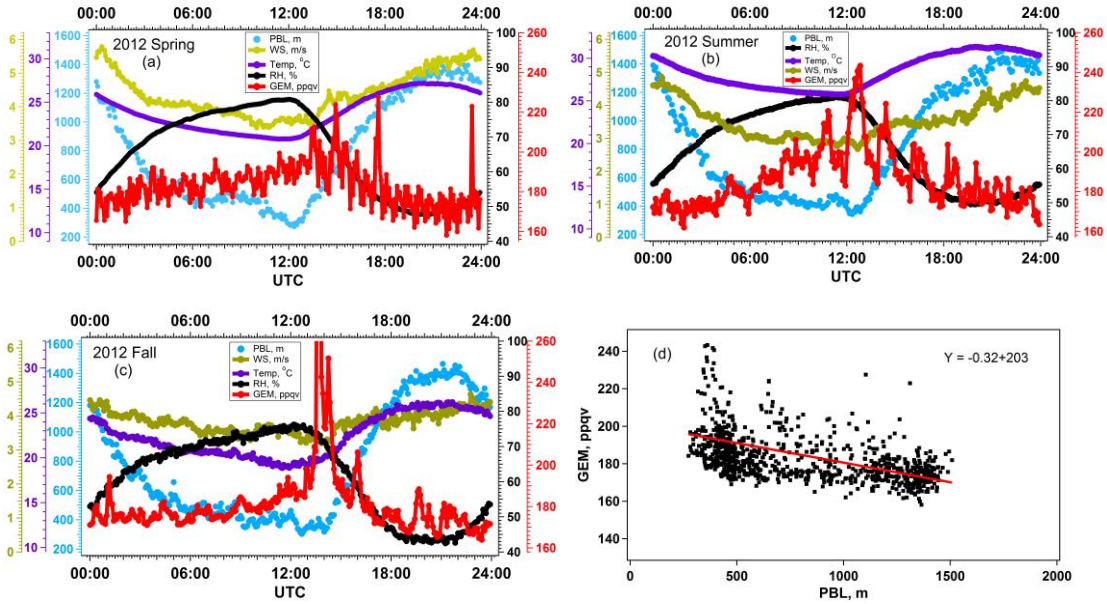

Figure 3.9. Seasonal diurnal variations of mercury versus meteorological factors.

3.4.2 Relationship with Winds

Rose plots unveil the relationship between wind and mercury mixing ratios during the measurement period and are displayed in Figure 3.10. Figure 3.10a shows the wind direction and GEM mixing ratios at the MT site. GEM above 250 ppqv were mainly associated with winds originated from the northeast and southeast, where there is an abundance of urban and industrial emission sources (Houston Ship-channel and Houston-Galveston refinery area). Figure 3.10b illustrates the MT site wind direction and RGM mixing ratios. RGM mixing ratios between 2-8 ppqv are predominantly associated with

southeast winds. Mixing ratios of 1.5-2 ppqv related with south to southeast winds. Northeast winds related with PBM (Figure 3.10c) mixing ratios from 2-3 ppqv, and 1.5-2 ppqv along with east to southeasterly winds.

For the CC site, as seen in Figure 3.10d, winds originated from the Gulf of Mexico associated with GEM mixing ratios below 250 ppqv. GEM above 200 ppqv are predominantly impacted by north or northeast winds. This direction also brings in air with GEM above 500 ppqv. Figure 3.10e and Figure 3.10f describe the relationship between wind direction and RGM/PBM mixing ratios. Both species mostly impacted by winds originated from the south or southeastern directions. RGM levels above 1.5 ppqv, especially 1.5 to 4 ppqv, are associated with air from Gulf of Mexico, however, most of the high RGM levels (6-8 ppqv) originated from the northeastern direction. The Northeasterly winds were also associated with the high PBM mixing ratios over 3 ppqv.

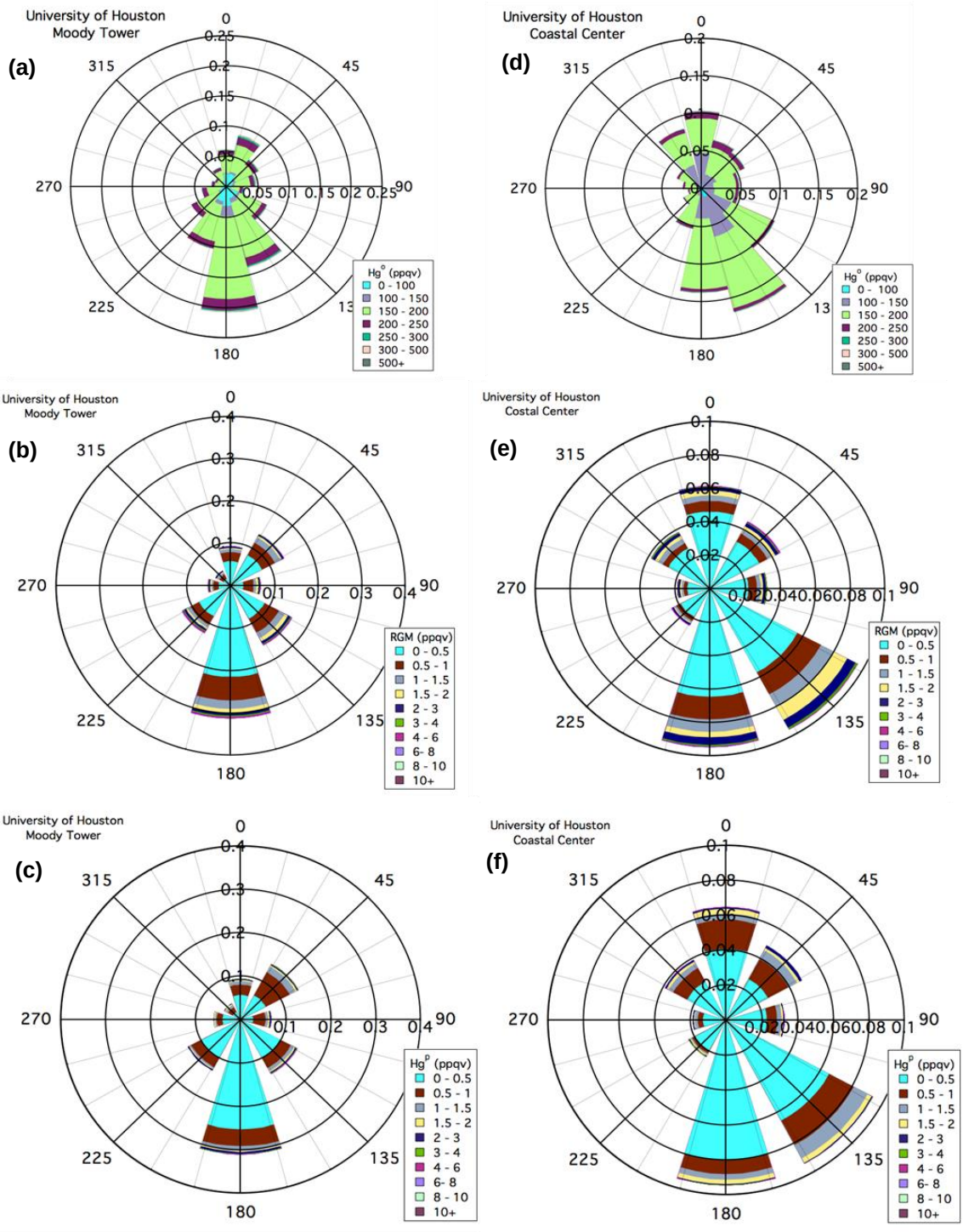

Figure 3.10. Complete mercury species versus wind direction for the MT and CC sites.

The distance between MT and CC sites is only 53 km, however, due to the differences in environmental settings and local anthropogenic emission sources, the GEM monthly median values show significant divergence. As previously mentioned, at the CC site, extremely high monthly median GEM value (260 ppqv) was detected in September, 2012, however, the other months' GEM median values were lower than those measured at MT, and were especially low in April, 2013. A wind rose was constructed for GEM in these two extreme months. Based on Figure 3.11(a), the low GEM period was associated with winds from the southeast. Figure 3.11(b) shows that the high GEM period was consistent with major northerly winds from industrialized areas of Houston. To the north of the CC site, the Houston Ship-channel area, with over 400 oil and gas related facilities present and they are suspected have the high GEM emissions. In contrast, southeasterly winds brought cleaner air from the Gulf of Mexico to CC probably diluting the mixing ratios of GEM and kept the high-mercury air to the north of the site. These variations show the importance of anthropogenic emissions locally and the impact of a clean southerly flow on mercury levels at the coastal site.

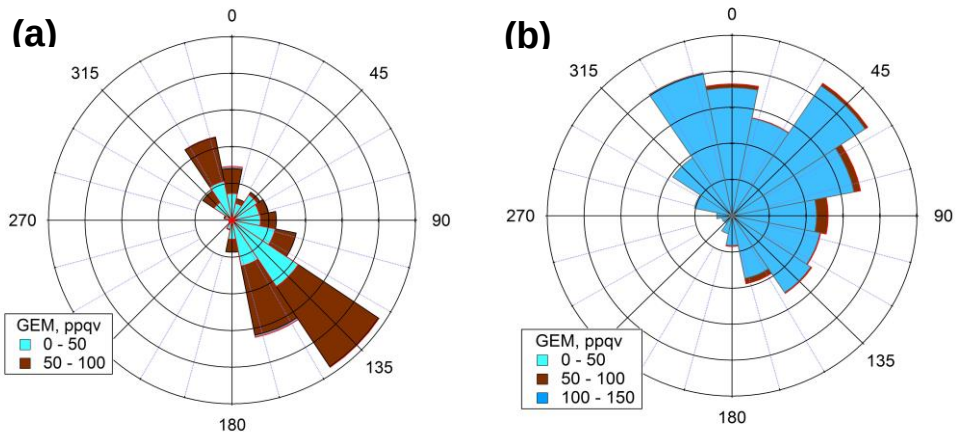

Figure 3.11. Wind rose for the low GEM period (a) and high GEM period (b) at CC site.

3.4.3 Relationship with Key Trace Gases

The MT site CO measurements have proven to be good indicators for long-range transport of pollution, biomass burning, or clean Gulf of Mexico air in Houston (Lefer et al., 2010). According to EPA 2011 National Emission Inventory, oil/petroleum/natural gas related facilities, coal-combustion electrical generating plants, landfills, and waste treatment facilities are major anthropogenic mercury emission sources. Stationary combustion source signatures are distinguishable by their high mixing ratios of SO_2, NO_x, and CO (Brooks et al., 2010). Coal-combustion power plant plumes show relatively strong enhancements in NO_y, SO_2, and CO_2, while CO will typically be negligible (Ryerson et al., 2003). More substantial enhancements of SO_2 are typically associated with coal- and oil-fired units, and are not frequently seen in natural-gas-fired units, the differences can help differentiate power plant emission source types (Ryerson et al., 2003).

A comprehensive investigation of the relationships between mercury species and other key trace gases was conducted, which can provide abundant information on the mercury mixing ratios under two different environmental settings. The positively correlated relationships between mercury mixing ratios and key trace gases mixing ratios are contained in the supplementary material (Figure S3.3-Figure S3.4). Figure 3.12 displays the seasonal diurnal variations of CO_2, CO, NO_x, CH_4, SO_2, O_3, and GEM in representative seasons at the MT and CC sites. The most important feature was the co-occurrence of GEM maximum values, and CO_2, CO, CH_4, SO_2 peak values. Figure 3.12a exhibits the diurnal variations of the key trace gases and GEM in 2012 spring at MT. GEM, CO, and CO_2 had similar diurnal patterns: the significant enhancements began at

04:00 LST and accumulated to the maximum values around 07:00 ~ 07:30 LST, then followed by sudden decreasing trends right after sunrise. The peak values of CO_2, CO, and GEM were 430 ppmv, 230 ppbv, and 210 ppqv. NO_x and O_3 peaked simultaneously at 01:00 LST around midnight, which took place before the enhancements of CO_2, CO, and GEM. Figure 3.12c depicts fall 2012 diurnal variation of selected key trace gases and GEM at the MT site. GEM, CO, CH_4, SO_2, and CO_2 had similar diurnal patterns: the mixing ratio enhancements started at 04:00 ~ 05:00 local time and reached the maximum value at 07:00 ~ 07:30 LST. The peak time of SO_2 was 09:00, 1-2 hours later than the other trace gases. The maximum values of CO_2, CO, CH_4, SO_2, and GEM were 450 ppmv, 330 ppbv, 2.5 ppmv, 0.4 ppbv, and 260 ppqv which were followed by sudden decreasing trends. NO_x peaked at 01:00 LST at 38 ppbv, prior to the enhancements of CO_2, CO, and GEM. The fall 2012 key traces gases together with GEM mixing ratios were highest in the five seasons. Seasonal diurnal patterns for the MT site are seen in Figure 3.12b (2012 summer), Figure 3.12d (2012 winter) and Figure 3.12e (2013 spring) together with Figure 3.12f (2012 summer) for the CC site. The common co-occurrence of GEM, CO, SO_2, CH_4, and CO_2 peaks suggest similar sources for these species. Vehicular emissions are believed to be the primary source of NO_x in urban areas (Frost et al., 2006). The different timing of NO_x peaks with those of Hg suggests that vehicular emissions may not be a significant source of mercury species in the Houston area.

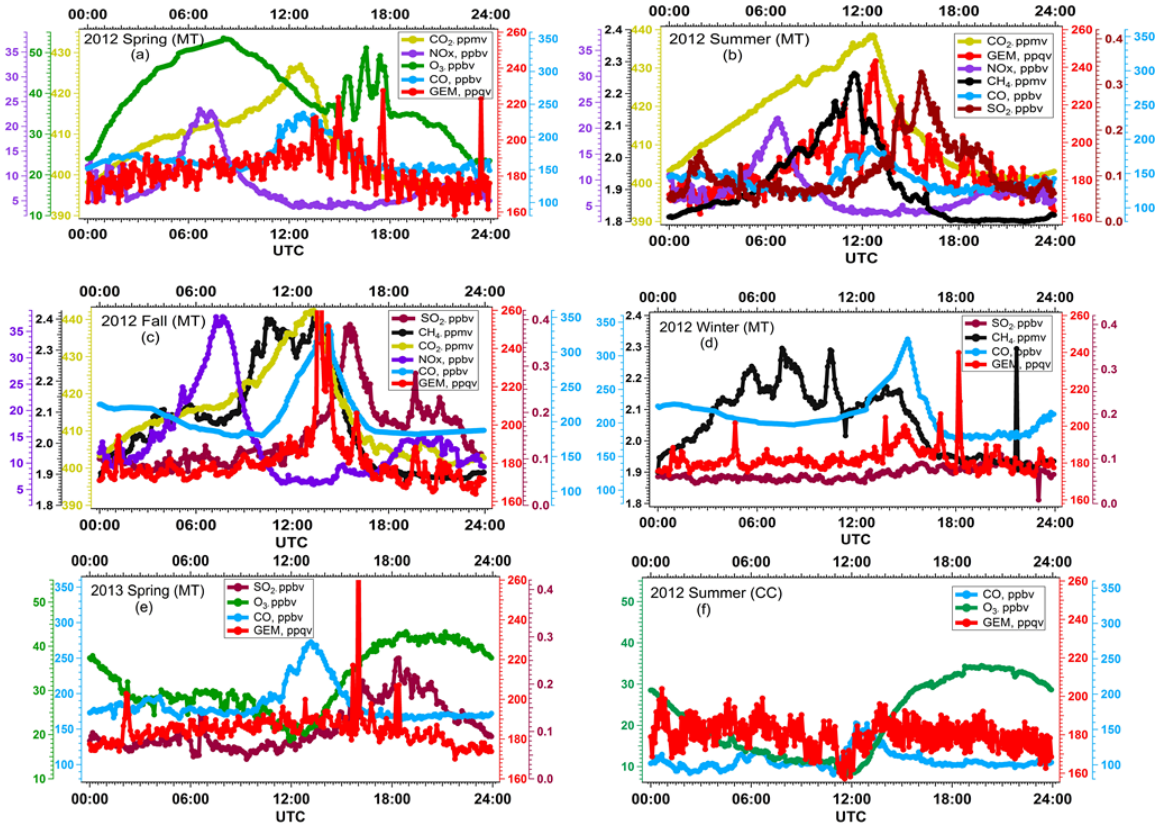

Figure 3.12. Seasonal diurnal variations of mercury versus trace gases at the MT and CC sites.

3.4.4 High Mercury Events

Except identifying Hg peaks at each air quality monitoring facility, key trace gases such as CO, CO_2, and CH_4 were also examined in this study. This allowed first-order identification of signature footprints of the sources for each high mercury event. Plumes from petrochemical complexes are proven to be more difficult to identify only by trace gases since they are known to have enhanced tracer gases characteristic of the embedded power plants that supply electricity and heat to the facilities (Ryerson et al., 2003). Typically the fuels utilized to fire refinery process heaters are those derived from processed petroleum with a higher Hg mixing ratios than other fuel products generally

sold to the public (Wilhelm et al., 2001). For these reasons, after identifying specific pollution plume signatures, wind data is necessary to determine the general direction of the emission sources to narrow down the emission source origin. Identifying the types of the power plant used in the facilities and combining this information with the known wind direction can provide an opportunity to pinpoint the facilities for each event. The combination of co-emitted tracer gasses and wind data can help identify high-Hg sources and determine their impact on Hg levels in southeast Texas.

Here is an analysis of one of the highest mercury events that occurred on April, 2013 at both the MT and CC sites. On April 6, 2013, 14:00 UTC time, the GEM mixing ratio was as high as 4500 ppqv at MT. Here we focus on the study period of 04/05/2013 00:00 ~ 04/07/2013 00:00 UTC time with emphasis on meteorological factors and key traces gases. This high mercury event occurred with the wind direction of 180 ~ 220 degrees, and relative high wind speed of 6 m/s (Figure 3.13a). Based on the 2011 EPA National Emission Inventory (Figure 3.2), the suspect mercury emission sources including the WA Parish plant located southwest of the MT site together with the petrochemical and refinery facilities in Texas City. Figure 3.13b displays the time series of boundary layer height, GEM mixing ratio, O_3, NO_x, CO, CO_2, CH_4, and SO_2 mixing ratios. The most important feature was the co-occurrence of the GEM, CO, CO_2, CH_4, and SO_2 peak values. The significant enhancements of GEM and the key trace gases began at 10:00 ~ 11:00 UTC time on April 6, 2013 and led to concomitant maximum values around 12:00 ~ 13:30 UTC. The peak values of CO_2, CO, CH_4, SO_2, and GEM were 550 ppmv, 600 ppbv, 8.0 ppmv, 1.2 ppbv, and 4500 ppqv. NO_x peaked at 01:00 LST at 160 ppbv. The trace gases mixing ratios were tens to hundreds of times higher

than their normal ranges. An interesting point was the extremely low boundary layer height during the nighttime, only100 m. It was then followed by a sudden increase from 100 m to 2000 m in just 3 hours after the sunrise. The co-occurrence feature of these plumes indicated that GEM, CO, CO_2, CH_4, and SO_2 probably shared the same or related emission sources.

On April 3, 2013, the GEM mixing ratio was as high as 2800 ppqv at the CC site. We analyzed the meteorological factors during the time period 04/02/2013 00:00 - 04/05/2013 00:00 and found the high mercury event occurred at the CC site was in consistent with the wind direction between 10º and 50º (northerly or northeast wind), and wind speeds ~ 4 m/s (Figure 3.13c). Based on the 2011 EPA National Emission Inventory (Figure 3.2), the suspect mercury emission sources are oil and gas related facilities located in the Houston Ship-Channel area. There are so many of them that it is impossible to identify single sources with our available data.

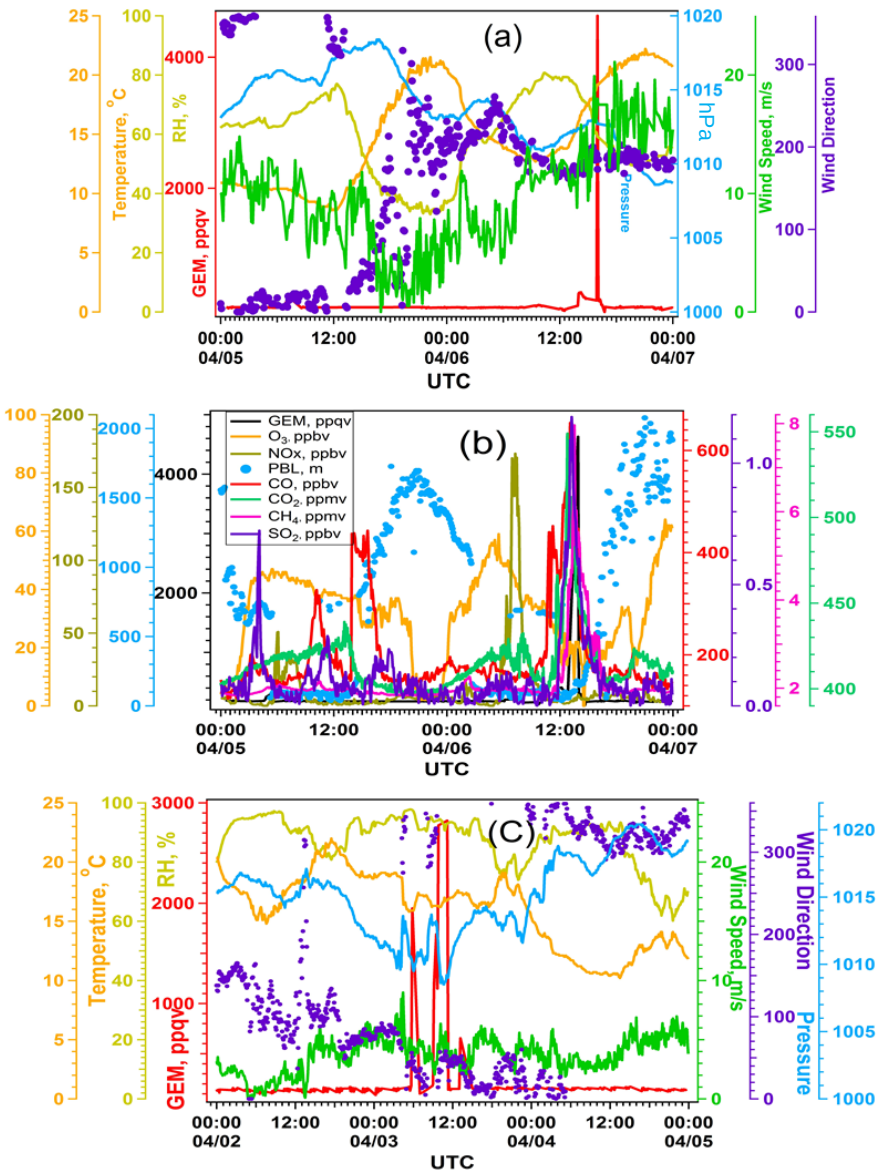

Figure 3.13. Large mercury events single analysis of Hg versus meteorological factors and trace gases at MT and CC.

3.5 Conclusions

Continuous measurements and comprehensive analysis of GEM, RGM, and PBM were conducted under urban and coastal settings in Houston, Texas. This study provides an investigation of mercury characteristics in a city where industrial facilities are highly concentrated. Due to this, the urban setting's GEM mean mixing ratios higher than the

Northern Hemisphere background level. RGM and PBM mean mixing ratios were 6 times higher than the RGM and PBM background level (0.112 ppqv). Under the coastal setting, the mean mixing ratio of GEM was 165 ppqv, equal to the Northern Hemisphere background level however higher than the GEM measured in other coastal sites in the Northeast United States. The mean value of RGM measured at the CC site was 0.75 ppqv, for PBM 0.58 ppqv. Both RGM and PBM mean mixing ratios were 4 times higher than the RGM and PBM Northern Hemisphere background level however lower than the MT. It is probably due to the coastal settings reduction of contaminations by diluting with cleaner air from the Gulf of Mexico. Consequently, the CC site had more frequencies of low mercury events than the MT site.

The seasonal distribution of mercury was small in the Houston area. Seasonal GEM mixing ratios showed tiny differences at MT site but distinct variations at CC, which are probably because of the north and southeast air flows at this site. Lowest median RGM value occurred in 2012 winter at both sites, the 2012 summer exhibited the lowest median/mean PBM mixing ratios. The winter and spring seasons exhibited relatively higher PBM values.

Mercury mixing ratios exhibited pronounced diurnal variations. At MT, GEM increased at midnight and accumulated overnight till reaching the maximum just before sunrise. Then it followed a gradual decrease in the following hours. The CC-diurnal-pattern was different, as GEM exhibited a steady decrease at night and reached its minimum mixing ratio before the sunrise, it slowly increased after the sunrise and reached the maximum mixing ratio in the late morning. We also found the CC RGM peak took place under mixed conditions when urban air mixed with marine air which was

attributed by the intensified southerly flow.

At the MT site, GEM of 100-250 ppqv was associated with winds from the south and southeast, where air mainly originated from the Gulf of Mexico with cleaner background levels. GEM levels above 250 ppqv were in consistent with winds originated mainly from the north or northeast, where air mases accumulated urban and industrial emissions. For the CC site, GEM levels above 200 ppqv were predominantly impacted by winds from the north or northeast.

The relationships between mercury species and key trace gases were conducted, the co-occurrence of GEM, CO_2, CO, CH_4, SO_2 maximum values at MT and GEM, CO peak at CC were striking. It reveals that GEM, CO, CO_2, CH_4, and SO_2 probably shared the same or related emission sources.

The future work is strongly warranted to quantify the emission sources combining modeling and observational work. We strongly suggest conducting ground measurements to quantify emission sources with our mobile laboratory. For a better understanding of these source signatures, future studies should include the measurements of $\delta^{13}C$ in CH_4, as well as the sampling of oil and gas emissions under urban and coastal settings in southeastern Texas.

3.6 Acknowledgements

The authors would like to thank Patrick Laine and other members in the Institute for Climate and Atmospheric Sciences at University of Houston for measuring and compiling the mercury data, meteorology, and key trace gases data and we express our sincere appreciation to Dr. Xun Jiang who provided insightful suggestions.

3.7 References

Banta R.M., Senff C.J., Gammon J.N., Darby L.S., Ryerson T.B., Alvarez R.J., Sandberg S.P., Williams E.J., and Trainer M., A bad air day in Houston. *Bull. Am. Meteorol.* Soc. 86, 657-669, 2005.

Brooks S., Luke W., Cohen M., Kelly P., Lefer B., and Rappengluck B., Mercury species measured atop the Moody Tower TRAMP site, Houston, Texas. *Atmos. Environ.* 44, 4045–4055, 2010.

Cheng I., Zhang L., Mao H., Blanchard P., Tordon R., and Dalziel J., Seasonal and diurnal patterns of speciated atmospheric mercury at a coastal-rural and a coastal-urban site. *Atmos. Environ*. 82, 193-205, 2014.

Engle M.A., Tate M.T., Krabbenhoft D.P., Schauer J.J., Kolker A., Shanley J.B., and Bothner M.H., Comparison of atmospheric mercury speciation and deposition at nine sites across central and eastern North America. *J. Geophys. Res.*115, 18306, 2010.

Frost G. J., McKeen S. A., Trainer M., Ryerson T. B., Neuman J. A., and Roberts J. M., Effects of changing power plant NOx emissions on ozone in the eastern United States: Proof of concept. . *J. Geophys. Res*. 10, 1029, 2006.

Gabriela M.C., Williamsona D.G., Brooks S., and Lindberg S., Atmospheric speciation of mercury in two contrasting Southeastern US airsheds. *Atmos. Environ*. 39, 4947–4958, 2005.

Holmes C.D., Jacob D.J., Yang X., Global lifetime of elemental mercury against oxidation by atomic bromine in the free troposphere. *Geoph. Research. Lett.*, 10, 1029-1076, 2006.

Jaffe D.A., Lyman S., Amos H.M., Gustin M.S., Huang J., Selin N.E., Levin L., Schure A., Mason R.P., Talbot R., Rutter A., Finley B., Jaeglé L., Shah V., McClure C., Ambrose J., Gratz L., Lindberg S., Weiss-Penzias P., Sheu G.R., Feddersen D., Horvat M., Dastoor A., Hynes A.J., Mao H., Sonke J.E., Slemr F., Fisher J.A., Ebinghaus R., Zhang Y., and Edwards G., Progress on Understanding Atmospheric Mercury Hampered by Uncertain Measurements. *Environ. Sci. Technol.* 48 (13), 7204–7206, 2014.

Keeler G., Glinsorn G., and Pirrone N., Particulate mercury in the atmosphere: its significance, transport, transformation and sources. *Water Air Soil Pollut*. 80, 159–168, 1995.

Lan X., Talbot R., Laine P., Lefer B., Flynn J., Sun Z., Torres A., Seasonal and diurnal variations of total gaseous mercury in urban Houston, Texas (U.S.A.). *Atmos. 5*, 399-419, 2014.

Lan X., Talbot R., Castro M., Perry K., Luke W., Seasonal and diurnal variations of atmospheric mercury across the US determined from AMNet monitoring data. *Atmos. Chem. Phys*., 12, 10569–10582, 2012.

Laurier F.J., Mason R.P., Whalin L., Kato S., Reactive gaseous mercury formation in the North Pacific Ocean's marine boundary layer: A potential role of halogen chemistry, *J. Geophys. Res.* 10, 1029-1088, 2003.

Lefer B., Rappenglück B., Flynn J., Haman C., Photochemical and meteorological relationships during the Texas-II Radical and Aerosol Measurement Project (TRAMP). *Atmos. Environ*. 44, 4005-4013, 2010.

Liu L., Talbot R., Lan X., Influence of Climate Change and Meteorological Factors on Houston's Air Pollution: Ozone a Case Study, *Atmos*. 6, 623-640, 2015.

Liu B., Keeler G.J., Dvonch J.T., Barres J.A., Lynam M.M., Marsik F.J., Morgan T.J., Temporal variability of mercury speciation in urban air. *Atmos. Environ*. 10, 1063, 2007.

Lyman S.N., Jaffe D.A., Gustin M.S., Release of mercury halides from KCl denuders in the presence of ozone. *Atmos. Chem. Phys*. 10, 8197-8204, 2010.

Malcolm E.G., Keeler G.J., Landis M.S., The effects of the coastal environment on the atmospheric mercury cycle. *J. Geophys. Res.* 10, 1029-1050, 2003.

Mao H., and Talbot R., Speciated mercury at marine, coastal, and inland sites in New England – Part 1: Temporal variability, *Atmos. Chem. Phys.* 12, 5099-5112, 2012.

Nair U.S., Wu Y., Walters J., Jansen J., Edgerton E.S., Diurnal and seasonal variation of mercury species at coastal-suburban, urban, and rural sites in the southeastern United States. *Atmos. Environ*. 499-508, 2011.

Obrist D., Tas E., Peleg M., Matveev V., Faïn X., Asaf D., Luria M., Bromine-induced oxidation of mercury in the mid-latitude atmosphere. *Nature Geoscience* 4, 22–26, 2011.

Pirrone N., Keeler G. J., and Nriagu J., Regional differences in worldwide emissions of mercury to the atmosphere. *Atmos. Environ*. 17, 2981–2987, 1996.

Pirrone N., Costa P., Pacyna J. M., and Ferrara R., Mercury emissions to the atmosphere from natural and anthropogenic sources in the Mediterranean region. *Atmos. Environ.* 35, 2997–3006, 2001.

Ren X.R., Luke W.T., Kelle P., Cohen M., and Ngan F., *Atmos*. 5, 230-251, 2014.

Rutter A.P., Snyder D. C., Stone E.A., Schauer J.J., In situ measurements of speciated atmospheric mercury and the identification of source regions in the Mexico City Metropolitan Area. *Atmos. Chem. Phys*. 9, 207-220, 2007.

Ryerson T. B., Trainer M., Angevine W. M., Brock C. A., Dissly R. W., Fehsenfeld F. C., Frost G. J., Goldan P. D., Holloway J. S., Hu¨bler G., Jakoubek R. O., Kuster W. C., Neuman J. A., Nicks Jr. D. K., Parrish D. D., Roberts J. M., Sueper D. T., Atlas E. L., Donnelly S. G., Flocke F., Fried A., Potter W. T., Schauffler S., Stroud V., Weinheimer A. J., Wert B. P., Wiedinmyer C., Alvarez R. J., Banta R. M., Darby L. S., Senff C. J., Effect of petrochemical industrial emissions of reactive alkenes and NO_x on tropospheric ozone formation in Houston, Texas. *J. Geophys. Res.* 108, 4249, 2003.

Schroeder W. H., Munthe J., Atmospheric mercury – an overview. *Atmos. Environ*. 5, 809–822, 1998.

Sigler J. M., Mao H., Sive B.C., Talbot R., Oceanic influence on atmospheric mercury at coastal and inland sites: a springtime noreaster in New England. *Atmos. Chem. Phys.* 9, 4023-4030, 2009.

Skov H., Brooks S.B., Goodsite M.E., Lindberg S.E., Meyers T.P., Landis M.S., Larsen M.R.B., Jensen B., McConville G., Christensen J., Fluxes of reactive gaseous mercury measured with a newly developed method using relaxed eddy accumulation. *Atmos. Environ*. 40, 5452–5463, 2006.

Sprovieri F., Pirrone N., Ebinghaus R., Kock H., Dommergue A., A review of worldwide atmospheric mercury measurements. *Atmos. Chem. Phys.* 10, 8245–8265, 2010.

Valente R.J., Shea C., Atmospheric mercury in the Great Smoky Mountains compared to regional and global levels. *Atmos. Environ*. 1861–1873, 2007.

Wilhelm S. M., Estimate of Mercury Emissions to the Atmosphere from Petroleum, *Environ. Sci. Technol. 35 (24),* 4704-4710, 2001.

Yang Y., Chen H., Wang D., Spatial and temporal distribution of gaseous elemental mercury in Chongqing, China. *Environ Monit Assess* 156, 479–489, 2009.

Zhu J.L., Wang T., Talbot R., Mao H, Characteristics of atmospheric Total Gaseous Mercury (TGM) observed in urban Nanjing, China. *Atmos. Chem. Phys*. 12, 12103-12118, 2012.

3.8 Supporting Materials

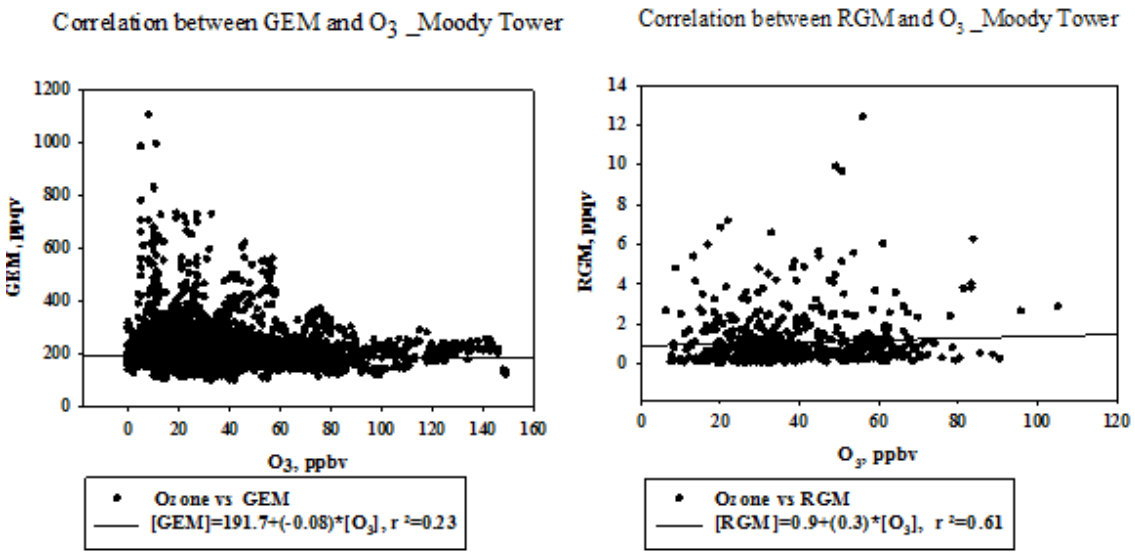

Figure S3.1. Relationship between GEM/RGM and ozone mixing ratio at the Moody Tower site.

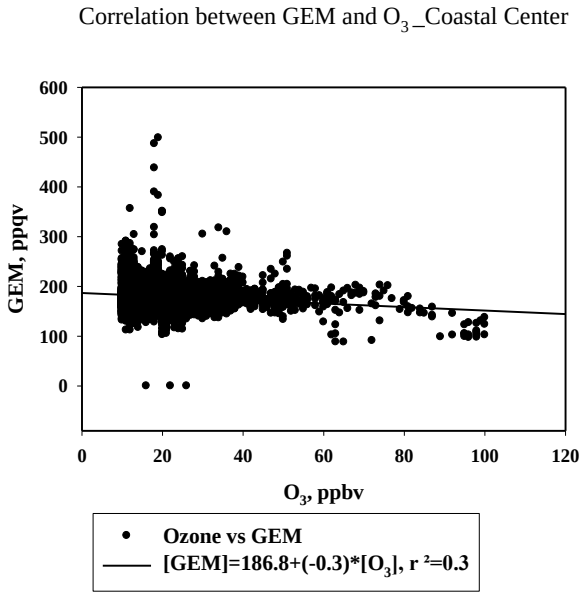

Figure S3.2. Relationship between GEM and ozone mixing ratio at the Coastal Center site.

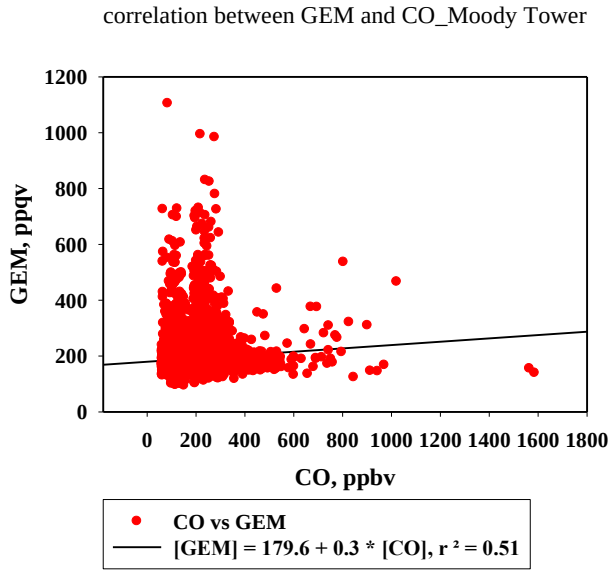

Fiure S3.3. Relationship between GEM mixing ratio and CO mixing ratio at the Moody Tower site.

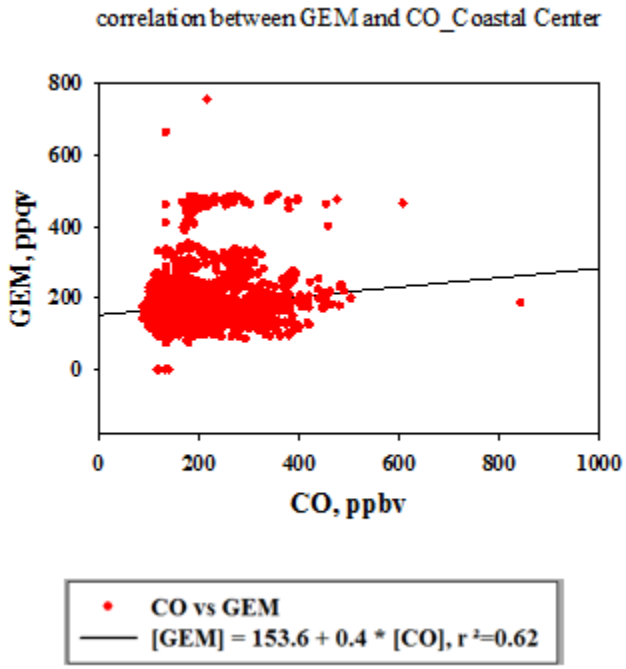

Figure S3.4. Relationship between GEM mixing ratio and CO mixing ratio at the Coastal Center site.

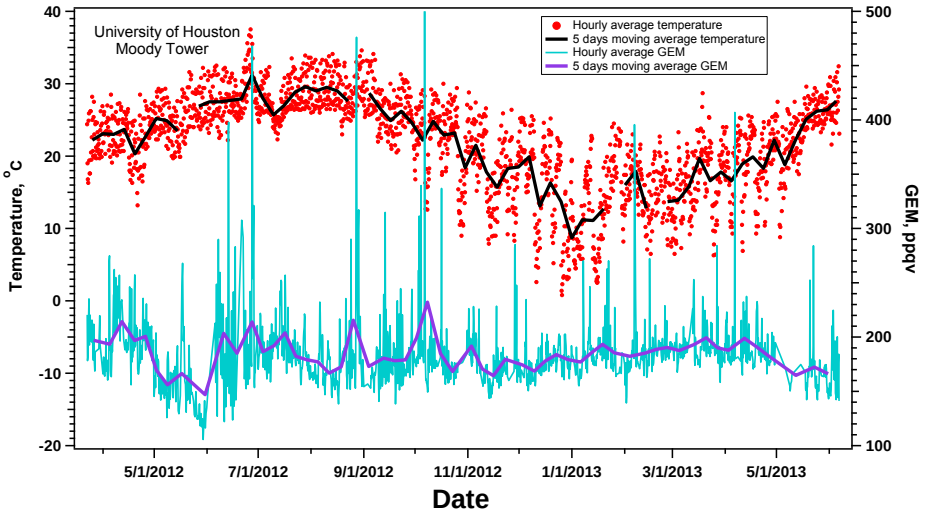

Figure S3.5. The complete time series of GEM mixing ratio and temperature along with the 5 days moving averages at the Moody Tower site.

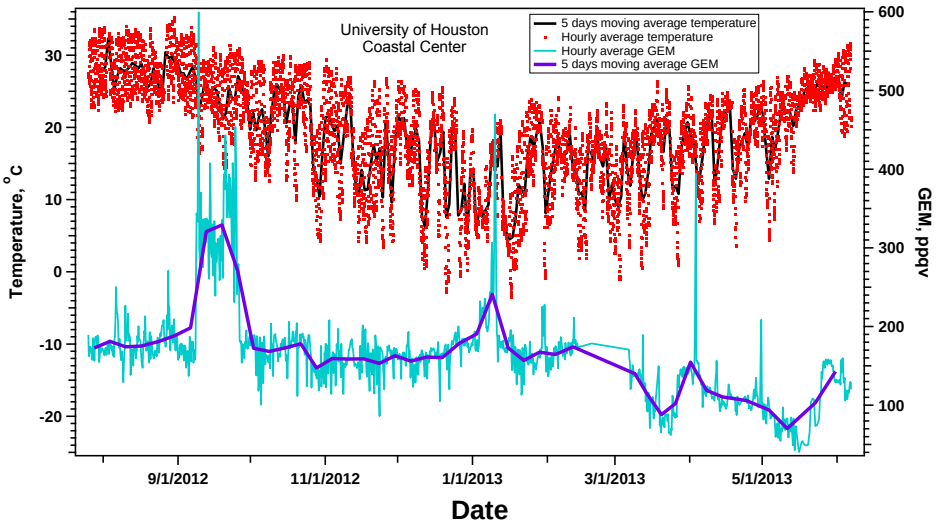

Figure S3.6. The complete time series of GEM mixing ratio and temperature along with the 5 days moving averages at the Coastal Center site.

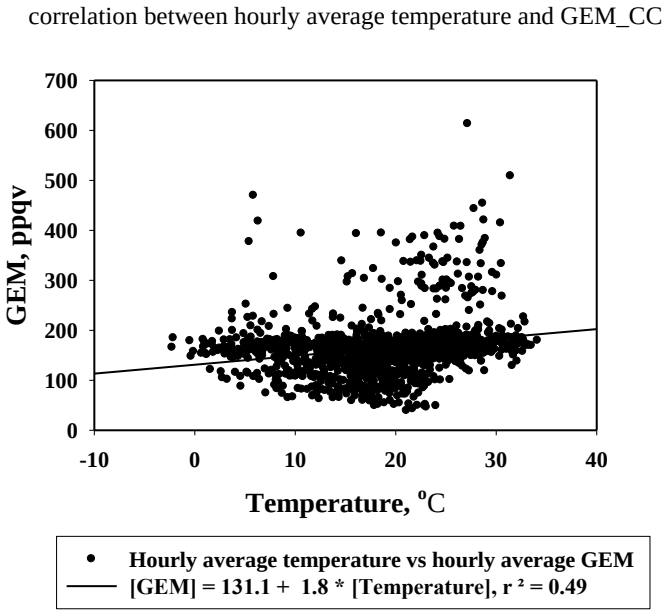

Figure S3.7. Relationship between hourly averaged GEM mixing ratio and temperature at the Coastal Center site.

Chapter 4

Emission Estimates of Trace Gases and Volatile Organic Compounds From a Prescribed Grassland Fire in Southeastern Texas[4]

4.1 Introduction

Biomass burning is the largest global source of primary fine carbonaceous particles and the second largest source of numerous important atmospheric trace gases (Andreae and Merlet, 2001; Yokelson et al., 1999a; Shirai et al., 2003). The open combustion of biomass is the key pathway by which humans directly affect the chemical and radiative properties of the atmosphere (Wooster et al., 2011; Bowman et al., 2009). Particles formed and emitted from biomass burning, primarily black carbon and organics, play an important role in the Earth's radiation balance and climate through their scattering and absorption properties (Ferek et al., 1998; Akagi et al., 2011; Andreae et al., 1988). Trace gases emitted from biomass burning have significant influences on the atmosphere (Sudo and Akimoto, 2007; Akagi et al., 2011), especially in tropical and subtropical regions (Koppmann et al., 1997; Andreae et al., 1997). For example, carbon monoxide (CO), methane (CH_4), and volatile organic compounds (VOCs) affect the oxidation capacity of the troposphere by reacting with OH radicals (Crutzen and

[4] Material in this chapter to be published:

Liu L., Talbot R., Lan X., Sive B., Lefer B., Flynn J., and Judd L., Emission Estimates of Trace Gases and Volatile Organic Compounds from a Prescribed Grassland Fire in Southeastern Texas, pending submission, 2016.

Andreae, 1990; Singh et al., 1995). Nitric oxide (NO) and VOC emissions lead to the formation of tropospheric ozone (O_3) and other photo oxidants (Schultz et al., 1999). Biomass burning is also a major source of methyl chloride (CH_3Cl), methyl bromide (CH_3Br), and a minor source of methyl iodide (CH_3I), which potentially delivers halogens to the stratosphere and causes O_3 depletion (Andreae et al., 1996; Blake et al., 1996). Trace gases from biomass burning, in particular NO_x and SO_2, are considerable sources of secondary aerosols (Alvarado and Prinn, 2009). Due to the long tropospheric lifetime of methane (CH_4) and its large global warming potential, global biomass burning events have direct impacts on the global CH_4 balance and climate change (Power et al., 2013; Keywood et al., 2013). Therefore, there is an increasing need for comprehensive information on biomass burning and trace gas and aerosol emissions (Koppmann et al., 2005; Goode and Yokelson, 1999).

According to previous work (Crutzen and Andreae, 1990; Hao and Liu, 1994; Koppmann et al., 2005), grassland and savanna fires are the single largest source of biomass burning emissions globally. However, there are only a relatively small number of studies that have reported emissions from grassland and savanna fires (Hurst et al., 1994a, 1994b; Wooster et al., 2011). There are even less studies of emission of trace gases from domestic grassland and savanna fires in the United States (Koppmann et al., 2005). Trace gases originating from biomass burning show variations dependent on burnt fuel mass, moisture, fuel composition and different stages of the fire (Christian et al., 2003; Freeborn et al., 2008; Andreae and Merlet, 2001; Burling et al., 2010). Full fire lifecycle emissions are seldom directly measured, except for laboratory studies under controlled conditions where the fuel load and compositions are typically known. Only a

few observations of the chemical evolution of individual biomass burning fires have been conducted previously (Yokelson et al., 2009; Hobbs et al., 2003; Goode et al., 2000).

Our experiment is unique because the sampling inlets were close (meters) to the controlled burn and we provide detailed in-situ measurements of trace gases and VOC emissions throughout the ignition, flaming, and smoldering phases of a prescribed grassland fire. The pre-burn and post-burn vegetation samplings were also conducted to characterize the structure, composition and loading of combustible material within the burn unit. Thus, this controlled experiment will add comprehensive and direct information of important trace gases and VOC emissions from biomass burning to our limited knowledge on this topic, and act as a reference point for future airborne/ground grassland and savanna combustion measurements.

4.2 Experimental and Methodology

4.2.1 Experimental

On January 30, 2013, a controlled burn experiment was conducted by the Texas Forest Service at University of Houston Coastal Center (UHCC), in which 0.63 km^2 (155 acres) of a grass field was burned. The UHCC is an environmental research center located 45 km southeast of the Houston downtown area and 22 km from the western shore of the Gulf Coast (Liu et al., 2015), that contains 300 acres of coastal tall-grass prairie consisting of a mixture of native grasses: big bluestem, little bluestem, and long-spike tridens (Clements et al., 2007). The fire on UHCC's prairie land was ideal for this research because the size of land used provided a large and long burn for a detailed analysis to be conducted. Pre-burn sampling was conducted on January 4, 2013. Post-burn sampling was conducted on February 7, 2013. Forty-six destructive clip plots were

established on a systematic grid within the burn unit at 25 meter spacing. The biomass consumption for each vegetation category was determined by subtracting pre-burn loadings from post-burn loadings. The average fuel loading per unit in this fire experiment was 2.88 tons/acre. Fuel moisture sampling was also conducted within 30 minutes of ignition for each burn unit, the average moisture content of the fuel was 15%.

Figure 4.1. Example photographs of this controlled grassland fire and the mobile laboratory inlets.

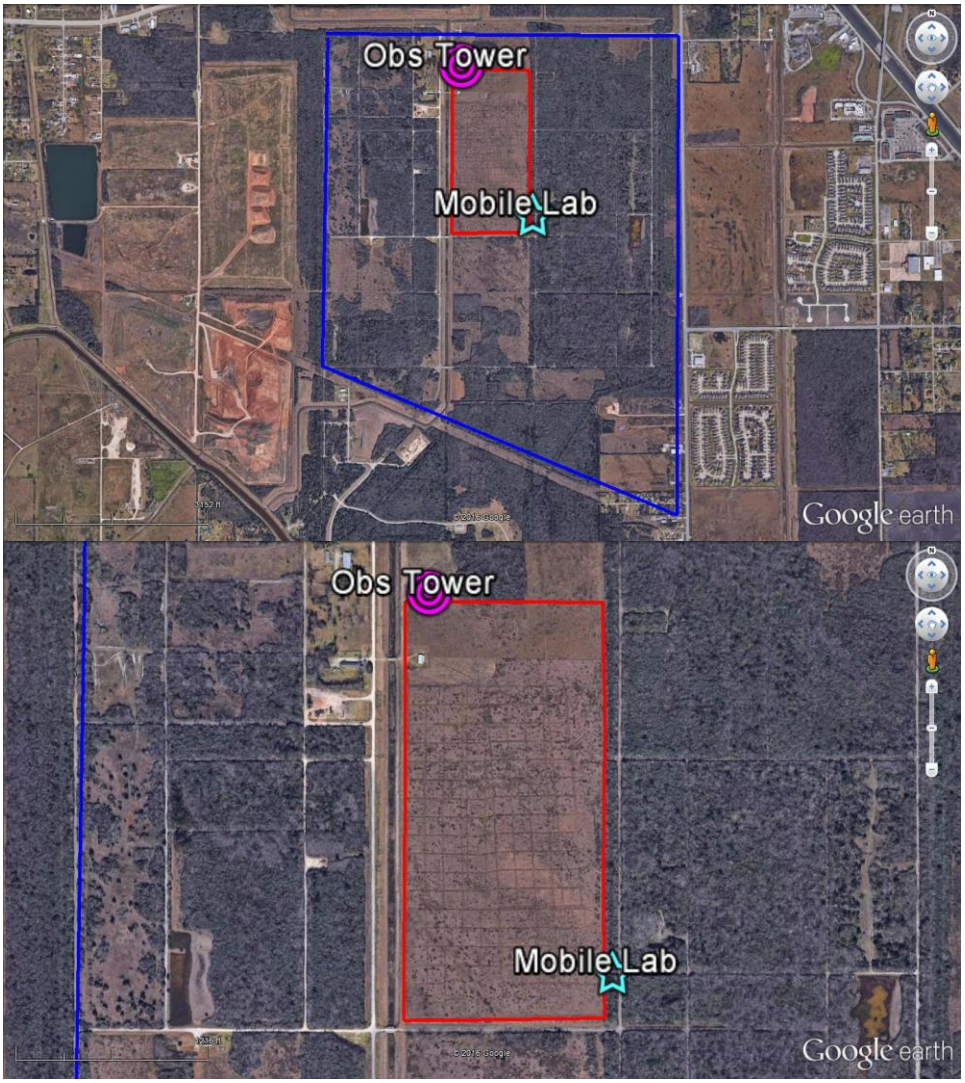

Figure 4.2. Map of the experimental setup. Blue box indicates the University of Houston Coastal Center. Red box indicates the burned area.

The fire experiment was conducted under moderate wind conditions (average wind speed = 10 m/s, northwest wind) (Figure 4.1). Our mobile laboratory was parked at the downwind boarder of the burn and measured trace gases continuously before, during and after the burn (Figure 4.2). Total gaseous mercury (THg = Hg^0 + GOM [gaseous oxidized mercury]), carbon monoxide (CO), carbon dioxide (CO_2), methane (CH_4), and nitrogen oxides (NO, NO_y) measured by the mobile laboratory can provide important

information on fresh biomass burning emissions. A Model 2537A mercury vapor analyzer was employing a Cold Vapor Atomic Fluorescence Spectrophotometry (CVSFS) for THg detection with a detection limit of <0.1 ng/m^3 and a range of 0.1-2000 ng/m^3 with 2.5 min resolution (Lan et al., 2014). Instrument calibration was checked daily using the internal mercury permeation source. The internal standard was verified every month using a Tekran 2505 unit. Carbon dioxide was measured using a LI-COR LI-7000 analyzer with time resolution of 1.0 ~ 1.5 second. Methane was measured with a Picarro G-2132i cavity ring-down instrument with 1.0 ~1.5 second resolution. Nitrogen oxides were measured with Thermo NO-NO_2-NO_x analyzer with 10-second resolution and blue light converter for NO_2 (Luke et al., 2010). Standard for all trace gases were obtained from Scott-Marrin and were NIST certified to ±1%.

Volatile organic compounds (VOCs) whole air samples were collected in 2-liter electro-polished, stainless steel canisters throughout each phase of the fire including pre-burn, ignition, growth, full development, and decay for a total of 16 samples over a 120 min period at the same location as the mobile lab. The canisters were analyzed using two analytical systems as described by Sive et al. (2005). The first system conducted analysis using a gas chromatography with flame ionization and electron capture detection (FID and ECD) in conjunction with mass spectrometry. The 2-GC, 1 GC-MS analytical system was used to quantity a suite of C_2-C_{10} non-methane hydrocarbons, C_1-C_2 halocarbons, C_1-C_5 alkyl nitrates, oxygenated volatile organic compounds, and reduced sulfur gases. The analysis was performed by cryogenic pre- concentration of a 1256 cm^3 (STP) sample aliquot. The second system conducted analysis by means of gas chromatograph using

FID to quantify methane and carbon dioxide. A 5-cm^3 (STP) aliquot sample was used to quantify CH_4 and CO_2. Calibration used the methods described by Sive et al. (2005).

4.2.2 Methodology

Emission information is represented by two basic forms: emission ratios and emission factors (Andreae et al., 2001). Biomass burning emissions are commonly characterized by determining the emission ratio (Shirai et al., 2003): dividing the "excess" trace species concentrations measured in a fire plume by the "excess" concentration of a simultaneously measured reference gas, for example CO (a good reference tracer of smoldering combustion) or CO_2 (reference tracer for flaming products). "Excess" indicates the ambient background concentrations must be subtracted from the values measured in the smoke (Andreae and Merlet, 2001). Meanwhile, for the VOCs measured by canisters, the emission ratio can be determined as the regression slope of the species versus the reference tracer.

Emission factor is defined as the amount of a trace species compound released per amount of dry fuel consumed, in units of g/kg. To calculate this parameter, the carbon contents of the fuel burned and the carbon budgets are required, in the controlled fire experiment, those information are available.

$$EF[x] = \frac{M[x]}{M[b]} = \frac{M[x]}{M[c]}[C]_{biomass},$$

M[c] is the mass of carbon emitted, $[C]_{biomass}$ is the carbon concentration in the biomass burned.

Emission factor can also be calculated as:

$$\text{Emission Factor}_x = \text{Emission Ratio}_{(x/y)} \frac{MWx}{MWy} \text{Emission Factor}_y$$

ER(x/y) is the emission ratio of species x relative to the reference species y, MW_x and MWy are the molecular weights of the species x and the reference tracer y, EF_y is the emission factor of the reference tracer y.

To determine the combustion status, quantify the relative amounts of flaming (complete combustion) and smoldering (incomplete combustion), combustion efficiency is a useful way. When CE > 90%, a fire is generally in the flaming phase, and when CE is less than 85%, it is in the smoldering phase (Ward and Hardy, 1991). The modified combustion efficiency is the simplified combustion efficiency, defined as:

$MCE = \Delta CO_2 / (\Delta CO + \Delta CO_2)$

To better assess the impacts from biomass burning to atmospheric environment, the total emissions of each trace species in a single fire event is defined as (Koppmann et al., 2005):

Total Emissions of species N = M*F*C*EF* S,

M is the amount of fuel mass for combustion per unit area in kg/m^2, F is the mass fraction of carbon in the fuel (54% in this experiment), C represents the combustion factor (fraction of that mass combusted during the coarse of a fire, in this experiment, pre / post dry fuel mass = 90%), EF is the combustion averaged emission factor for species N in unit of g/kg, and S is the total burned area in this single fire experiment in unit of m^2.

4.3 Results

4.3.1 General Characteristics of Fire Emitted Trace Species

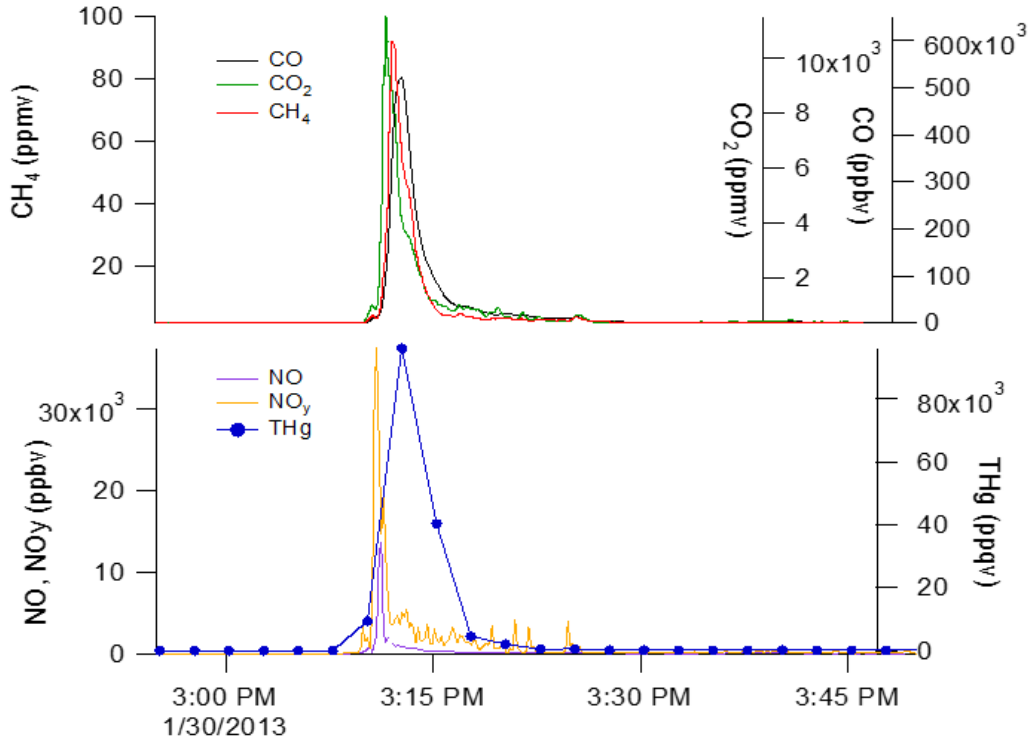

Figure 4.3. Time series of trace species measured with the mobile laboratory. The THg peak is offset from the others due to the averaging time of the measurement.

Figure 4.3 depicts the time series of trace species, CO, CO_2, CH_4, NO, NO_y, and THg, measured with the mobile lab in this grassland fire experiment. The background value of each trace species was also measured before the ignition (CO = 149 ppbv, CO_2 = 391 ppmv, CH_4 = 1.88 ppmv, NO = 0.137 ppbv, NO_y = 1.88 ppbv, and THg =145 ppqv). As an important greenhouse gas, CO_2 is the main compound emitted from combustion of organic materials. The CO_2 concentration began to increase at local time 15:09, and three minutes later (15:12), the peak value was detected as high as 11500 ppmv, twenty-seven

times higher than the background value. CO_2 then decreased to 800 ppmv at 15:16. Because of the co-occurrence with the high CO_2 time period and the main plume time period (15:10-15:18), we conclude that most of the CO_2 was emitted within the plume period. CH_4 is an important greenhouse gas and biomass burning is its third largest source globally (IPCC, 2013). Starting from 15:09, the CH_4 mixing ratio increased from its background value of 1.88 ppmv to 90 ppmv in four minutes, then decreased to 2 ppmv in the following five minutes with the decreasing rate of 0.29 ppmv/second. The CH_4 peak time is one minute later than that of CO_2, and the time period of high CH_4 matches well with the plume time. As the good reference tracer of smoldering combustion, CO is well correlated with most gaseous compounds emitted during the smoldering stage. In our study, the CO mixing ratio starts to increase when the plume begins at 15:09, and reaches its peak at 500,000 ppbv, at 15:14. This peak time is one minute later than that of CH_4. The CO mixing ratio decreased to the background level in the following eight minutes.

Recent research has shown that emissions of Hg from fires can be significant (Wiedinmyer et al., 2007), however, the emission details has not been well studied. In this study, we measured the total gaseous mercury throughout the whole fire stages. We found the high Hg period correlated well with the plume time, THg concentration reaches its peak at local time 15:14, at 88,000 ppqv, and it was 600 times higher than its background value. THg mixing ratio then decreased to its background level within the following eight minutes. THg time series and peak time correlated well with that of CO. The peak time of NO and NO_y are three minutes earlier than the THg peak time, and the co-occurrence with the peak time of CO_2 is striking. The NO_y peak value (40,000 ppbv) is

20,000 times higher than its background value and it took 13 minutes to decrease the NO_y mixing ratio from its peak down to the background level.

All trace species measured by the mobile laboratory showed single-peak characteristics and their peak times matched well with the fire plume time. However, as Figure 4.4 demonstrates, the VOCs show double peaks features in this fire experiment. The time series plots illustrate a primary spike in VOC signatures at local time 15:12 for all gases analyzed, with a secondary spike at time 15:22, except for CO_2. These spikes correspond to multiple fire phases, causing the VOCs to become enhanced, then relaxed emissions, and then enhanced again at a second time during smoldering. This was different for CO_2 since it is a minor product during the smoldering phase, in which the other VOCs become enhanced. The most pronounced second peaks occurred for CH_4, C_2H_6, n-C_4H_{10}, and n-C_5H_{12}.

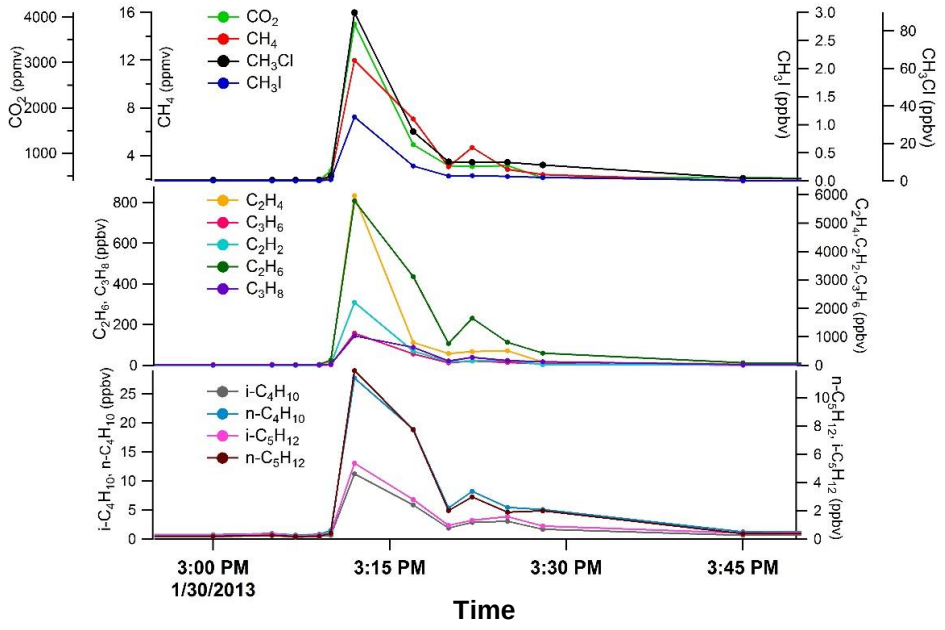

Figure 4.4. Times series of VOCs during different phases of the fire.

4.3.2 Emission Ratios

As demonstrated in Table 4.1, CO_2 evolved primarily in the flaming stage and CO is the reference species for the smoldering stage (Hurst et al., 1994), the fire stages were classified as flaming, smoldering, and total stage combustions based on the modified combustion efficiency. The excess mixing ratio of each measured trace species is plotted against ΔCO_2 and ΔCO, the correlation is determined from the correlation coefficients (R^2).

For the VOC emission ratios (Table 4.1a), CH_4 is well correlated with CO (0.81) and CO_2 (0.89), it indicates that there are CH_4 emissions during both flaming and smoldering stages, however, its emission ratio relative to CO is seven times higher than its emission ratio relative to CO_2 (ppbv/ppbv). The CH_4 emissions were primarily emitted during the smoldering stage in this fire. Volatile organic compounds CH_3Cl, CH_3I, C_2H_4, C_2H_2, n-C_6H_{14}, C_6H_6, 1-C_4H_8, and n-C_8H_{18} are species highly correlated with CO and CO_2 ($R^2 > 0.95$) through the fire, and their emission ratios with CO are at least 10 times higher than those with CO_2, showing that these species are primarily emitted during the smoldering stage like CH_4. For species like C_2H_6, C_3H_8, C_3H_6, i-C_4H_{10}, n-C_4H_{10}, i-C_5H_{12}, n-C_5H_{12}, C_5H_8, C_7H_8, C_8H_{10}, t-2-C_4H_8, 2,2,4-TMP, and m+p-Xylene, their correlation coefficients R^2 with CO_2 and CO distributed between 0.70 and 0.95, less correlated with CO or CO_2 than the VOC species we listed previously, but their emission ratios relative to CO are at least 10 times higher than those with CO_2 as well; they are primarily emitted during the smoldering stage like most VOCs. This result matches well with conclusions that the emission of hydrocarbons is associated with smoldering combustion and VOCs are better correlated with CO than with CO_2 regard less of the vegetation type (Ferek et

al., 1998). Species have relative high emission ratios relative to CO_2 and CO include CH_4, C_2H_6, C_2H_4, C_2H_2, and C_3H_6. Bonsang et al. (1995) reported emission ratios of CH_4 relative to CO_2 for grassland fires in the Ivory Coast varied between 0.0032 and 0.0046 in the flaming stage, which is similar to our results. The comparison between the emission ratios of this fire experiment and the emission ratios of other fire types and locations are available in the discussion section.

ΔHg/ΔCO values have been used to estimate mercury emissions, it is important to better characterize the ΔHg/ΔCO values under different temporal and spatial conditions to improve the accuracy of emission calculations. For the mobile laboratory measurements calculated emission ratios (Table 4.1b), the largest emission ratio of ΔHg/ΔCO is 2.06E-^{07} (ppbv/ppbv) with a correlation coefficient $R^2 = 0.90$ during the smoldering stage. It demonstrates that THg is primarily emitted during the smoldering stage of the fire.

Biomass burning is an important source of the nitrogen species emitted to the atmosphere; the emissions are dependent on the nitrogen content of the fuel (Burling et al., 2010; Crounse et al., 2009). For NO and NO_y, the largest emission ratio is ΔNO/ΔCO in smoldering stage 0.0051 (ppbv/ppbv) with correlation coefficient $R^2 = 0.97$, $\Delta NO_y/\Delta CO$ in smoldering stage 0.045 (ppbv/ppbv) with correlation coefficient $R^2 = 0.62$.

Table 4.1a. Emission Ratios and Correlation Coefficients for Trace Gases and VOCs versus ΔCO and ΔCO_2

Species	Versus CO_2, ppbv/ppbv						Versus CO, ppbv/ppbv					
	Total		Smoldering		Flaming		Total		Smoldering		Flaming	
	ER	R^2	ER	R^2	ER	R^2	ER	R^2	ER	R^2	ER	R^2
Methane (CH_4)	0.0030	0.89	0.0029	0.91	0.0028	0.94	0.0237	0.81	0.1895	0.82	0.0211	0.91
Carbon Dioxide (CO_2)	****** ****** ******	*** *** ***	****** ****** ******	*** *** ***	****** ****** ******	*** *** ***	8.1482	0.99	69.3497	0.97	7.7594	0.99
Chloromethane (CH_3Cl)	0.2612 3578991	0.98	5.2E-6	0.87	2.5E-5	0.99	0.0002	0.95	0.0003	0.80	0.0002	0.98
Iodomethane (CH_3I)	0.3315 8927917	0.99	1.2E-7	0.87	3.3E-7	0.99	2.7E-6	0.98	8.8E-6	0.91	2.5E-6	0.99
Ethane (C_2H_6)	2.4E-4	0.88	4.7E-5	0.31	2.1E-4	0.94	0.0019	0.79	0.0033	0.30	0.0016	0.90
Ethene (C_2H_4)	0.0017	0.99	6.1E-4	0.96	0.0017	0.99	0.0141	0.99	0.0432	0.95	0.0138	0.99
Ethyne (C_2H_2)	6.4E-4	0.99	1.6E-4	0.96	6.6E-4	0.99	0.0053	0.97	0.0119	0.95	0.0051	0.99
Propane (C_3H_8)	4.3E-5	0.83	9.9E-6	0.12	3.8E-5	0.92	0.0003	0.75	0.0007	0.01	0.0002	0.88
Propene (C_3H_6)	0.0003	0.93	0.0001	0.97	0.0003	0.99	0.0027	0.92	0.0076	0.95	0.0025	0.97
i-Butane (i-C_4H_{10})	3.19E-6	0.91	2.4E-6	0.11	2.8E-6	0.95	2.1E-5	0.80	0.0001	0.01	2.1E-5	0.92
n-Butane (n-C_4H_{10})	0.8999 9815961	0.80	7.4E-6	0.29	7.1E-6	0.90	6.2E-5	0.70	0.0005	0.09	5.2E-5	0.85
i-Pentane (i-C_5H_{12})	0.1555 7323666	0.92	2.3E-6	0.19	1.3E-6	0.95	1.1E-5	0.80	0.0001	0.04	1.0E-5	0.92

n-Pentane (n-C_5H_{12})	3.5E-6	0.69	2.1E-6	0.27	3.1E-6	0.91	2.7E-5	0.72	0.0001	0.04	2.3E-5	0.86
Isoprene (C_5H_8)	1.90E-0612357	0.55	4.0E-6	0.91	1.3E-7	0.02	1.2E-4	0.61	0.0002	0.89	4.8E-6	0.08
n-Hexane (n-C_6H_{14})	0.1896345999132222 1	0.97	8.8E-7	0.31	1.1E-5	0.99	3.5E-4	0.98	6.4E-5	0.01	8.7E-5	0.97
Benzene (C_6H_6)	0.0001	0.98	3.6E-5	0.96	0.0001	0.99	0.0820	0.99	0.0025	0.95	0.0008	0.97
Toluene (C_7H_8)	3.5E-5	0.87	1.2E-5	0.97	3.1E-5	0.91	0.0165	0.88	0.0008	0.97	0.0002	0.87
Cyclopentane (C_5H_{10})	1.0E-8	0.07	3.5E-7	0.59	3.6E-8	0.04	9.8E-8	0.01	2.8E-5	0.67	3.9E-7	0.31
Cyclohexane (C_6H_{12})	1.08E-08	0.02	5.33E-07	0.36	1.87E-07	0.04	4.82E-07	0.02	3.06E-05	0.29	1.68E-06	0.20
Styrene (C_8H_8)	5.99E-07	0.12	1.51E-6	0.95	8.28E-7	0.01	1.39E-06	0.01	0.0001	0.93	1.06E-05	0.21
Ethylbenzene (C_8H_{10})	3.45E-06	0.84	1.83E-06	0.96	2.86E-06	0.79	2.55E-05	0.74	0.0001	0.94	2.03E-05	0.72
t-2-Butene (t-2-C_4H_8)	1.01E-05	0.95	3.45E-06	0.97	9.30E-06	0.94	7.89E-05	0.89	0.0002	0.95	6.97E-05	0.90
1-Butene (1-C_4H_8)	5.51E-05	0.98	1.66E-05	0.96	5.36E-05	0.98	4.39E-04	0.95	0.0011	0.95	0.0004	0.96
i-Butene (i-C_4H_8)	2.78E-05	0.96	8.40E-06	0.93	2.61E-05	0.96	0.0002	0.92	0.0006	0.95	0.0001	0.93
c-2-Butene (c-2- C_4H_8)	8.02E-06	0.96	2.15E-06	0.90	7.47E-06	0.95	6.28E-05	0.91	0.0001	0.86	5.62E-05	0.91
n-Heptane (n-C_7H_{16})	5.32E-07	0.13	1.15E-07	0.09	2.03E-07	0.21	1.11E-07	0.01	8.74E-06	0.09	5.11E-06	0.15

n-Octane (n-C_8H_{18})	2.569564132E-06	0.99	2.61E-07	0.24	2.58E-06	0.99	2.08E-05	0.98	9.86E-06	0.01	1.99E-05	0.98
n-Nonane (n-C_9H_{20})	8.09E-08	0.12	1.11E-08	0.02	8.78E-08	0.11	1.38E-07	0.01	1.68E-06	0.05	1.24E-06	0.21
i-Propylbenzene (i-C_9H_{12})	1.13E-7	0.71	9.89E-08	0.57	8.38E-08	0.60	7.83E-07	0.60	6.22E-06	0.50	5.58E-07	0.52
n-Propylbenzene (n-C_9H_{12})	1.85E-07	0.49	2.26E-07	0.70	9.03E-08	0.28	1.12E-06	0.36	1.37E-05	0.59	4.59E-07	0.18
n-Decane (n-$C_{10}H_{22}$)	5.36E-08	0.11	1.43E-06	0.90	7.87E-08	0.11	1.44E-07	0.01	9.96E-05	0.88	9.98E-07	0.25
o-Xylene	1.31E-06	0.71	5.64E-07	0.65	9.82E-07	0.60	9.16E-06	0.59	4.86E-05	0.78	6.56E-06	0.51
2-Ethyltoluene	2.16E-08	0.09	2.91E-07	0.49	5.43E-08	0.04	1.06E-07	0.01	1.73E-05	0.41	5.84E-07	0.35
3-Ethyltoluene	4.17E-08	0.11	3.09E-07	0.68	7.36E-08	0.04	1.32E-07	0.01	1.98E-05	0.61	8.68E-07	0.31
4-Ethyltoluene	1.13E-07	0.12	2.01E-07	0.29	1.39E-07	0.01	2.10E-07	0.01	9.89E-06	0.20	1.84E-06	0.21
1,3,5-TMB	6.60E-9	0.09	1.12E-10	0.01	2.27E-09	0.04	1.72E-08	0.01	1.89E-07	0.01	8.02E-08	0.14
1,2,4-TMB	3.1E-7	0.10	9.4E-7	0.69	8.0E-7	0.04	1.4E-6	0.01	6.5E-5	0.68	8.5E-6	0.36
1,2,3-TMB	6.2E-8	0.10	4.9E-7	0.56	1.3E-7	0.04	2.4E-7	0.02	3.7E-5	0.60	1.5E-6	0.33
2,2,4-TMP	4.6E-6	0.95	1.9E-6	0.85	4.3E-6	0.95	3.6E-5	0.90	0.0001	0.91	3.2E-5	0.91
m+p-Xylene	5.4E-6	0.87	2.0E-6	0.71	4.5E-6	0.83	4.0E-5	0.78	0.0001	0.78	3.3E-5	0.77

Table 4.1b. Emission Ratios and Correlation Coefficients for Trace Gases versus ΔCO and ΔCO_2 (Mobile Laboratory Measurements)

Species	Versus CO_2, ppbv/ppbv						Versus CO, ppbv/ppbv					
	Total		Smoldering		Flaming		Total		Smoldering		Flaming	
	ER	R^2	ER	R^2	ER	R^2	ER	R^2	ER	R^2	ER	R^2
Methane (CH_4)	0.0072	0.80	0.0039	0.93	0.0061	0.72	1.22E-01	0.96	0.0767	0.87	0.1313	0.95
Carbon Dioxide (CO_2)	1.0	1.0	1.0	1.0	1.0	1.0	16.7712	0.91	18.8494	0.89	14.2981	0.87
Carbon Monoxide (CO)	0.0596	0.91	0.0423	0.89	0.0525	0.87	1.0	1.0	1.0	1.0	1.0	1.0
NitricOxide (NO)	4.26E-04	0.19	0.0002	0.90	4.81E-06	0.01	7.15E-03	0.15	0.0051	0.97	0.0006	0.04
Total Reactive Nitrogen (NO_y)	2.22E-03	0.25	0.0020	0.59	1.97E-05	0.01	3.73E-02	0.22	0.0451	0.62	0.0024	0.05
Total Gaseous Mercury (THg)	1.61E-08	0.14	8.99E-09	0.89	2.06E-08	0.45	2.69E-07	0.17	2.06E-07	0.90	2.25E-07	0.36

4.3.3 Emission Factors and Total Emissions

It is desirable to provide separate emission factors for flaming and smoldering combustion (Andreae et al., 2001). Many field studies have contributed to the database of emission ratios and emission factors, along with the relationship between the combustion stages (Wooster et al., 2011). However, because of uncertainties in emission factors, improvements in understanding of the emission factors are warranted (Freeborn et al., 2009; Kaiser et al., 2009). In our controlled fire experiment, the advantage is, based on the pre-sampling and post-sampling, the fuel characteristics are known at the Texas coastal prairie. Calculated emission factors for each combustion stage are listed in Table 4.2. The comparison between the emission factor of this fire experiment and those of other fires are available in the discussion section.

According to the definition of emission factor, there are 1747g CO_2 emitted from the fire per kg dry fuel combusted. This accounts 90% of all species emission factors, and the CO_2 emission factor during the flaming stage is 200 g/kg more than that from the smoldering stage. CO with a high emission factor of 104 g/kg through the whole fire stage and 3 g/kg more CO emitted during the smoldering stage. Emission factors of CO_2, CO, CH_4, NO, CH_3Cl, C_2H_6, C_2H_4, C_3H_8, C_3H_6, C_6H_6, and C_7H_8 account for 96% of total trace species emission factors. VOC emission factors during the smoldering stage are higher than those during the flaming stage, except for CO_2, n-C_6H_{14} and n-C_8H_{18}. Our estimate for THg (0.0005 g/kg) is identical to that of Biswas et al. (2007) for grassland fires.

Different from previous biomass burning work, our field experiment is unique because the amount of fuel mass for combustion, the mass fraction of carbon in the fuel, the combustion factor, the combustion averaged emission factor, and total burning area are known. This makes it possible to calculate the total emissions of each species accurately during the fire instead of estimating the emissions as most previous work has done. As Table 4.3 demonstrates, 53, 257 kg of CO_2 was emitted into the atmosphere and it accounts 95% of all trace species emissions in the fire. As the second largest emission species, 3,170 kg CO was emitted into the atmosphere. Other significant emissions ordered from highest to least as C_6H_6 (706 kg), C_7H_8 (177 kg), CH_4 (146 kg), NO (108 kg), C_2H_6 (35 kg), C_2H_4 (30 kg), C_2H_2 (14 kg), C_3H_8 (13 kg), and C_3H_6 (11 kg). This controlled fire experiment can play a role as reference data for future biomass burning measurements, especially for grassland or savanna fires, when the fuel information may not be available.

Table 4.2. Emission Factors of Trace Gases and VOCs

Species	UHCC Fire	Emission Factor, g/kg	
	Total	Smoldering	Flaming
Methane (CH_4)	4.8±0.7	5.9±0.9	4.7±0.5
Carbon Dioxide (CO_2)	1747±95	1617±65	1824±50
Carbon Monoxide (CO)	104±15	112±15	109±12
Nitric Oxide (NO)	3.57	3.65	2.44
Total Gaseous Mercury (THg)	0.0005	0.0008	0.0003
Chloromethane (CH_3Cl)	0.07	0.09	0.02
Iodomethane (CH_3I)	0.007	0.008	0.006
Ethane (C_2H_6)	1.17	1.31	0.83
Ethene (C_2H_4)	0.99	1.61	0.80
Ethyne (C_2H_2)	0.463	1.025	0.506
Propane (C_3H_8)	0.443	0.101	0.051
Propene (C_3H_6)	0.380	1.104	0.491
Butane (C_4H_{10})	0.0042	0.038	0.0049
Pentane (C_5H_{12})	0.0065	0.0402	0.0064
Isoprene (C_5H_8)	0.0292	0.0626	0.0013
n-Hexane (n-C_6H_{14})	0.1118	0.0224	0.0291
Benzene (C_6H_6)	23.177	0.936	0.2733
Toluene (C_7H_8)	5.809	0.331	0.072
Cyclopentane (C_5H_{10})	2.55E-04	8.12E-03	1.09E-04
Cyclohexane (C_6H_{12})	1.56E-04	0.0104	0.0006
Styrene (C_8H_8)	0.054	0.042	0.0006
Ethylbenzene (C_8H_{10})	0.0504	0.0106	0.0083
t-2-Butene (t-2-C_4H_8)	0.028	0.041	0.02
1-Butene (1-C_4H_8)	0.0915	0.2688	0.087
i-Butene (i-C_4H_8)	0.0416	0.1344	0.0436
c-2-Butene (c-2- C_4H_8)	0.0131	0.0224	0.0122
n-Heptane (n-C_7H_{16})	3.71E-03	3.61E-03	0.0019
n-Octane (n-C_8H_{18})	8.47E-03	4.56E-03	8.01E-03
n-Nonane (n-C_9H_{20})	6.65E-04	8.70E-04	5.98E-04
i-Propylbenzene (i-C_9H_{12})	3.56E-04	2.88E-03	2.62E-04
n-Propylbenzene (n-C_9H_{12})	4.46E-04	6.72E-03	2.15E-04
n-Decane (n-$C_{10}H_{22}$)	7.91E-03	0.0568	0.0005
o-Xylene	0.0039	0.0157	0.0027
2-Ethyltoluene (2-C_9H_{12})	4.45E-04	8.16E-03	2.80E-04
3-Ethyltoluene (3-C_9H_{12})	5.78E-04	8.87E-03	5.25E-04
4-Ethyltoluene (4-C_9H_{12})	8.03E-04	7.23E-03	6.78E-04
1,3,5-TMB	7.58E-05	9.61E-05	3.74E-05
1,2,4-TMB	6.37E-03	0.0315	4.23E-03
1,2,3-TMB	1.07E-03	0.0163	8.39E-04
2,2,4-TMP	0.0152	0.0456	0.0146
m+p-Xylene	0.0231	0.0373	0.0012

Table 4.3. Total Emissions of Trace Gases and VOCs

Species	Emissions From UHCC Fire (kg)
Methane (CH_4)	146.3272
Carbon Dioxide (CO_2)	53257.0085
Carbon Monoxide (CO)	3170.4229
Nitric Oxide (NO)	108.8309
Total Gaseous Mercury (THg)	0.0152
Chloromethane (CH_3Cl)	2.1339
Iodomethane (CH_3I)	0.2134
Ethane (C_2H_6)	35.6673
Ethene (C_2H_4)	30.1800
Ethyne (C_2H_2)	14.1145
Propane (C_3H_8)	13.5048
Propene (C_3H_6)	11.5842
i-Butane (i-C_4H_{10})	0.1280
Pentane (C_5H_{12})	0.1982
Isoprene (C_5H_8)	0.8902
n-Hexane (n-C_6H_{14})	3.4082
Benzene (C_6H_6)	706.5470
Toluene (C_7H_8)	177.0864
Cyclopentane (C_5H_{10})	0.0078
Cyclohexane (C_6H_{12})	0.0048
Styrene (C_8H_8)	1.6462
Ethylbenzene (C_8H_{10})	1.5364
t-2-Butene (t-2-C_4H_8)	0.8536
1-Butene (1-C_4H_8)	2.7894
i-Butene (i-C_4H_8)	1.2682
c-2-Butene (c-2- C_4H_8)	0.3994
n-Heptane (n-C_7H_{16})	0.1132
n-Octane (n-C_8H_{18})	0.2582
n-Nonane (n-C_9H_{20})	0.0203

i-Propylbenzene (i-C_9H_{12})	0.0109
n-Propylbenzene (n-C_9H_{12})	0.0136
n-Decane (n-$C_{10}H_{22}$)	0.2412
o-Xylene	0.1189
2-Ethyltoluene (2-C_9H_{12})	0.0136
3-Ethyltoluene (3-C_9H_{12})	0.0176
4-Ethyltoluene (4-C_9H_{12})	0.0245
1,3,5-TMB	0.0023
1,2,4-TMB	0.1943
1,2,3-TMB	0.0326
2,2,4-TMP	0.4634
m+p-Xylene	0.7012

4.3.4 Carbon Emissions

Biomass burning plays an important role in the cycling of carbon in many ecosystems and represents a significant source of aerosols and trace gas emissions (Van der werf et al., 2003). The problem of quantifying direct carbon emissions from wildfire has received attention (French et al., 2004), and site-based to global-scale approaches to estimate carbon emissions from fire have been conducted in many regions and sites within North America (French et al., 2011). However, to study the impact of fire on atmospheric carbon, variations in vegetation structure, vegetation type, soil carbon, fuel moisture, and fire behavior need to be considered (French et al., 2004). Most frequently used methods in previous work was remote sensing and model estimates which have uncertainties. To the best of our knowledge, this is the first estimate of total carbon released during a wildfire in Texas based on in-situ measurements. Calculating total carbon emissions from biomass burning (Ct) is generally done by estimating the area

affected by fire along with the amount of fuel consumed during the fire, the fuel moisture and carbon content. 194 tons ($1.94*E^{05}$ kg) of carbon emitted from the fuel in combustion, among them, 14.5 tons ($1.45*E^{04}$ kg) of carbon released by CO_2 emissions (Figure 4.5), it accounts 7.5% of the total carbon emissions (14.5 tons / 194 tons). Considering CO_2 is the major trace species emission, we suspect that the largest mass of carbon is released via particles as black and organic carbon into the atmosphere.

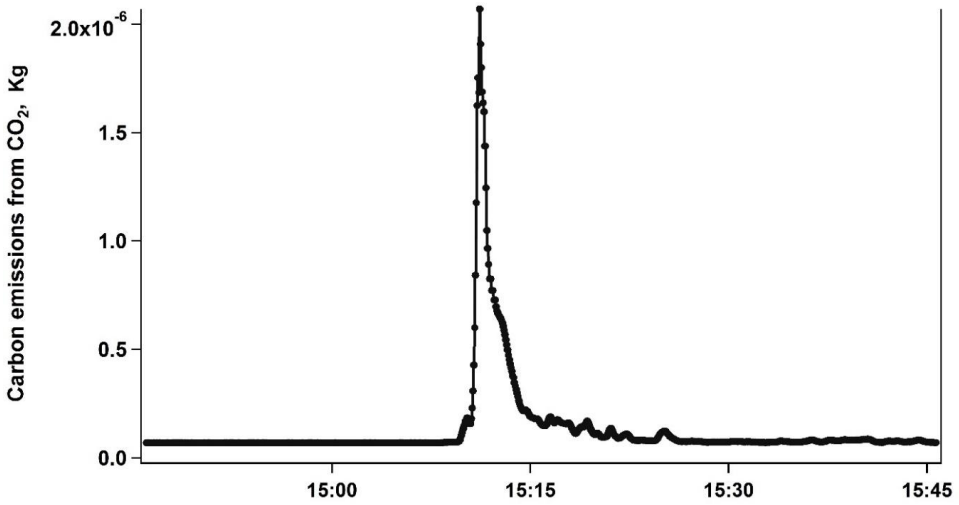

Figure 4.5. Time series of carbon emissions (C) via CO_2.

4.4 Discussion

Emission ratios of species relative to CO from Texas field-based grassland fire are in contrast with emission ratios of airborne-based biomass burnings in Australia, Brazil, Africa, and Yucatan (Mexico) as demonstrated in Table 4.4. The CH_4 emission ratio was largest in Brazil forest biomass burning (0.1240, probably due to the longer smoldering stage of the fire), and smallest in the Australia fire (0.0044). The CO_2 emission ratio shows significant diversity among the six experiments: the emission ratio in Yucatan fires

was 13 ppbv/ppbv, followed by this Texas fire with 8 ppbv/ppbv, and the Brazil 1998 fire at 6.3 ppbv/ppbv. The other three fires had small emission ratios lower than 0.0001 ppbv/ppbv. Except CH_4 and CO_2, the other species emission ratios are close to each other with small differences among the six fire experiments, which probably is because these species emissions only account small emissions during the fire regardless of the fire type and combustion efficiency.

Table 4.4. Emission Ratios and Correlation Coefficients for Trace Gases and Volatile Organic Compounds Relative to CO of Different Fire Experiments

Species	UHCC ppbv/ppbvground	R^2	Australia ppbv/ppbv Airborne	R^2	Brazil1994p pbv/ppbvAirborne	R^2	Brazil1998 ppbv/ppbvAirborne	R^2	Africa ppbv/ppbv Airborne	R^2	Yucatan ppbv/ppbv Airborne
Methane (CH_4)	0.0237	0.81	0.0044	0.78	0.1070	0.86	0.1240	0.90	0.0078	0.91	0.1104
Carbon Dioxide (CO_2)	8.1483	0.99	8.6E-05	0.97	3.7E-05	0.87	6.3217	0.43	6.2E-05	0.96	13.0241
Chloromethane (CH_3Cl)	0.0002	0.95	0.00038	0.89	0.00031	0.90	0.000116	0.05	0.00057	0.92	-
Iodomethane (CH_3I)	2.7E-06	0.98	2.8E-06	0.82	3.6E-06	0.60	1.4E-05	0.31	1.2E-06	0.70	-
Ethane (C_2H_6)	0.0019	0.79	0.0028	0.97	0.0085	0.84	0.0052	0.85	0.0052	0.96	0.0098
Ethene (C_2H_4)	0.0141	0.99	0.0071	0.93	0.0171	0.95	0.0105	0.83	0.0083	0.78	0.0111
Ethyne (C_2H_2)	0.0053	0.97	0.0029	0.96	0.0046	0.90	0.0024	0.63	0.0045	0.98	0.0029
Propane (C_3H_8)	0.0003	0.75	0.00058	0.97	0.0016	0.79	0.0010	0.82	0.00097	0.94	0.0015
Propene (C_3H_6)	0.0027	0.92	0.0016	0.86	0.0049	0.98	0.0039	0.87	0.001	0.56	0.0079
i-Butane (i-C_4H_{10})	2.1E-05	0.80	4.8E-05	0.96	6.7E-05	0.78	7.4E-05	0.82	4.3E-05	0.77	8.6E-05
n-Butane (n-C_4H_{10})	6.2E-05	0.70	0.0001	0.97	0.0002	0.70	0.0002	0.79	0.0002	0.88	0.0003
i-Pentane (i-C_5H_{12})	1.1E-05	0.80	6.5E-06	0.69	2.0E-05	0.57	3.1E-05	0.73	-	-	3.4E-05
n-Pentane (n-C_5H_{12})	2.7E-05	0.72	2.8E-05	0.97	4.3E-05	0.84	5.8E-05	0.81	5.3E-05	0.80	6.9E-05
Isoprene (C_5H_8)	1.2E-04	0.61	-	-	-	-	6.9E-05	0.73	-	-	-
n-Hexane (n-C_6H_{14})	3.5E-04	0.98	4.2E-05	0.89	-	-	-	-	-	-	-
Benzene (C_6H_6)	0.0820	0.99	0.0008	0.97	0.0017	0.97	0.0014	0.89	0.0013	0.96	0.0034
Toluene (C_7H_8)	0.0165	0.88	0.0003	0.93	0.0007	0.72	0.0009	0.81	0.0004	0.85	-
Cyclopentane (C_5H_{10})	9.8E-08	0.01	-	-	-	-	-	-	-	-	5.8E-06
Ethylbenzene (C_8H_{10})	2.5E-05	0.74	3.4E-05	0.85	4.2E-05	0.83	9.6E-05	0.70	2.6E-05	0.52	-
t-2-Butene (t-2-C_4H_8)	7.8E-05	0.89	2.6E-05	0.52	0.0002	0.88	0.0002	0.89	-	-	2.5E-04
1-Butene (1-C_4H_8)	4.3E-4	0.95	0.0002	0.84	0.0007	0.75	0.0006	0.90	0.0001	0.54	6.0E-04
i-Butene (i-C_4H_8)	0.0002	0.92	-	-	-	-	-	-	-	-	5.1E-04
c-2-Butene (c-2-C_4H_8)	6.3E-05	0.91	2.2E-05	0.60	0.0002	0.87	0.0002	0.89	-	-	1.9E-04
n-Heptane (n-C_7H_{16})	1.1E-07	0.01	1.7E-05	0.83	-	-	-	-	-	-	-
m+p-Xylene	4.1E-05	0.78	5.8E-05	0.81	6.9E-05	0.83	0.0001	0.72	4.0E-05	0.53	
Nitric Oxide (NO)	7.1E-03	0.15	-	-	-	-	-	-	-	-	0.0202
Total Reactive Nitrogen (NO_y)	3.7E-02	0.22	-	-	-	-	-	-	-	-	0.0453

The comparison of emission factors is presented in Table 4.5. Trace gases and VOCs measured from our field-based Texas grassland fire experiment is in contrast with measurements from various types of biomass burnings. CH_4 emission factor in Texas grassland fire is 0.2 g/kg lower than Yucatan forest fire, but two times higher than the global average savanna and grassland fire emission factors (Akagi et al., 2011; Andreae et al., 2001). Without exception, CO_2 emission factors are the largest and account for 90% of the total emission factors in all fire events despite of fire type and locations. The CO emission factor together with most other trace species emission factors in the Texas fire experiment are larger than those emission factors from other biomass burnings, especially the C_6H_6 emission factor for the Texas fire being 100 times higher than for other fires. The reason for this is unclear, but it is not related to calibration.

Table 4.5. Emission Factors for Trace Gases and Volatile Organic Compounds in Different Fire Experiments

Species	UH EF g/kg	Savanna EF g/kg (Akagi)	Grassland EF g/kg (Andreae)	Yucatan Fire EF g/kg (Yokelson)
Methane (CH_4)	4.8±0.7	1.94±0.85	2.3±0.9	5.059
Carbon Dioxide (CO_2)	1747±95	1686±38	1613±95	1641
Carbon Monoxide (CO)	104±15	63±17	65±20	80
Nitric Oxide (NO)	4.57	3.90	3.90	1.733
Total Gaseous Mercury (THg)	0.0005	-	0.001	-
Chloromethane (CH_3Cl)	0.07	0.055	0.075	-
Iodomethane (CH_3I)	0.007	5.06E-04	0.0005	-
Ethane (C_2H_6)	1.17	0.66	0.32	0.844
Ethene (C_2H_4)	0.99	0.82	0.79	0.889
Ethyne (C_2H_2)	0.463	0.24	0.29	0.215
Propane (C_3H_8)	0.443	0.10	0.09	0.192
Propene (C_3H_6)	0.380	0.79	0.26	0.952
Butane (C_4H_{10})	0.0042	0.0043	0.006	0.042
Pentane (C_5H_{12})	0.0065	0.0022	0.005	0.014
Isoprene (C_5H_8)	0.0292	0.039	0.020	-
n-Hexane (n-C_6H_{14})	0.1118	0.013	0.039	-
Benzene (C_6H_6)	23.177	0.20	0.23	0.759
Toluene (C_7H_8)	5.809	0.080	0.13	-
Cyclopentane (C_5H_{10})	2.52E-04	0.0019	0.032	0.0012

Cyclohexane (C_6H_{12})	1.56E-04	0.0035	-	-
Styrene (C_8H_8)	0.054	-	0.024	-
Ethylbenzene (C_8H_{10})	0.0504	0.006	0.013	-
t-2-Butene (t-2-C_4H_8)	0.028	0.011	0.024	0.04
1-Butene (1-C_4H_8)	0.0915	0.043	0.09	0.096
i-Butene (i-C_4H_8)	0.0416	0.024	0.030	0.081
c-2-Butene (c-2- C_4H_8)	0.0131	0.0084	0.021	0.03
n-Heptane (n-C_7H_{16})	3.71E-03	0.0070	0.05	-
n-Octane (n-C_8H_{18})	8.47E-03	-	-	-
n-Nonane (n-C_9H_{20})	6.65E-04	-	-	-
i-Propylbenzene (i-C_9H_{12})	3.57E-04	-	-	-
n-Propylbenzene (n-C_9H_{12})	4.46E-04	0.018	-	-
n-Decane (n-$C_{10}H_{22}$)	7.91E-03	-	-	-
o-Xylene	0.0039	0.014	0.045	-

4.5 Conclusions

In the past decades significant progress has been made in characterizing trace species emissions from biomass burning via ground and airborne methods. Selected atmospheric trace gases and VOCs emitted by a Texas coastal grassland fire were measured together with comprehensive pre-combustion and post-combustion sampling. Emission ratios, emission factors, and total emissions were determined for a large variety of species under smoldering and flaming stages. All trace species measured by the mobile laboratory show single-peak characteristics and their peak time matches well with the fire plume time, while the VOCs exhibited double peaks features with primary emissions associated with smoldering combustion stage. The emission factors of CO_2, CO, CH_4, NO, CH_3Cl, C_2H_6, C_2H_4, C_3H_8, C_3H_6, C_6H_6, and C_7H_8 account for 96% of total trace species emission factors. Meanwhile, most of the VOC emission factors during the smoldering stage are higher than those during the flaming. For the emissions from this fire, 53,257 kg of CO_2 was emitted into the atmosphere and it accounted 95% of all species emissions, on the other hand, total of 194 tons of carbon emitted from the fuel, among them, 14.5 tons of carbon released via CO_2 emissions.We suspect that the largest

mass of carbon is released via the particulate phase into the atmosphere. The CO emission factor together with most other species emission factors in this Texas fire were larger than those from other biomass burnings, in-situ field measurement with less uncertainties compared with remote measuring methods is a possible reason. This controlled fire experiment in a coastal prairie area can serve as a reference for the future field or airborne biomass burning measurements, especially for grassland or savanna fires, when their fuel information may not be available.

4.6 Acknowledgements

The author would like to thank members of the Department of Earth and Atmospheric Sciences in University of Houston for the trace species data measurements, and we appreciate Barkley C. Sive's group at Appalachian State University for their work on the VOCs.

4.7 References

Akagi S.K., Yokelson R.J., Wiedinmyer C., Alvarado M.J., Reid J.S., Karl T., Crounse J.D., and Wennberg P.O., Emission factors for open and domestic biomass burning for use in atmospheric models, *Atmos. Chem. Phys*., 11, 4039-4072, 2011.

Alvarado M.J., and Prinn R.G., Formation of ozone and growth of aerosols in young smoke plumes from biomass burning: 1. Lagrangian parcel studies, *J. of Geophys. Res.* 10, 1029-1038, 2009.

Andreae M.O. and Merlet P., Emission of trace gases and aerosols from biomass burning, *Glob. Biogeo. Cycl.* 955-966, 2001.

Andreae M.O., and Crutzen P.J., Atmospheric Aerosols: Biogeochemical Sources and Role in Atmospheric Chemistry, *Sci*. 276, 5315, 1052, 1997.

Andreae M.O., Methyl halide emission from savanna fires in southern Africa, *J. Geophys. Res.* 101, 23, 603-23, 1996.

Andreae M.O., Browell E.V., Garstang M., Gregory G.L., Harriss R.C., Hill G.F., Jacob D.J., Pereira M.C., Sachse G.W., Setzer A.W., Silva Dias P.L., Talbot R.W., Torres A.L., and Wofsy S.C., Biomass-burning emissions and associated haze layers over Amazonia, , *J. Geophys. Res.* 10, 1029, 1509, 1988.

Biswas, A; Blum, J. D.; Klaue, B.; Keeler, G. J. Release of mercury from Rocky Mountain forest fires. *Biogeo. Cyc. 21*, 1002, 2007.

Blake N.J., Blake D.R., Sive B.C., Chen T.Y., and Rowland F.S., Biomass burning emissions and vertical distribution of atmospheric methyl halides and other reduced carbon gases in the South Atlantic region, *J. Geophys. Res*. 24, 151-24, 1996.

Bonsang B., Boissard C., Le Cloarec M. F., RudolphAffiliated J, and Lacaux J. P., Methane, carbon monoxide and light non-methane hydrocarbon emissions from African savanna burnings during the FOS/DECAFE experiment, *J. Atmos. Chem.* 11, 149-162, 1995.

Bowman D.M., Balch J.K., Artaxo P., Bond W.J., Carlson J.M., Cochrane M.A., D'Antonio C.M., Defries R.S., Doyle J.C., Harrison S.P., Johnston F.H., Keeley J.E., Krawchuk M.A., Kull C.A., Marston J.B., Moritz M.A., Prentice I.C., Roos C.I., Scott A.C., Swetnam T.W., Van der Werf G.R., and Pyne S.J., Fire in the Earth system, *Sci.* 324, 481-484, 2009.

Burling I.R., Yokelson R.J., Griffith D.W.T., Johnson T.J., Veres P., Roberts J.M., Warneke C., Urbanski S.P., Reardon J., Weise D.R., Hao W.M., and Gouw J., Laboratory measurements of trace gas emissions from biomass burning of fuel types from the

southeastern and southwestern United States, *Atmos. Chem. Phys.*, 10, 11115-11130, 2010.

Christian T., Kleiss B., Yokelson R.J., Holzinger R., Crutzen P.J., Hao W.M., Saharjo B.H., and Ward D.E., Comprehensive laboratory measurements of biomass burning emissions: 1. Emissions from Indonesian, Africa, and other fuels, *J. Geophys. Res.* 108(D23), 4719, 2003.

Clements C.B., Observing the dynamics of wildland grass fires: FireFlux – a field validation experiment. *Bull. Amer. Meteorol. Soc.* 88, 1369-1382, 2007.

Crounse J. D., DeCarlo P. F., Blake D. R., Emmons L. K., Campos T. L., Apel E. C., Clarke A. D., Weinheimer A. J., McCabe D. C., Yokelson R. J., Jimenez J. L., and Wennberg P. O., Biomass burning and urban air pollution over the Central Mexican Plateau, *Atmos. Chem. Phys.* 10, 5194-5210, 2009.

Crutzen P.J., and Andreae M.O., Biomass Burning in the Tropics: Impact on Atmospheric Chemistry and Biogeochemical Cycles, *Science*, 250.49881669, 1990.
Ferek R.J., Jeffrey S.R., and Hobbs P.V., Emission factors of hydrocarbons, halocarbons, trace gases and particles from biomass burning in Brazil, *J. Geophys. Res.* 32, 107-32, 1998.

Freeborn P.H., Wooster M.J., Hao W.M., Ryan C.A., Nordgren B.L., Baker S.P., and Ichoku C., Relationships between energy release, fuel mass loss, and trace gas and aerosol emissions during laboratory biomass fires, *J. Geophys. Res.* 113, D01102, 2008.

Freeborn P.H., Wooster M.J., Roberts G., Malamud B., and Xu W., Development of a virtual active fire product for Africa through a synthesis of geostationary and polar orbiting satellite data, *Remote Sens. Environ.* 113, 1700-1711, 2009.

French N.H.F, Goovaerts P., Kasischke E.S., Uncertainty in estimating carbon emissions from boreal forest fires, *J. Geophys. Res*. 1029, 3635, 2004.

French N.H.F., de Groot W.J., Jenkins L.K., Rogers B.M., Alvarado E., Amiro B., Jong B., Goetz S., Hoy E., Hyer E., Keane R., Law B. E., McKenzie D., McNulty S,G., Ottmar R., Pérez-Salicrup D.R., Randerson J., Robertson K.M., and Turetsky M., Model comparisons for estimating carbon emissions from North American wildland fire, *J. Geophys. Res.* 1469, 2011.

Goode J.G., and Yokelson R.J., Trace gas emissions from laboratory biomass fires measured by open-path Fourier transform infrared spectroscopy: Fires in grass and surface fuels, *J. Geophys. Res*, 21, 237-21, 245, 1999.

Goode J.G., Yokelson R.J., Ward D.E., Susott R.A., Babbitt R.E., Davies M.A., and Hao W.M., Measurements of excess O_3, CO_2, CO, CH_4, C_2H_4, C_2H_2, HCN, NO, NH_3,

HCOOH, CH_3COOH, HCHO, and CH_3OH in 1997 Alaskan biomass burning plumes by airborne Fourier transform infrared spectroscopy (AFTIR), *J. Geophys. Res*. 105(D17), 22147-22166, 2000.

Hao W.M., and Liu M.H., Spatial and temporal distribution of tropical biomass burning, *Glob. Biogeo. Cyc.* 8, 495-503, 1994.

Hobbs P.V., Sinha P., Yokelson R.J., Christian T.J., Blake D.R., Gao S., Kirchstetter T.W., Novakov T., and Pilewskie P., Evolution of gases and particles from a savanna fire in South Africa, *J. Geophys. Res.* 108(D13), 8485, 2003.

Hurst D.F. and Griffith W.T., Trace gas emissions from biomass burning in tropical Australian savannas, *J. Geophys. Res.* 16,441-16,456, 1994.

Kaiser J., Boucher O., Doutriaux-Boucher M, Flemming J., Govaerts Y.M., Gulliver J., Heil A., Jones L., Lattanzio A., Morcrette J., Perrone M.R., Razinger M., Roberts G., Schultz M.G., Simmons A.J., Suttie M., and Wooster M.J., Smoke in the Air, *ECMWF News*. No. 119, 2009.

Keywood M., Kanakidou M., Stohl A., Dentener F., Grassi G., Meyer C. P., Torseth K., Edwards D., Thompson A.M., Lohmann U., and Burrows J., Fire in the Air: Biomass Burning Impacts in a Changing Climate, *Environ. Sci. and Tech*. 604248, 2013.

Koppmann R., Czapiewski K., and Reid J.S., A review of biomass burning emissions, part I: gaseous emissions of carbon monoxide, methane, volatile organic compounds, and nitrogen containing compounds, *Atmos. Chem. Phys. Discuss.* 5, 10455-10516, 2015.

Koppmann R., Khedim A., Rudolph J., Poppe D., Helas G., Welling M., and Zenker T., Emissions of organic trace gases from savanna fires in Southern Africa during SAFARI 92 and their impact on the formation of tropospheric ozone, *J. Geophys. Res.* 845, 1997.

Lan X., Talbot R.W., Laine P., Lefer B., Flynn J., Sun Z., and Torres A., Seasonal and diurnal variations of total gaseous mercury in urban Houston, Texas (U.S.A.), *Atmos. 5*, 399-419, 2014.

Liu L., Talbot R.W., and Lan X., Influence of Climate Change and Meteorological Factors on Houston's Air Pollution: Ozone a Case Study, *Atmos*. 6, 623-640, 2015.

Luke W.T., Kelley P., Lefer B., Flynn J., Rappengluck B., Leuchner M., Dibb J.E., Ziemba L.D., Anderson C.H., and Buhr M., Measurements of primary trace gases and NOY composition in Houston, Texas, *Atmos. Environ*. 4068–4080, 2010.

Schultz M.G., Jacob D.J., Wang Y., Logan J.A., Atlas E.L., Blake D.R., Blake N.J., Bradshaw J.D., Browell E.V., Fenn M.A., Flocke F., Gregory G.L., Heikes B.G., Sachse G.W., Sandholm Shetter, S. T., R.E., Singh H.B., Talbot R.W., On the origin of

tropospheric ozone and NOx over the tropical South Pacific, *J. Geophys. Res.* 2309, 1999.

Shirai T., Blake D.R., Meinardi S., Rowland F.S., Smith J.R., Edwards A., Kondo Y., Koike M., Kita K., Machida T., Takegawa N., Nishi N., Kawakami S., and Ogawa T., Emission estimates of selected volatile organic compounds from tropical savanna burning in northern Australia, *J. Geophys. Res.* JD000841, 2003.

Singh H.B., Kanakidou M., Crutzen P.J., and Jacob D.J., High concentrations and photochemical fate of oxygenated hydrocarbons in the global troposphere, *Natu*. 378(6552), 50-54, 1995.

Sive B. C., Zhou Y., Troop D., Wang Y., Little W.C., Wingenter O.W., Russo R.S., Varner R.K., and Talbot R., Development of a cryogen-free concentration system for measurements of volatile organic compounds, *Anal. Chem., 77*(21), 6989-6998, 2005.

Sudo K., and Akimoto H., Global source attribution of tropospheric ozone: Long-range transport from various source regions, *J. Geophys. Res.* 7992, 2007.

Van der werf G.R., Randerson J.T., Collatz G.J., and Giglio L., Carbon emissions from fires in tropical and subtropical ecosystems, *Glob. Chan. Bio.* 604, 2003.

Ward D.E., and Hardy C.C., Smoke emissions from wildland fires, *Environ. Int.*, 17,117-134, 1991.

Wiedinmyer C., and Friedli H., Mercury emission estimates from fires: an initial inventory for the United States, *Environ. Sci. Technol*, 41, 8092-8098, 2007.

Wooster M.J., Freeborn P.H., Archibald S., Oppenheimer C., Roberts G.J., Smith T.E.L., Govender N., Burton M., and Palumbo I., Field determination of biomass burning emission ratios and factors via open-path FTIR spectroscopy and fire radiative power assessment: headfire, backfire and residual smouldering combustion in African savannas, *Atmos. Chem. Phys.*, 11, 11591-11615, 2011.

Yokelson R.J., Crounse J.D., DeCarlo P.F., Karl T., Urbanski S., Atlas E., Campos T., Shinozuka Y., Kapustin V., Clarke A.D., Weinheimer A., Knapp D.J., Montzka D.D., Holloway J., Weibring P., Flocke F., Zheng W., Toohey D., Wennberg P.O., Wiedinmyer C., Mauldin L., Fried A., Richter D., Walega J., Jimenez J.L., Adachi K., Buseck P.R., Hall S.R., and Shetter R., Emissions from biomass burning in the Yucatan, *Atmos. Chem. Phys.*, 9, 5785-5812, 2009.

Yokelson R.J., Goode J.G., Ward D.E., Susott R.A., Babbitt R.E., Wade D.D., Bertschi I., Griffith D.W.T., and Hao W.M., Emissions of formaldehyde, acetic acid, methanol, and other trace gases from biomass fires in North Carolina measured by airborne Fourier transform infrared spectroscopy, *J. Geophys. Res*. 900817, 1999.

Chapter 5

Concluding Remarks

We found that background O_3 mixing ratios in Houston are flat or decreasing slightly around 30 ppbv. The exceedance days of 1-h/8-h averaged O3 mixing ratio decreased dramatically from tens of days to only a couple of days annually. A rapid shift occurred around 2000. Southerly flow has been increasing in the Houston area since at least 1990. Both the frequency and the wind speed of the southerly flow have increased. During 2010~2013, 60% of the wind direction was concentrated in the range of 130°–195°, which is southerly winds or southeasterly winds, from the Gulf of Mexico. The cause for increased southerly flow is an increase of nearly 3 °C in LST compared to the SST of the ocean. The net temperature difference between LST and SST increased by a factor of four in May and by a factor of two in June. Before 1999, the range between the maximum and minimum was 12 °C, however, between 1999 and 2012, the range increased to 20 °C, with a pronounced increase in variability.

Our continuous measurements and comprehensive analysis of GEM, RGM, and PBM were conducted under urban and coastal settings in Houston, Texas. This study provides an investigation of mercury characteristics in a city where industrial facilities are highly concentrated. The urban setting's GEM mean mixing ratios were higher than the Northern Hemisphere background level. RGM and PBM mean mixing ratios were 6 times higher than the RGM and PBM background level (0.112 ppqv). Under the coastal setting, the mean mixing ratio of GEM was 165 ppqv, equal to the Northern Hemisphere

background level however higher than the GEM measured in other coastal sites in the Northeast United States. The mean value of RGM measured at CC site was 0.75 ppqv, for PBM 0.58 ppqv. Both RGM and PBM mean mixing ratios were 4 times higher than the RGM and PBM Northern Hemisphere background level however lower than at MT. It is probably due to the coastal settings reduction of contaminations by diluting with cleaner air from the Gulf of Mexico. Consequently, the CC site had a higher frequency of low mercury events than the MT site. The seasonal distribution of mercury was small in the Houston area. Seasonal GEM mixing ratios showed tiny differences at MT site but distinct variations at CC, which are probably because of the north and southeast air flows at this site. Mercury mixing ratios exhibited pronounced diurnal variations. At urban site, GEM increased at midnight and accumulated overnight until reaching the maximum right before sunrise. Then it followed a gradual decrease in the following hours. The coastal site diurnal pattern was different, as GEM exhibited a steady decrease at night and reached its minimum mixing ratio before the sunrise, it slowly increased after the sunrise and reached the maximum mixing ratio in the late morning. At the urban site, GEM of 100-250 ppqv was associated with winds from the south and southeast, where air mainly originated from the Gulf of Mexico with cleaner background levels. GEM levels above 250 ppqv were in consistent with winds originated mainly from the north or northeast, where air mases accumulated urban and industrial emissions. The relationships between mercury species and key trace gases were conducted, the co-occurrence of GEM, CO_2, CO, CH_4, SO_2 maximum values at MT and GEM, CO peak at CC were striking. It unveils that GEM, CO, CO_2, CH_4, and SO_2 probably shared the same or related emission sources.

Selected atmospheric trace gases and VOCs emitted by a Texas coastal grassland fire were measured together with comprehensive pre-combustion and post-combustion sampling. Emission ratios, emission factors, and total emissions were determined for a large variety of species under smoldering and flaming stages. All trace species measured by the mobile laboratory show single-peak characteristics and their peak time matches well with the fire plume time, while the VOCs exhibited double peaks features with primary emissions associated with smoldering combustion stage. The emission factors of CO_2, CO, CH_4, NO, CH_3Cl, C_2H_6, C_2H_4, C_3H_8, C_3H_6, C_6H_6, and C_7H_8 account for 96% of total trace species emissions. Meanwhile, most of the VOC emission factors during the smoldering stage are higher than those during the flaming. For the emissions from this fire, 53,257 kg of CO_2 was emitted into the atmosphere and it accounted 95% of all species emissions, on the other hand, total of 194 tons of carbon emitted from the fuel, among them, 14.5 tons of carbon released via CO_2 emissions., We suspect that the largest mass of carbon is released via the particulate phase into the atmosphere. The CO emission factor together with most other species emission factors in this Texas fire were larger than those from other biomass burnings, in-situ field measurement with less uncertainties compared with remote measuring methods is a possible reason. This controlled fire experiment in a coastal prairie area can serve as a reference for the future field or airborne biomass burning measurements, especially for grassland or savanna fires, when their fuel information may not be available.

The future work is strongly warranted to quantify the ozone and mercury emission sources combining modeling and observational work. I strongly suggest conducting ground measurements to quantify emission sources with our mobile laboratory. For a

better understanding of these source signatures, future studies should include the measurements of $\delta^{13}C$ in CH_4, NO, NO_2, and SO_2 as well as the sampling of oil and gas emissions under urban and coastal settings in south-central Texas.